NON-RECIPROCAL ACOUSTIC DEVICES FOR RF COMMUNICATIONS

José Antonio Bahamonde

Submitted in partial fulfillment of the
requirements for the degree of
Doctor of Philosophy
under the Executive Committee
of the Graduate School of Arts and Sciences

COLUMBIA UNIVERSITY

2020

Abstract

The purpose of this research is to develop, demonstrate, and characterize a novel architecture based on surface acoustic wave (SAW) devices capable of non-reciprocal propagation of forward and reverse signals. To begin, a novel topology is introduced based on asymmetrical delay lines and a current source representing a copy of the input signal. An analysis of this structure demonstrates it is capable of functioning as an isolator with the added capability of tuning the frequency response by controlling the phase relationships between input signal and its copy. The structure is dependent on creating large phase shifts of 360° and 180° which is implemented in the acoustic domain. The current source functioning as a copy of the input signal is implemented by a parametric circuit. When a non-linear capacitor is pumped by a large signal at exactly twice the input signal frequency, an amplified copy of the input signal is reflected with a phase shift according to the pump signal phase due to the presence of negative resistance. This is precisely the behavior required for the topology to function. This type of parametric amplification is known as phase-coherent degenerate parametric amplifier.

To investigate further, models are developed for the surface acoustic wave transducers, the non-linear capacitor, and the overall structure in Keysight's Advanced Design Systems (ADS). Harmonic balance simulations in ADS verify the theory and demonstrate the same tunable behavior. These simulations are then used to design the SAW device and the peripheral circuitry required to match and isolate the pump signal from the input signal.

The SAW device is fabricated on bulk $LiNbO_3$ and bonded to a PCB board containing the pump circuitry. The first implementation is based on a bi-directional center transducer design and demonstrates overall functionality with limited bandwidth due to the single resonant parametric circuit design. A secondary device with a uni-directional SAW center transducer, which better matches the bandwidth of the input and output transducers, and a 2nd order resonant network result in improved performance demonstrating gain and isolation throughout the bandwidth of the SAW filter. Furthermore, the tunable aspect is also demonstrated by controlling the phase relationship

between input and pump signals. This device, however, requires phase-coherence between signals and the relationship $f_P = 2f_S$ to be maintained. This is difficult to implement in practical systems and requires additional complicated circuitry. For this reason, a phase-incoherent version was also investigated.

The addition of the uni-directional center transducer which couples the negative resistance to the acoustic waves, generates another form of asymmetry which also results in non-reciprocal propagation of forward and reverse signals. Due to its general applicability, the focus of the work is shifted to this prototype. The device is capable of functioning under different pump frequencies each with its advantages and disadvantages. For this reason, the performance both phase-coherent and incoherent modes of operation in terms of gain, isolation, noise, and linearity are characterized and understood under the lens of parametric amplification. When compared to the state-of-the-art, the device exhibits superior performance in terms of isolation and insertion loss.

Table of Contents

List of Tables

List of Figures

ACKNOWLEDGEMENTS

First and foremost, I would like to thank my advisor, Prof. Ioannis Kymissis, whose support, guidance, and insight, have been indispensable over the years. I would also like to thank Prof. Harish Krishnaswamy whose advising, feedback, and collaboration inspired much of my research.

I would like to thank Prof. Peter Kinget, Prof. Wen Wang, Prof. James Hone, and Prof. Mingoo Seok for taking time out of their busy schedules to be a part of the committee to review my dissertation and listen to my presentation. I'm very grateful for their investment and support.

I would also like to extend my gratitude to the electrical engineering department staff of Columbia University for helping me make all of the transitions over the years from master's student to PhD candidate.

I would also like to thank the Columbia Nano Initiative staff for their assistance and support in the clean room. I greatly appreciate their help in developing processes to fabricate the various devices I have researched over the year.

I would like to thank members of the Columbia Laboratory for Unconventional Electronics (CLUE) and Columbia high-speed and Mm-wave IC (CoSMIC) research groups for their conversation and support.

This work was supported by the Nation Science Foundation (NSF) Emerging Frontiers in Innovation and Research (EFRI) program 1641100.

Dedication

This dissertation is dedicated to my parents José Antonio Bahamonde Sr. and Haydeé Bahamonde whose unyielding love, support, and encouragement kept me inspired to pursue this research.

CHAPTER 1
INTRODUCTION AND BACKGROUND

As the demand for higher performance in wireless communications increases, the community has responded with new protocols and hardware innovations to meet customer expectations. In the advent of fifth generation (5G) technology, there still exists a discussion on what is the path forward. If history is any indicator, the next generation will not deviate too far from a current successful one. The FCC has defined three possibilities for 5G systems: 3.5GHz-6 GHz, 27-40 GHz, and 64-71 GHz. These three bands contain their own unique challenges in implementation, yet they all share a common challenge in that of filtering. This issue in particular can very well determine the future of front-end circuits for radio frequency (RF) communications.

Historically, RF filtering has been peen predominantly performed by acoustic devices due to their low insertion loss and form factor compared to its electromagnetic counter-parts. Because of its incredibly small size, they have been almost exclusively used in this role in cell phones since very early on with the number of acoustic devices per phone only increasing in current designs. Furthermore, with no disruptive technology on the horizon that can meet the cost requirements, performance, and size of the current acoustic technologies for mobile devices, these devices will continue to dominate in applications with operating frequency lower than 10GHz [1]. For instance, in fourth generation (4G) long term evolution (LTE) technology, up to 30 acoustic filters are used in cell phones to accommodate carrier aggregation (CA) in both transmit (TX) and receive (RX) bands where the transmitted/received codes are spread into different frequencies requiring their own filter [2]. Figures 1.1 a) and b) are example of what a CA front-end circuits look like for 4G LTE systems. For the system to function properly, the filters are designed at different center frequencies with 10's of MHz of bandwidth. They are also required to be benign or completely isolated from each other so that pass-bands do not overlap. If this is the case, the topology in figure 1.1 a) can be used. However, as one might expect, as the number of filters increases to

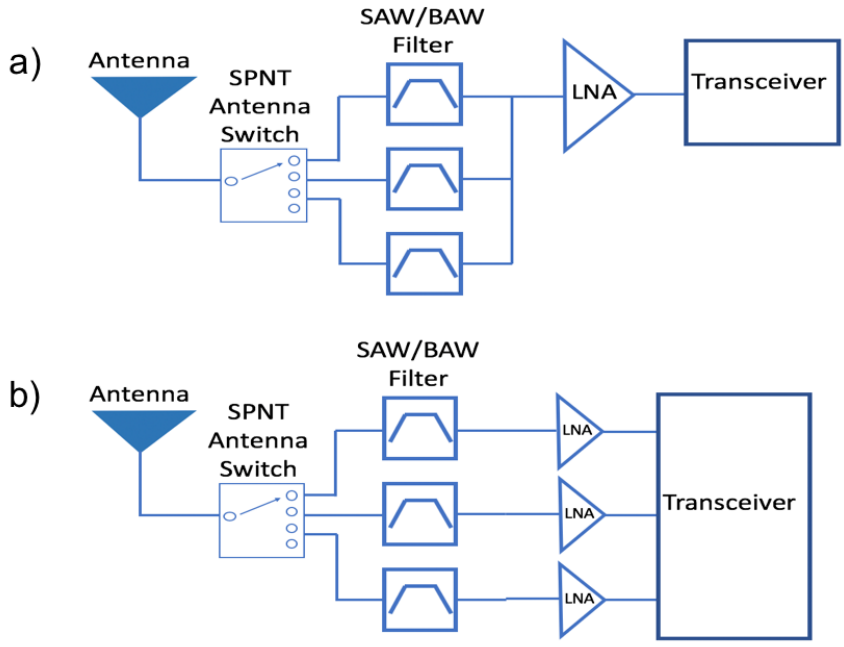

Figure 1.1: a) Direct conversion topology for 4G LTE front end circuit where band-pass filters share transceiver connection. b) 4G LTE front end topology where filters are isolated electrically. An antenna switched is used to select between desired bands from. a bank of acoustic filters whose output is then amplified and delivered to the transceiver circuit [1].

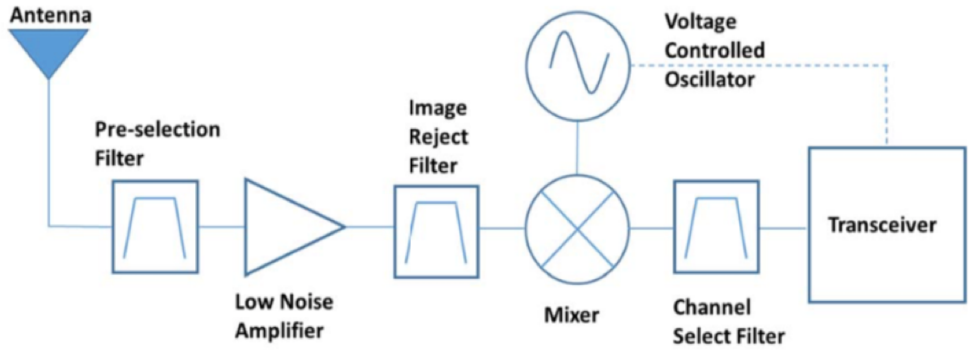

Figure 1.2: Super-heterodyne receiver front end for millimeter-wave communications [1].

accommodate more carrier aggregation, these filters become more difficult to design. In this case, the topology in figure 1.1 b) can be employed where the filters are electrically isolated at the cost of more area. Nonetheless, both topologies force designers to fit a lot of filters into a very small area. Ideally, tunable filters could be used in instead to try to cover the spectrum required without occupying valuable space. This is of course pertaining to the frequency band of 3.5GHz to 6 GHz where the CA topology is still practical. If millimeter wave frequencies are used, designers will likely revert to the classic super-heterodyne receiver illustrated in Fig. 1.2. The front-end filtering in this case will have to be done by other means, mostly likely slow wave electromagnetic techniques as described in [3, 4, 5]. Acoustic filters will likely be employed for channel selection, since the signal is mixed down to a lower frequency at this stage. This is a function where effective tunable filters would still be very desirable.

A recent development in mobile communications is the introduction of non-magnetic circulators that are compatible with integrated circuits. This is an area rich in history and innovation, but without question, the most impactful is the development of spatio-temporal modulation-based

gyrators. This is a process in which a signal is modulated and de-modulated by staggered clocks so that forward and reverse transmission of the signal is non-reciprocal in phase. This technique has been notably used in [6, 7, 8] to demonstrate circulators at RF and millimeter wave frequencies. Similar techniques have also been used to create general non-reciprocal acoustic filters and circulators [9, 10, 11]. Figure 1.3 shows the implementation and performance of 171MHz and 1.95 GHz circulators using acoustic devices where low-loss and high isolation, two very important metrics for circulators, were achieved; demonstrating that acoustic technology can be used effectively in this application. An unfortunate drawback of some of these devices is the requirement of two high power synchronized clock signals. However, these results have galvanized the research community to further explore different methods of creating acoustic devices with non-reciprocity. Such devices can perform the duties of filtering and providing isolation which can greatly improve the performance of systems due to relaxed matching conditions, improved loss, and isolation between ports. Recently, asymmetrically transduced micro-resonators were demonstrated to result in non-reciprocal transmission of forward and reverse waves with 16 dB of isolation [12]. The insertion loss, however, is $-60dB$ making it impractical. The work in [10] achieve an insertion loss of $-5.6dB$ with an isolation of $15dB$, but the device requires four different clock signals for operation and a complex topology that will make it too large for mobile applications.

There also exists a long history of researchers trying to introduce gain, non-reciprocity, and tunability into acoustic devices using the acoustoelectric effect. This effect occurs when an acoustic wave is in close proximity to drift electrons in a semiconductor. When the electrons are accelerated beyond the phase velocity of the elastic wave, it will amplify the wave traveling in the same direction while attenuating waves in the opposite direction. This was first demonstrated in [13] on CdS acting as both the piezoelectric and semiconductor materials achieving greater than 38 dB gain. Later work showed high gain was also possible when separate materials were used for the piezoelectric and semiconductors such as LiNbO and Silicon [14, 15, 16, 17]. Although many successful experiments were demonstrated, it was never adopted practically due to high noise and the large required electric fields needed to produce gain [18, 19]. Recent efforts employing high

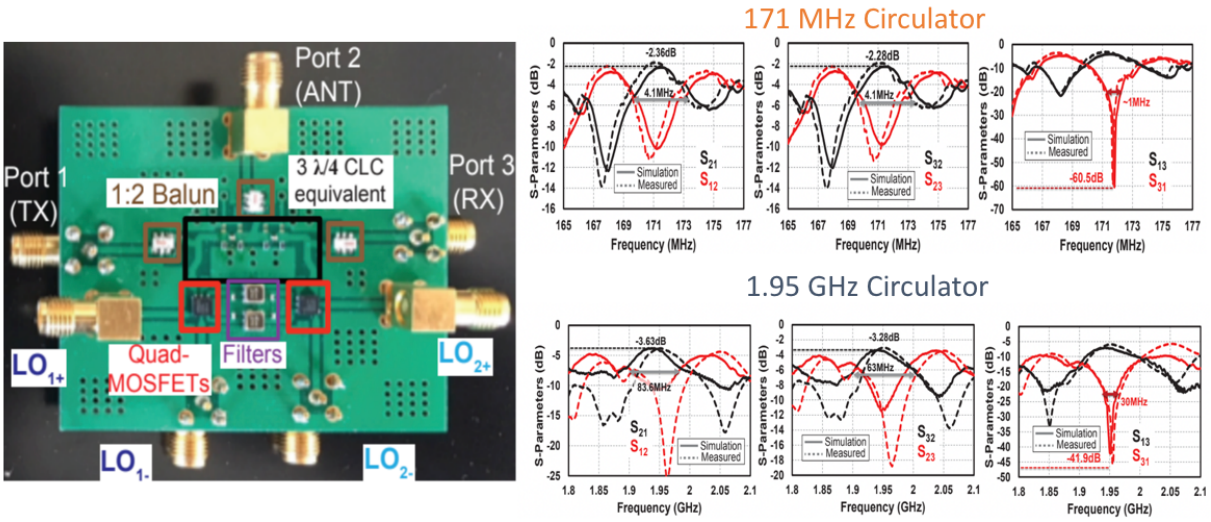

Figure 1.3: Left: PCB Circulator implemented with spatio-temporal modulation with acoustic filters. Right: Performance of 171 MHz and 1.95GHz circulators [11].

performance semiconductors such as GaN to lower the require electric field and reduce noise have been made [20, 21], however, the device still suffers from $-50dB$ of insertion losses.

This same effect can be used to create tunable acoustic filters, by using an electric field to modulate the stiffness of the piezoelectric material [22, 23], but with high insertion losses, low tuning values of $.02\%$, and large electric fields to initiate tuning, the devices never gained any further interest. Recently, efforts have been made to improve on past devices by using high performance semiconductors such as GaN [24, 25]. While these works were able to increase tunability up to $\%.09$, they still suffer from large losses and relatively high voltages for operation.

In this work, a new topology is introduced that unifies filtering, non-reciprocity, and tunability into a compact and simple design. This is achieved by a three-port asymmetrical design where the large delays available in acoustic technology are combined with a negative resistance to cause the constructive or destructive interference of reflected waves. This could potentially address the issues currently facing communications community concerning filtering, channel selection, carrier aggregation, and antenna interfaces.

1.1 Fundamentals of Acoustic Devices

Acoustic devices are based on the principles of elasticity and piezoelectricity. For the purposes of this work, it is useful to review these physical principles to better understand how acoustic waves are excited, induced, and detected in propagation media. In this spirit, first we will briefly review some the basics of elastic waves in solids and piezoelectricity.

1.1.1 Elastic Waves in Solids

Bulk acoustic waves (BAWs) are elastic waves propagating in solids. They are categorized as longitudinal or pressure waves demonstrated in Fig. 1.4 a) and transverse or shear waves shown in Fig. 1.4 b). These are identified by their displacement direction which is also known as the polarization. In the case of longitudinal waves, the polarization direction is parallel to the propagation direction whereas the transverse wave polarization is perpendicular to the propagation. When stress, a force commonly labeled as T and carrying the units N/m^2, is applied to the solid; it will experience strain or deformations proportional to the stress according the elasticity c of the material also known as Young's modulus with units of N/m^2. This relationship is stated by Hooke's law in 1.1 written in tensor form to accommodate all possible components of deformations or strain S.

$$\{T\} = \{c\} : \{S\} \tag{1.1}$$

The velocity of elastic waves are dependent on the density and stiffness of the material. For longitudinal waves and transverse waves, the velocities are given by

$$V_l = \sqrt{\frac{c_{11}}{\rho}}, \tag{1.2}$$

$$V_t = \sqrt{\frac{c_{44}}{\rho}}, \tag{1.3}$$

where c_{ij} is the stiffness constant of the material and ρ is the mass density.

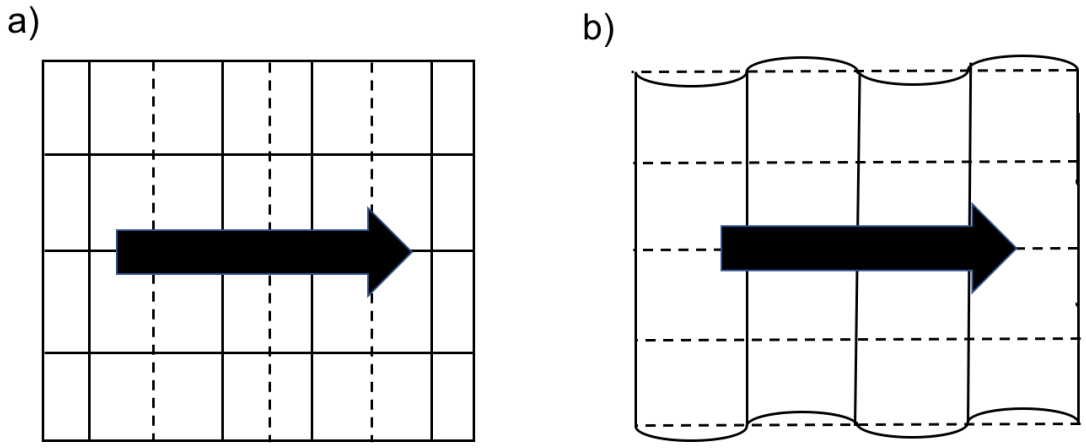

Figure 1.4: a) Longitudinal or pressure elastic waves in solids. These waves are associated with volume change of the material. b) Transverse or shear elastic waves in solids.

Like electromagnetic waves, the wavenumber or propagation constant, k, is given by

$$k = \frac{2\pi}{\lambda} \tag{1.4}$$

where λ is the wavelength, which is defined to be

$$\lambda = \frac{v}{f}, \tag{1.5}$$

where v is the velocity of the elastic wave and f is the frequency in Hertz.

Similar to electromagnetic waves, elastic waves also experience attenuation as it propagates through a medium. These are mainly due to two mechanisms: loss due to scattering caused by inhomogeneous material and loss resulting from scattering caused by thermal lattice vibrations. In the case of longitudinal waves, loss can also emerge from energy transportation by thermal diffusion to neutralize temperature variations caused by volume changes [26]. In both propagation modes, these losses become more severe as the wavelength approaches the size of the scatterers.

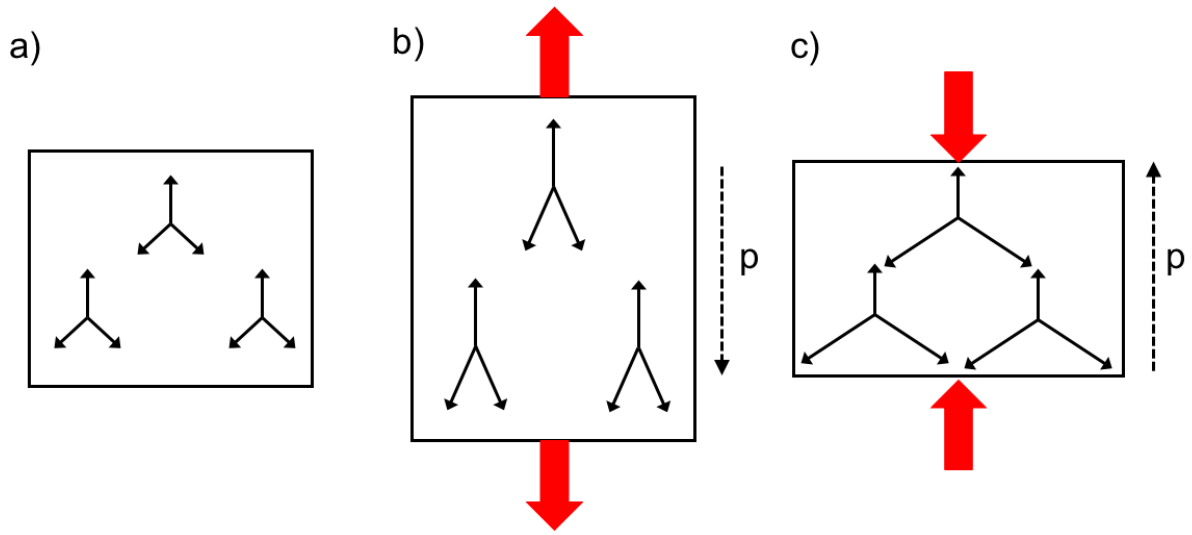

Figure 1.5: Trigonal structure. a) Equilibrium. b) Under tensile stress. c) Under compressive stress.

In other words, as the frequency increases, so will the loss.

1.1.2 Piezoelectricity

With a basic understanding of elastic waves in solids, now we can discuss how these waves can be converted in to electronic energy and vice versa. Consider Fig. 1.5 where a trigonal structure is placed under different forms of stress. Under equilibrium (Fig. 1.5a), no stress is applied therefore no net polarization appears. When a tensile stress is applied (1.5b), dipole moments displace resulting in a net polarization in the direction show. Similarly, under compressive stress (Fig. 1.5c) a net polarization appears in the opposing direction. Thus, the resulting polarization depends on the amplitude and direction of applied stress. Also, by applying an electric field instead of stress, the same mechanism results in the generation of strain proportional to the electric field. This characteristic of linear coupling between elasticity and electricity is called piezoelectricity.

In contrast, let us now consider a tetragonal structure Fig. 1.6. In every case, even though dipoles are moved under stress, no net polarization appears due to symmetric nature of the structure

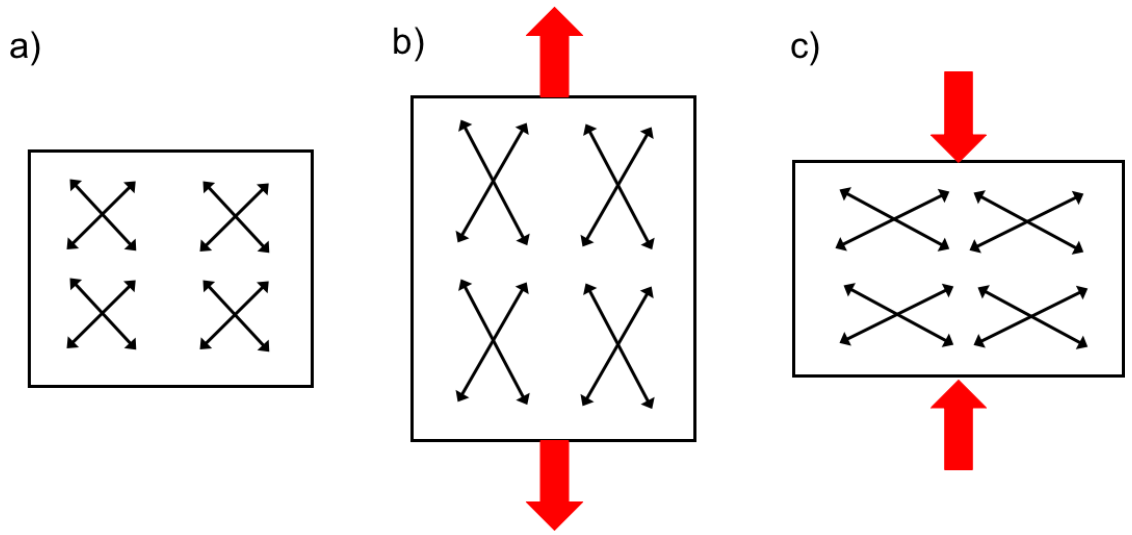

Figure 1.6: Tetragonal structure. a) Equilibrium. b) Under tensile stress. c) Under compressive stress.

revealing an important crystallographic requirement for piezoelectricity. In order for piezoelectricity to exist, the crystal structure of the material has to be asymmetric [26]. More specifically it has to be non-inversion symmetric.

Now let's consider the parallel capacitor in Fig. 1.7 where the dielectric layer is a non-piezo material. If an electric field is applied, charges of opposite polarity will accumulate at the surfaces of the capacitor. The surface charge density in $\frac{C}{cm^2}$ proportional to the electric field is related by

$$D = \epsilon_0 \epsilon_r E = \epsilon E, \tag{1.6}$$

where ϵ_r is the relative dielectric permittivity and ϵ_0 is the permittivity of free space (8.856 x $10^{-12} F/m$).

If the dielectric is piezoelectric, however, this relation no longer holds because of the net polarization that occurs. When an electric field is applied, it will result in deformations in the material. Thus, Eqn. 1.6 is modified to account for the coupling between electric and mechanical parameters

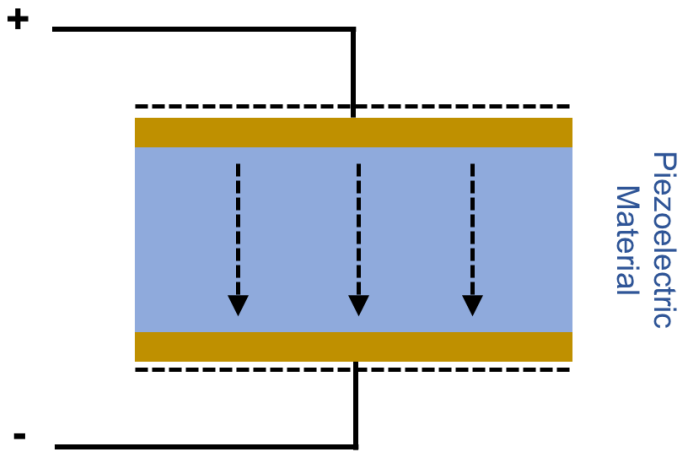

Figure 1.7: Parallel plate capacitor with piezoelectric material where strain is induced by an applied electric field.

as

$$D = [e][S] + [\epsilon]E, \tag{1.7}$$

where e is piezoelectric coupling term.

Equation 1.7 is a matrix equation employing the reduced coordinates for strain S in Eqn. 1.1. The displacement density term is then a three-dimensional one in x, y and z coordinates. Since the S term has six components from Eqn. 1.7, the piezoelectric constant terms in [e] will form a 3 X 6 matrix with 18 elements. The parameter $[\epsilon]$ relating dielectric permittivity is a 3 X 3 matrix with nine elements.

Revisiting Eqn. 1.7 to add the coupling between mechanical and electrical forces results in

$$[T] = [c][S] + [e^t]E \tag{1.8}$$

where e^t is the transpose of the piezoelectric constant e and is now a 3 x 6 matrix.

Equations 1.7 and 1.8 now represent the reciprocal conversion of electric to mechanical energy

and vice versa, demonstrating the piezoelectric action.

How much energy is converted between electrical and acoustic domains is one of the most important parameters along with its phase velocity v. The electromechanical coupling coefficient, K^2, is defined in terms of the piezoelectric coefficient e, elastic constant c, and dielectric permittivity ϵ as

$$K^2 = \frac{e^2}{c\epsilon}. \tag{1.9}$$

Tensor notation in Eqn. 1.9 is dropped since an appropriate calculation requires consideration of both propagation direction and crystal cut.

1.1.3 The Surface Acoustic Wave Equation

Elastic waves propagating in a piezoelectric medium are evaluated by the mechanical equations of motion coupled with Maxwell's equations to describe the corresponding electric field. The derivation process is complex and beyond the scope of our review of acoustic fundamentals, however, the result is a powerful one. The solution is that the electrical potential ,Φ, on the surface induced by a mechanical wave in a piezoelectric medium can be accurately described by the familiar traveling wave equation below

$$\Phi(x,t) =\mid \Phi \mid e^{j(\omega t-\beta x-\beta y)} \tag{1.10}$$

where β and λ share the same definitions previously stated and t is time. The coordinate x denotes the direction of propagation on the free surface as depicted in Fig. 1.8, while y denotes the depth of the saw wave in the piezoelectric substrate.

In most cases, it is suffice to only consider the traveling wave on the free surface. Thus Eqn. 1.10 becomes

$$\Phi(x,t) =\mid \Phi \mid e^{j(\omega t-\beta x)}. \tag{1.11}$$

.

In simple terms, equation 1.11 signifies that waves traveling in a piezoelectric medium is analogous to electromagnetic waves traveling on a transmission line. In fact, this turns to be incredibly

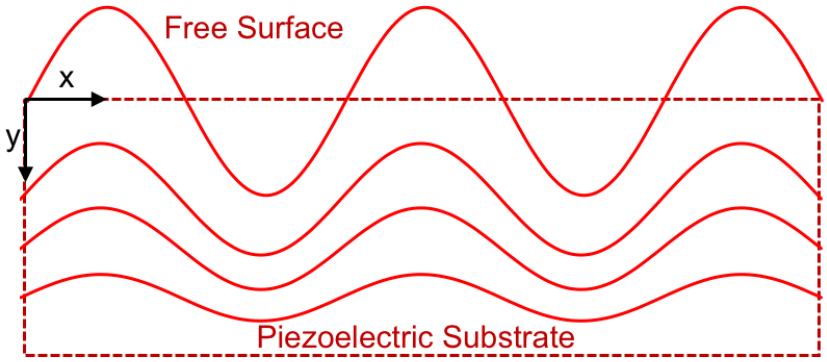

Figure 1.8: Surface acoustic wave traveling on the free surface of a piezoelectric substrate.

useful in modeling acoustic devices allowing the reformulation of transmission line modeling techniques for acoustic waves. This will be discussed more in detail in upcoming sections.

1.1.4 Surface Acoustic Wave Devices

SAW devices are usually composed of simple metal gratings on a piezoelectric material as depicted in Fig. 1.9. The metal gratings are used to apply the electric field at the surface to of the material to induce an elastic wave to travel. Each pair of metal gratings, known as interdigitated transducers (IDTs), are designed so that its periodicity in polarity results the desired frequency response. Figure 1.10 demonstrates the frequency response of SAW device similar to Fig. 1.9 on LiNbO where both IDTs have 24 pairs of transducers. The phase velocity of the LiNbO is $3780m/s$, width of the transducers are $4\mu m$, and periodicity is $16\mu m$ resulting in a center frequency of 236MHz. The group delay of the device is also geometrically defined by the gap between the transducers. This topology is commonly referred to as a transversal SAW filters or delay lines [27].

A drawback of these devices, however, is that IDTs induce acoustic waves to travel bi-directionally.

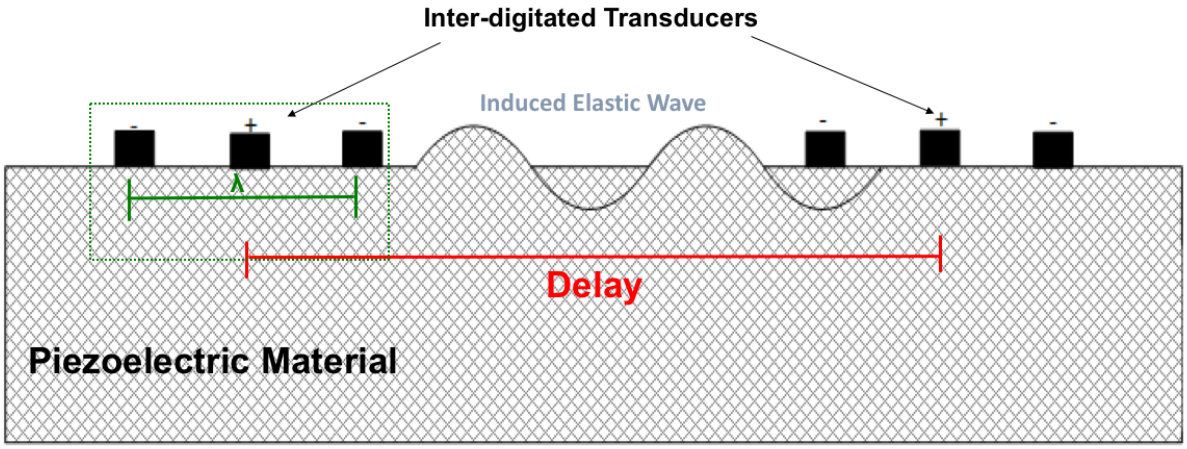

Figure 1.9: Two-port surface acoustic wave structure.

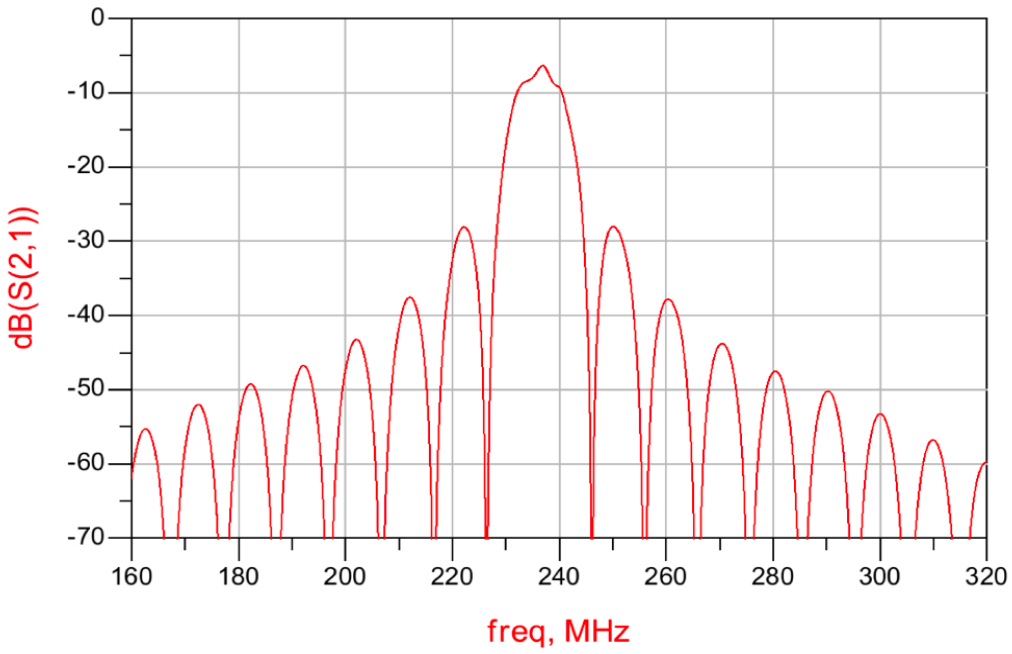

Figure 1.10: Frequency response of two port SAW device on LiNbO where the width of the transducers are $4\mu m$, and periodicity is $16\mu m$.

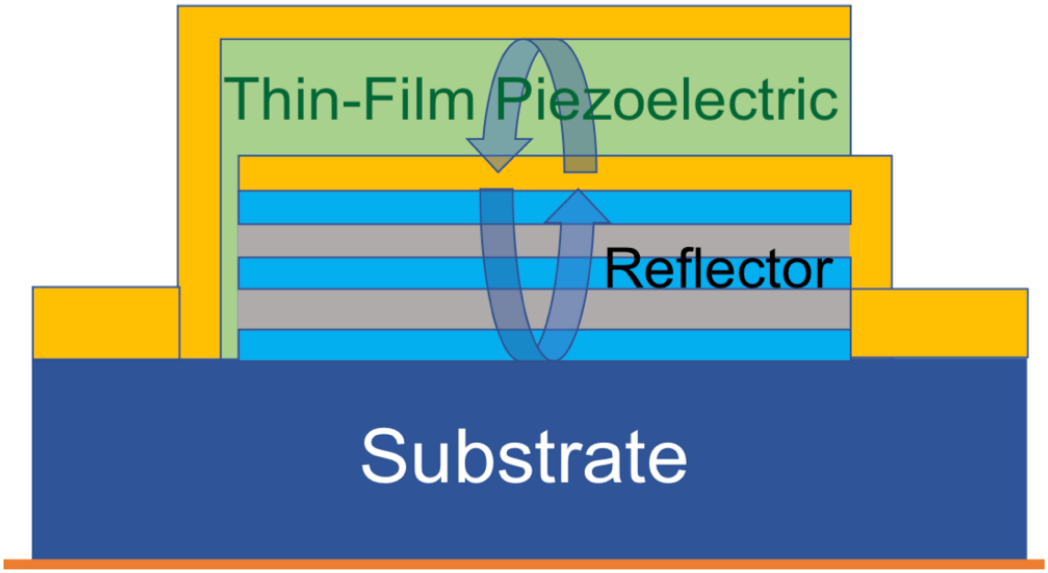

Figure 1.11: Cross section of bulk acoustic wave resonator with acoustic mirror.

This causes half of the power of the signal to be lost at each transducer interface meaning basic delay line filter as demonstrated in Fig. 1.9 has a minimum insertion loss of 6 dB. Techniques have been developed to combat bi-directional losses such as interdigital IDTs and reflector gratings [28, 29] and uni-directional transducers [30, 31, 32] which led to sub-3 dB insertion loss. Furthermore, IDTs can also be used as single frequency resonators to build ladder filters for high frequency operation and improved power handling compared to transversal filters [33]. These advances have led SAW devices to dominate RF front-end circuits.

1.1.5 Bulk Acoustic Wave Devices

While this work will primarily focus on transversal SAW filters, it important to briefly mention BAW technology due to the increase use in microwave frequencies and above. As new generations of mobile technology trend to operate at higher frequencies where SAW devices start to suffer from increase in insertion loss due to metallization resistance and propagation loss, BAW devices emerged as a low loss solution. Since the operating frequency of bulk modes are defined by the thickness of the piezoelectric, IDTs are not required to induce bulk modes circumventing metal-

lization loss due to the need for deep sub-micron SAW transducers. In this case, however, the structure behaves as a resonator where the resonant frequency is defined by

$$f_r = \frac{v_{BAW}}{2t} \tag{1.12}$$

where v_{BAW} is the phase velocity of BAW propagating mode and t is the thickness of the piezoelectric. Figure 1.11 illustrates a thin-film bulk acoustic resonator (TFBAR) with an acoustic mirror to increase quality factor. Topologies such as ladder filters and lattice filters use resonators at different frequencies as building blocks to create high performance filters [34]. These are now used widely as duplexers for antenna interfaces in LTE mobile communications systems [35] and have partially replaced SAW filters above and including microwave frequencies.

CHAPTER 2
A NOVEL NON-RECIPROCAL TOPOLOGY BASED ON ASYMMETRICAL TRANSMISSION LINES

Lorentz reciprocity is a fundamental characteristic shared by most electronic components. However, non-reciprocal devices such as isolators and circulators can provide new functionality in modern systems that can greatly improve performance. Reciprocity can be broken several different ways. One such way is by the Faraday effect where a strong magnetic field interacts with an electromagnetic wave modulating its phase velocity. This effect was used to create the first microwave gyrators, isolators, and circulators [36]. However, since these devices required a magnetic bias and are typically large, they have never been adopted in practical systems. Recently, researchers have exploited time-variant circuits to break reciprocity to make magnetic-free passive isolators, gyrators, and circulators in integrated circuit platforms [6, 7, 8, 9], but these devices rely on two or more high power clock signals with very precise phase relationships. Lastly, another effective wave of creating non-reciprocal devices is by the use of non-linearity. Active devices such as transistors can be used as amplifiers to create isolation and even circulators [37], but these run into added noise and limited power handling. In this section, we will introduce a new topology not only capable of non-reciprocity, but also one who's non-reciprocal properties can be tuned.

2.1 Phase Coherent Non-Reciprocity

To begin exploring this new topology, we will now derive the forward and reverse transmission S-parameters S_{21}, and S_{12} for the circuit illustrated in fig 2.1. Figure 2.1 illustrates a T-network where two transmission lines surround a current source. Each has 50Ω terminations. A 50Ω voltage source is also added for the derivation of S_{21}, and S_{12}.

Treating the transmission lines L1 and L2 as lossless, the current and voltages along L1 and L2

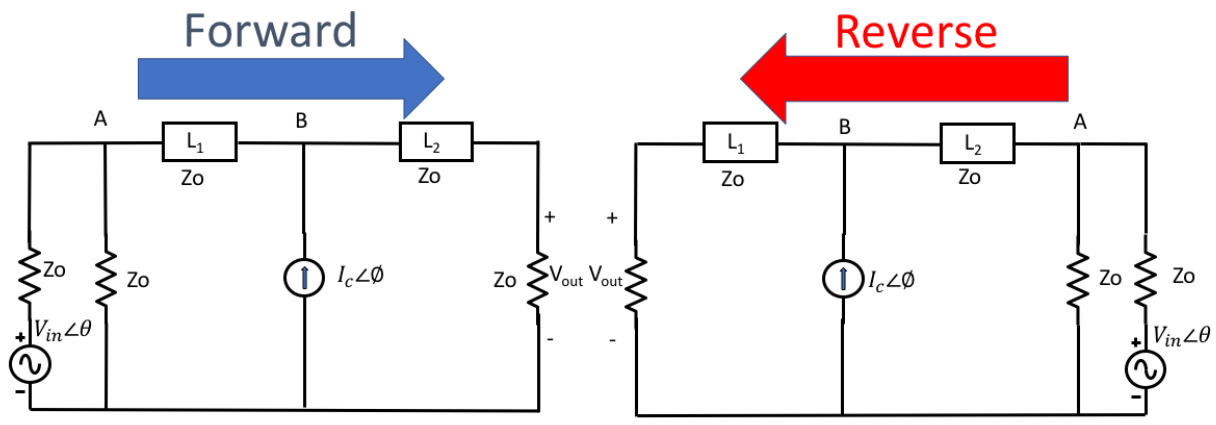

Figure 2.1: T-Network of two transmission lines surrounding a current source. Left: Set-up for derivation of forward transmission wave. Right: Set-up for derivation of reverse transmission wave.

can be expressed by the telegrapher's equations as

$$V(x) = V^+ e^{-j\beta x} + V^- e^{j\beta x} \tag{2.1}$$

and

$$V(x) = \frac{1}{Z_0}\left(V^+ e^{-j\beta x} - V^- e^{j\beta x}\right) \tag{2.2}$$

where Z_0 is the characteristic impedance of the transmission lines and β is the propagation constant which is equal to $\frac{2\pi}{\lambda}$ where λ is the wavelength. The variable x refers to the distance the voltage and current waveforms have traveled through the transmission lines. Starting with the derivations of the forward transmission as illustrated in fig. 2.1, applying Kirchhoff's Current Law,

the following equations can be written:

$$V_A = V_{L1}^{+} + V_{L1}^{-}, \tag{2.3}$$

$$V_B = V_{L1}^{+} e^{-j\beta l_1} + V_{L1}^{-} e^{j\beta l_1}, \tag{2.4}$$

$$V_B = V_{L2}^{+} + V_{L2}^{-} \tag{2.5}$$

$$V_{OUT} = V_{L2}^{+} e^{-j\beta l_2} + V_{L2}^{-} e^{-j\beta l_2}, \tag{2.6}$$

$$V_{IN} e^{-j\theta} - 2V_A = V_{L1}^{+} - V_{L1}^{-}, \tag{2.7}$$

$$\frac{1}{Z_0}\big(V_{L1}^{+} e^{-j\beta l_1} + V_{L1}^{-} e^{j\beta l_1}\big) + I_C e^{-j\phi} = \frac{1}{Z_0}\big(V_{L2}^{+} - V_{L2}^{-}\big), \tag{2.8}$$

$$V_{L2}^{+} e^{-j\beta l_2} - V_{L2}^{-} e^{j\beta l_2} = 2V_{OUT}, \tag{2.9}$$

and

$$I_{OUT} = \frac{V_{OUT}}{Z_0} \tag{2.10}$$

where L_1 and L_2 are the lengths of the transmission lines.

Solving for this system of equations, we can now find an expression for $S_{21} = 2\frac{V_{OUT}}{V_{IN}}$ as

$$S_{21} = \frac{-2\big(2V_{IN} e^{-j\theta} - Z_0 I_C e^{-j(\phi+\beta L_1)} + 3Z_0 I_C e^{j(\beta L_2 - \phi)}}{V_{IN} e^{-j\beta(L_1+L2)} - 9e^{j\beta(L_1+L2)}}. \tag{2.11}$$

Setting $\theta = \phi = 0$, equation 2.11 can be re-written as

$$S_{21} = \frac{-2\big(2V_{IN} - Z_0 I_C e^{-j(\beta L_1)} + 3Z_0 I_C e^{j(\beta L_2)}}{V_{IN} e^{-j\beta(L_1+L2)} - 9e^{j\beta(L_1+L2)}}. \tag{2.12}$$

Repeating this process for the reverse case and again setting $\theta = \phi = 0$, S_{21} can be written as

$$S_{12} = \frac{-2\big(2V_{IN} - Z_0 I_C e^{-j(\beta L_2)} + 3Z_0 I_C e^{j(\beta L_1)}}{V_{IN} e^{-j\beta(L_1+L2)} - 9e^{j\beta(L_1+L2)}}. \tag{2.13}$$

These equations can be further simplified by setting the length of both transmission lines to λ. Since $\beta = \frac{2\pi}{\lambda}$, the terms $e^{\pm j(\beta L_{1,2})}$ now simplify to 1. Now equations 2.12 and 2.13 can be written as

$$S_{21} = \frac{2V_{IN} - Z_0 I_C + 3Z_0 I_C}{4V_{IN}} \tag{2.14}$$

and

$$S_{12} = \frac{2V_{IN} - Z_0 I_C + 3Z_0 I_C}{4V_{IN}}. \tag{2.15}$$

Upon visual inspection of 2.14 and 2.15, they are perfectly reciprocal in nature. However, if the lengths of the transmission lines are now changed to $L_1 = \frac{\lambda}{2}$ and $L_2 = \lambda$, an interest thing occurs. There now exists a sign flip as a result of $e^{-j(\beta L_1)} = -1$ and $e^{-j(\beta L_2)} = 1$. Keeping $\theta = \phi = 0^\circ$, S_{21}, equations 2.12 and 2.13 are re-written as

$$S_{21} = \frac{-2(2V_{IN} + (Z_0 I_C + 3Z_0 I_C))}{9V_{IN}} \tag{2.16}$$

and

$$S_{12} = \frac{-2(2V_{IN} - (Z_0 I_C + 3Z_0 I_C))}{9V_{IN}}. \tag{2.17}$$

The sign flip now causes a non-reciprocal transmission to occur dependent on the relationship of the input signal V_{IN} and the current source I_C. If the magnitude of the input voltage is equal to the voltage produced by the current source represented by the remaining two terms in the nu-

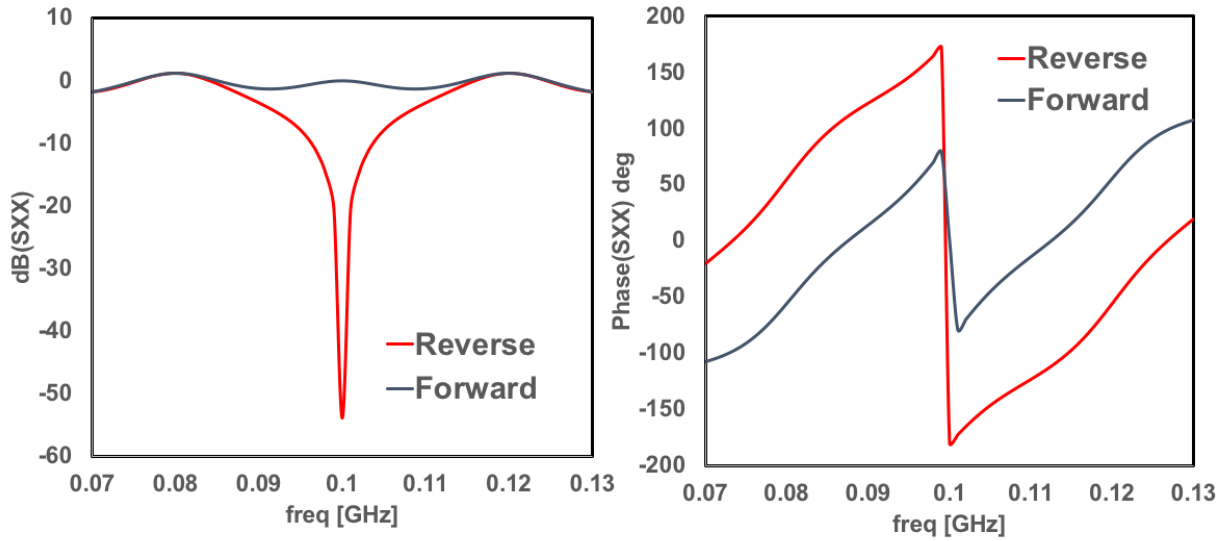

Figure 2.2: Evaluation of equations 2.16 and 2.17 demonstrating general non-reciprocity for the case $V_{IN} = \frac{Z_0 I_C + 3 Z_0 I_C}{2}$ and $\theta = \phi = 0°$. Left: Magnitude in dBm of forward and reverse transmission S-parameter terms. Right: Phase of forward and reverse transmission S-parameter terms.

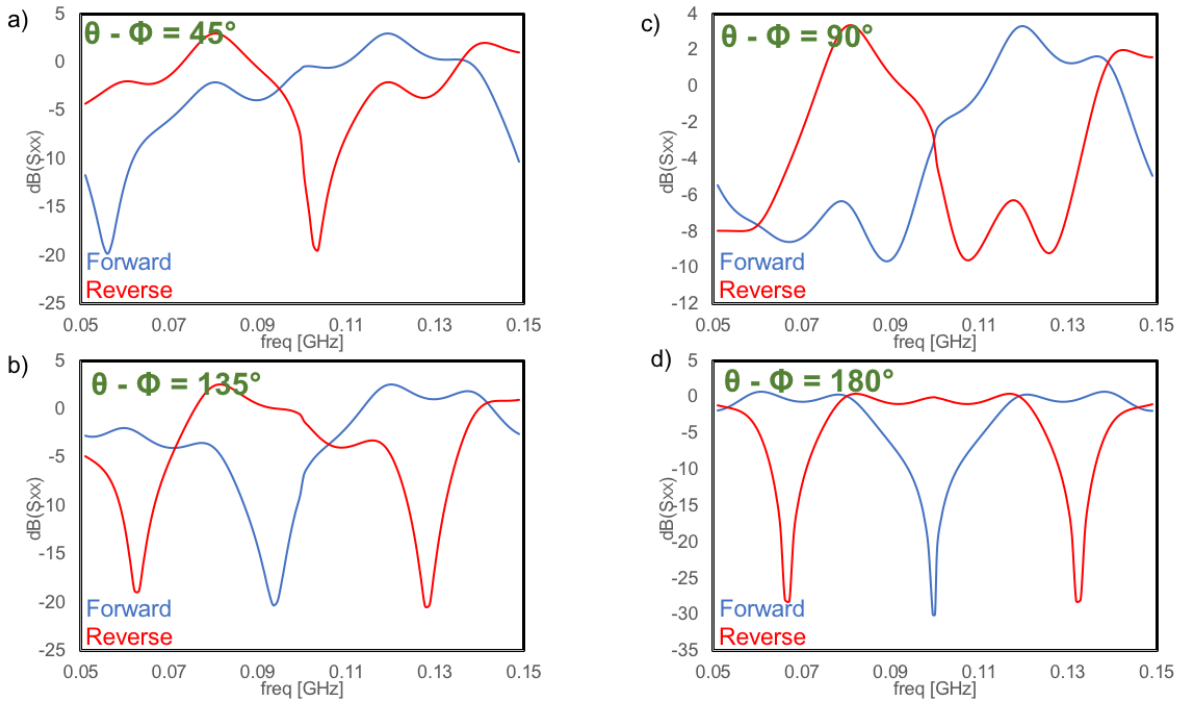

Figure 2.3: Evaluation of equations 2.16 and 2.17 demonstrating dependency of phase relationship between input signal, V_{IN}, and current source I_C for the case $V_{IN} = \frac{Z_0 I_C + 3 Z_0 I_C}{2}$. a) $\theta - \phi = 45°$. b) $\theta - \phi = 90°$ c) $\theta - \phi = 135°$. d) $\theta - \phi = 180°$.

merator, in other words when $V_{IN} = \frac{Z_0 I_C + 3 Z_0 I_C}{2}$, and a wavelength of transmission lines are taken at 100 MHz, equations 2.16 and 2.17 result in a frequency response to that of an isolator. Figure 2.2 demonstrates this case. As seen here, at the center frequency, S_{21} exhibits no loss meaning the input signal travels to the output port unimpeded. In the reverse case, S_{12}, the input signal is perfectly canceled out by the current source terms.

It is important to note that this response is dependent on the phase relationship between the input signal and the current source as seen empirically in equation 2.12. The results in Fig. 2.2 are for the case in which $\theta - \phi = 0°$, but an interesting thing occurs when this is changed. Figure 2.3 demonstrates the magnitude in dB of S_{21} and S_{12} for different phase relationships of input signal and current source. As seen here, the isolation frequency changes according to the phase until the isolation behavior is completely reversed as in the case when the phase difference is $180°$. This can function as a means of tuning the center transmission and isolation frequencies.

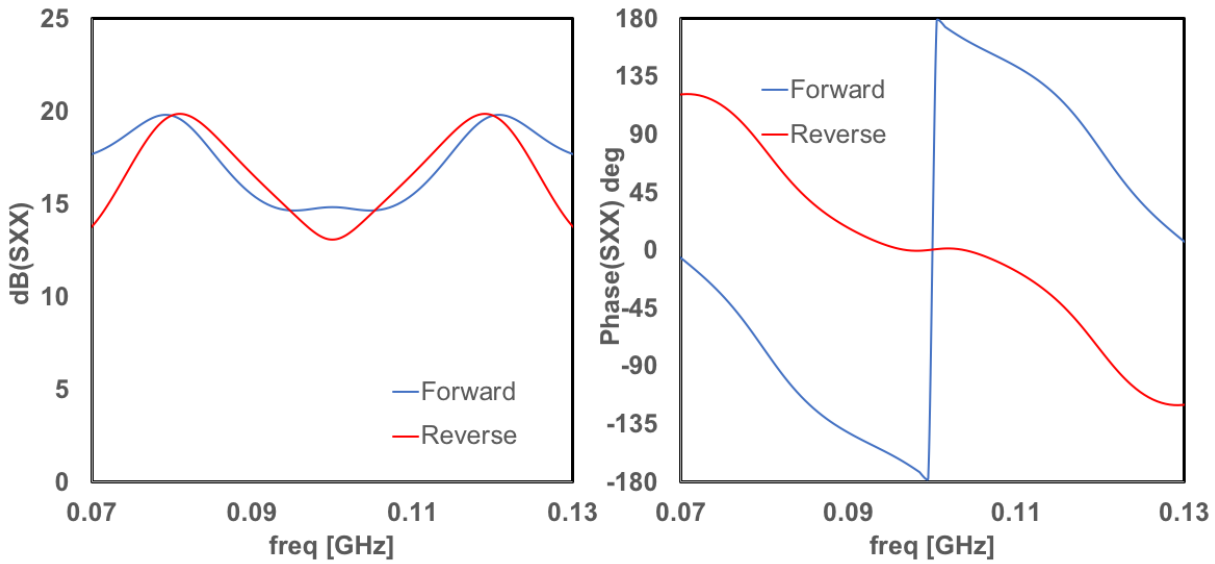

Figure 2.4: Evaluation of equations 2.16 and 2.17 demonstrating general non-reciprocity for the case $V_{IN} \ll \frac{Z_0 I_C + 3 Z_0 I_C}{2}$ and $\theta = \phi = 0°$. Left: Magnitude in dBm of forward and reverse transmission s-parameter terms. Right: Phase of forward and reverse transmission S-parameter terms.

2.2 Phase Non-Reciprocity Functionality for Phase Incoherent Operation

Figures 2.2 and 2.7 show non-reciprocal transmission between forward and reverse EM waves for the case $V_{IN} = \frac{Z_0 I_C + 3 Z_0 I_C}{2}$, however, if the magnitude of the current source is increased far beyond that of the input signal, the behavior changes. Figure 2.4 demonstrates the magnitude and phase of the forward and reverse S-parameters for the case $V_{IN} \ll \frac{Z_0 I_C + 3 Z_0 I_C}{2}$. In this instance, the magnitude of the current source results in overall gain of both S_{21} and S_{12}. While some non-reciprocal gain is observable, there is not enough isolation to be deemed useful, however, again due to the sign flip caused by the difference in transmission line lengths, there is a $180°$ phase difference between S_{21} and S_{12} at the center frequency. This behavior is similar to that of a gyrator originally proposed by Tellegen in [38].

A gyrator is a two-port network whose S-parameter are given by

$$S_{gyrator} = \begin{pmatrix} 0 & -1 \\ 1 & 0 \end{pmatrix}. \tag{2.18}$$

S_{11} and S_{22} are perfectly matched while there is a 180° phase difference between S_{21} and S_{12}. Gyrators are the most widely used element to create isolators and circulators. In this case, we have a gyrator where the forward and reverse waves are also amplified. Assuming the ports are matched, the s-parameters for the topology discussed when $V_{IN} \ll \frac{Z_0 I_C + 3 Z_0 I_C}{2}$ are

$$S = \begin{pmatrix} 0 & -\alpha \\ \alpha & 0 \end{pmatrix}, \tag{2.19}$$

where α is the gain factor. Utilizing this gyrator, a three-port circulator can be implemented by the addition of $\frac{\lambda}{4}$ transmission lines as illustrated in Fig. 2.5. Terminating Port 3 to 50Ω results in an isolator, whose s-parameters are demonstrated in Figure 2.6 for different values of α. When $\alpha = 1$, the structure behaves as a perfect isolator. When $\alpha = 2$ and $\alpha = 3$, S_{21} experiences a gain of near +10 dB while S_{12} experiences attenuation. When $\alpha = 4$, an unequal amount of reverse gain is observed. These results suggest that this structure can function as a unilateral amplifier with proper selection of α.

Furthermore, as in the previous case, the center frequency can be changed via the phase of the current source. Since in the case $V_{IN} \ll \frac{Z_0 I_C + 3 Z_0 I_C}{2}$, the current source dominates thus, the phase of V_{IN} does not play a role in the frequency response. Thus, the magnitude and phase of the forward and reverse s-parameters are determined by the current source. Any adjustment to the phase of the current source results in a direct phase shift from 180°. Figure 2.7 demonstrates the phase of equations 2.16 and 2.17 for different phases of the current source. As the phase is changed, the frequency at which the phase difference between S_{21} and S_{12} is 180° is also changed until the transmission is completely reversed as in the case when $\phi = 180^\circ$.

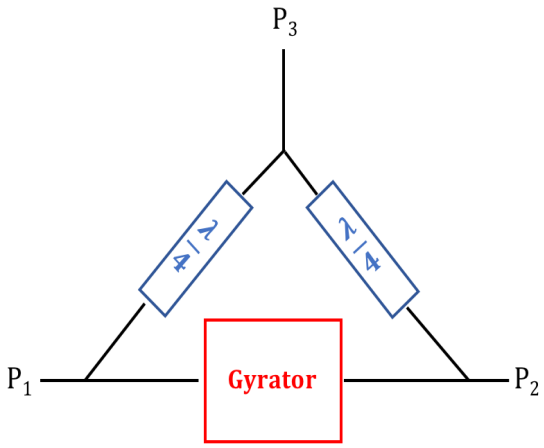

Figure 2.5: S-parameters of Isolator utilizing gyrator from Eq. 2.19.

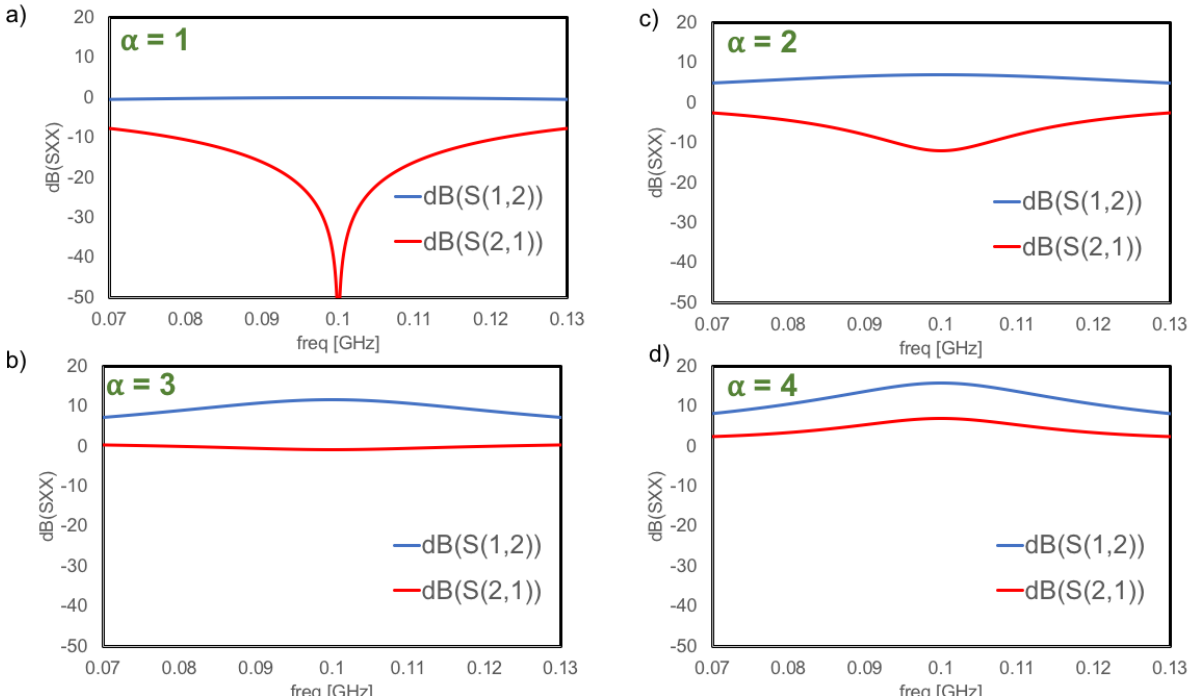

Figure 2.6: S-parameters of Isolator utilizing gyrator from Eq. 2.19 in the circuit configuration displayed in Fig. 2.5. a) Gain factor $\alpha = 1$. b) Gain factor $\alpha = 2$. c) Gain factor $\alpha = 3$. Gain factor $\alpha = 4$.

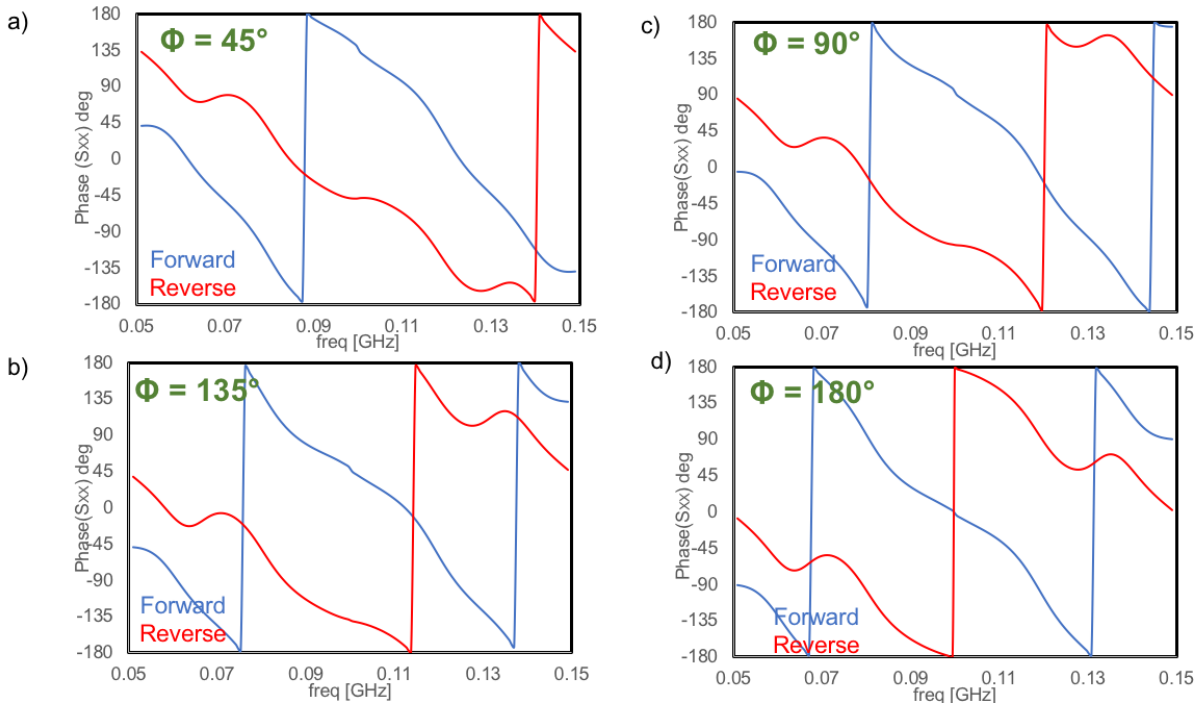

Figure 2.7: Evaluation of equations 2.16 and 2.17 demonstrating dependency of phase relationship between input signal, V_{IN}, and current source I_C for the case $V_{IN} \ll \frac{Z_0 I_C + 3 Z_0 I_C}{2}$. a) $\phi = 45°$. b) $\phi = 90°$ c) $\phi = 135°$. d) $\phi = 180°$.

2.3 The Current Source: Negative Resistance Parametric Amplification

In the previous section, a simple topology has been described capable of non-reciprocity functionality that can be either phase coherent or incoherent dependent on the magnitude of the current source. This current source is assumed to be at the same frequency and phase synchronized to the incoming signal. Up to this point, there has been no discussion as to how such a current source is achieved. In this section, we will describe a method of doing so by means of parametric amplification.

2.3.1 Parametric Amplification

Parametric amplification is a non-linear, time-varying process by which RF to RF power conversion can be achieved. This was first proposed by Manley and Rowe in [39], where they analyzed the power flowing in and out of a non-linear reactance pumped by a large signal. Their analysis

is based on the circuit illustrated in fig. 2.8. The signal source, f_s is a small signal in which amplification is desired. The signal frequency, f_p, is a large signal and is referred to as the pump frequency and supplies the power that will be used to amplify f_s. The nonlinearity of the reactance will cause mixing products of f_s and f_p to appear, hence each branch of the circuit, except that of the nonlinear capacitor, contains an ideal filter that only supports the various sums and differences that arise. Under these conditions, Manley and Rowe derived the power relations 2.20 and 2.21 .

$$P_{m,n} = \sum_{n=-\infty}^{\infty} \sum_{m=-\infty}^{\infty} \frac{mP_{n,m}}{mf_1 + nf_2} = 0 \tag{2.20}$$

$$P_{m,n} = \sum_{n=-\infty}^{\infty} \sum_{m=-\infty}^{\infty} \frac{nP_{n,m}}{mf_1 + nf_2} = 0 \tag{2.21}$$

$P_{m,n}$ is defined to be the power flowing into the reactance at frequency mf_1 and nf_2. Thusly, the sign convention follows that if $P_{m,n}$ is negative, the power is flowing out of the reactance.

The value of these relations is best demonstrated by several cases in which power is only allowed to flow in these frequencies. Let f_1 be the signal source and f_2 by the pump source. If power is allowed to flow at f_3 and $f_3 = f_1 + f_2$, then 2.20 becomes

$$\frac{P_1}{f_1} + \frac{P_3}{f_3} = 0 \tag{2.22}$$

and 2.22 becomes

$$\frac{P_2}{f_2} + \frac{P_3}{f_3} = 0. \tag{2.23}$$

Since the signal generator P_1 is delivering power to the nonlinear capacitor, it has a positive sign. Thus, from 2.22, P_3 must be negative, signifying that power is flowing from the capacitor to the termination. The power gain can be derived from 2.22 as

$$gain_{1-3} = \frac{f_3}{f_1}. \tag{2.24}$$

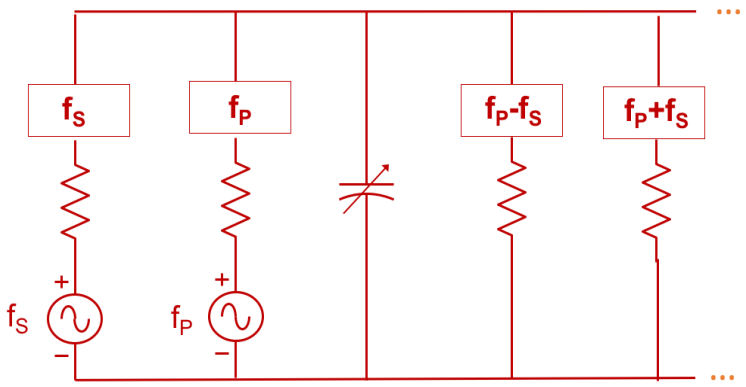

Figure 2.8: Circuit used by Manley-Rowe to derive the power flow relations of an isolated nonlinear capacitor.

The signal frequency experiences an up-conversion in frequency with gain, this case is known as the up-converting parametric amplifier. Although in practice, a proper derivation of gain includes parasitic elements and losses, these Manley-Rowe relations offer a general characterization of the behavior of these circuits.

Another example of how these systems can operate is the case that if the pump frequency, f_2, is the sum of f_1 and f_3 where f_1 is the signal frequency and f_3 is the output frequency. Since P_2 is delivering power to the reactance, following equations 2.20 and 2.21, P_1 and P_3 are negative. Meaning power is flowing from the reactance to the terminations tunes to f_1 and f_3. If the gain of the system is defined as the ratio of power delivered to the source by the reactance to that of the power provided by the source to the reactance, then it is possible for there to be infinite gain which can lead to instability. This type of parametric device is known as a negative-resistance parametric amplifier (NRPA) since it amplifies the incoming signal without any frequency conversion.

There are two types of NRPAs depending on the selection of frequencies that generally satisfy f_1+f_3=f_2, where f_2 is the pump frequency. The first is the case where $f_1 = f_3$ or $f_2 = 2 \times f_1$. In this case the idler frequency, f_3, is equal to f_1 so the phase relationship between the signal and idler frequency significantly impacts gain. This is known as the phase-coherent degenerate amplifier.

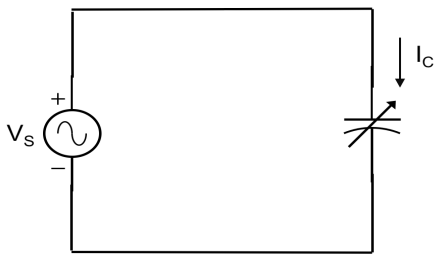

Figure 2.9: Circuit for derivation of current flowing into a nonlinear capacitor.

The second type is the case where $f_1 \neq f_3$. Here, the phase relationship between the idler and signal frequencies do not impact gain, however, as stipulated by Manly and Rowe, an extra circuit is required to support power flow at the idler frequency. This is known as the non-degenerate amplifier.

2.3.2 Emergence of Negative Resistance: Time Domain Analysis

Although the Manley-Rowe relations demonstrate that negative resistance is possible under certain conditions, it is useful to derive how negative resistance emerges from a pumped nonlinear capacitor. Figure 2.9 illustrates the circuit used for the derivation of the capacitor current I_C. The voltage source V_S is defined as $V_S = A\sin(\omega_S t + \theta)$, where A is the amplitude, ω_S is the signal frequency, and θ is the phase. The pumped nonlinear capacitor is modeled by a setting the Capacitance C to $C = C_0 + C_M \sin(\omega_P t + \phi)$, where C_0 is the static capacitance, C_M is the magnitude by which the capacitance changes in time, ω_P is the pump frequency, and ϕ is the phase of the pump source. The current of the capacitor can be written as

$$I_C = \frac{d}{dt}\Big[\big(C_0 + C_M \sin(\omega_P t + \phi) \times A\sin(\omega_S t + \theta)\big)\Big]. \tag{2.25}$$

Taking the time derivative, eqn. 2.25 becomes

$$I_C = A\omega_S \cos(\omega_S t{+}\theta){+}\frac{AC_M}{2}\big([\omega_S{+}\omega_P]\sin(\omega_S t{+}\omega_P t{+}\phi{+}\theta){+}[\omega_S{-}\omega_P]\sin(\omega_P t{-}\omega_S t{+}\theta{+}\phi)\big). \tag{2.26}$$

For simplicity, lets focus on the degenerate case where $\omega_P = 2\omega_S$. Equation 2.26 can now be written as

$$I_C = A\omega_S \cos(\omega_S t + \theta) + \frac{AC_M}{2}\big([3\omega_S]\sin(3\omega_S t + \phi + \theta) - [\omega_S]\sin(\omega_S t + \theta + \phi)\big). \quad (2.27)$$

Equation 2.27 shows now the emergence of a terms existing at ω_S and $3\omega_S$. The term at $3\omega_S$ would be suppressed by circuity in a practical case, so we can focus on the other terms only as shown in eqn. 2.28.

$$I_C = A\omega_S \cos(\omega_S t + \theta) - \frac{AC_M\omega_S}{2}\sin(\omega_S t + \theta + \phi). \quad (2.28)$$

As seen here, the first term is 90° out of phase with the source signal so it does not contribute to power. The negative sign on the second term signifies that this current is flowing out of the capacitor instead of being absorbed by it. This means that the nonlinear reactance gives rise to a negative resistance which reflects the incoming signal back as an amplified, phase-shifted version. This can be modeled as a current source expressed by the second term in eqn. 2.28, signifying that a NRPA can function as the current source in the topology proposed in the previous section.

2.3.3 Gain of Negative Resistance Amplifiers

Equation 2.28 yields a simple expression of the gain that results from the nonlinear capacitor. To get a more realistic view of the gain to include losses from the circuitry and capacitance, a more rigorous derivation is required. Following the method in [40], let us consider the circuit in figure 2.10. The pump circuit is omitted in this case and instead a time-varying capacitance is used for simplicity where the frequency of at which it is modulated is ω_P.

From the work of Manley-Rowe in [39], given a nonlinear capacitor $C(t) = C_0(1+2\gamma_1 cos(\omega_P t)+ 2\gamma_2 cos(2\omega_P t))$ where C_0 is the static capacitance and $2\gamma_1$ is the change in capacitance analogous to C_M in our previous derivation, the impedance matrix for the nonlinear capacitor when are there

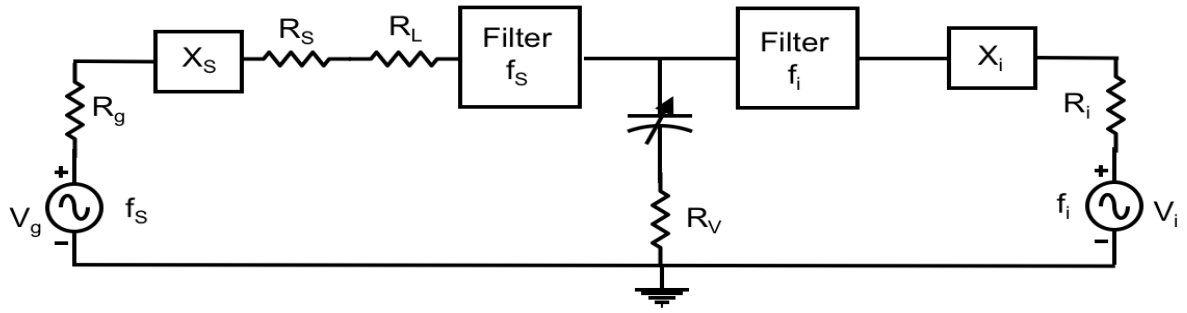

Figure 2.10: Circuit used for derivation of transducer gain of negative resistance parametric amplifiers.

up to three signals of significant voltage present is

$$\begin{bmatrix} V_1 \\ V_2^* \end{bmatrix} = \begin{bmatrix} \frac{1}{j\omega_1 C} & \frac{\gamma}{j\omega_2 C} \\ \frac{-\gamma}{j\omega_1 C} & \frac{-1}{j\omega_1 C} \end{bmatrix} \begin{bmatrix} I_1 \\ I_2^* \end{bmatrix} \tag{2.29}$$

where $\gamma = \gamma_1$, $C = C_0(1 - \gamma_1^2)$ for short circuited harmonics and $\gamma = \gamma_1(1 + \gamma_1^2)(1 - \gamma_2)$, $C = C_0(1 - 2\gamma_1^2)$ for open-circuited harmonics.

When the non-linear capacitor is pumped at frequency ω_P, two currents at the signal frequency ω_S and the idler signal ω_i. The idler is a mixing product of the input signal and the pump whose frequency can be defined to be as $\omega_i = \omega_P - \omega_S$. Thus, we can choose to find the transducer gain of the signal at ω_S and ω_i. We are only interested in transducer gain of the signal frequency ω_S, so we will focus our efforts on deriving the transducer gain for this signal.

The transducer gain is defined as the ratio of the power output $|I_L|^2 R_L$ divided and the available power input given by $\frac{|V_g|^2}{4R_g}$. To obtain an expression for the transducer gain in figure 2.10, the current must be written in terms of the source V_g. This is simplified by adding the external circuit impedances (R_g, R_l) to the effective self-impedances of the non-linear element by using the

impedance matrix formulation. The impedance matrix equations for the circuit in figure 2.10 can be written as

$$\begin{bmatrix} V_g \\ V_i \end{bmatrix} = \begin{bmatrix} Z_{11} + Z_{T1} & Z_{12} \\ Z_{21} & Z_{22} + Z_{T2} \end{bmatrix} \begin{bmatrix} I_g \\ I_i \end{bmatrix} \tag{2.30}$$

where $Z_{T1} = X_1 + R_g + R_L + R_V + R_1$ and $Z_{T2} = X_2 + R_V + R_i$. Series impedances X_1 and X_2 are used for matching purposes.

In the case of obtaining the transducer gain at the signal frequency ω_S by setting V_i to zero, the current I_g can be written as

$$I_g = \frac{V_{g1}(Z_{22} + Z_{T2})}{(Z_{11} + Z_{T1})(Z_{22} + Z_{T2}) - Z_{12}Z_{22}} \tag{2.31}$$

The transducer gain can now be obtained by the ratio of power dissipated in R_L to the power available at ω_1.

$$g_t = \frac{4R_g R_L \mid I_g \mid^2}{\mid V_{g1} \mid^2} \tag{2.32}$$

which becomes

$$g_t = \frac{4R_g R_L \mid (Z_{22} + Z_{T2}) \mid^2}{\mid (Z_{11} + Z_{T1})(Z_{22} + Z_{T2}^{)} - Z_{12}Z_{21} \mid^2}. \tag{2.33}$$

If we apply the matching conditions of $Z_{11} = -X_1$ and $Z_{22} = -X_2$, the transducer gain becomes

$$g_t = \frac{4R_g R_L}{(R_{T1} - \frac{\gamma^2}{\omega_1 \omega_2 C^2 R_{T2}})^2}. \tag{2.34}$$

An important result to note in 2.34 is the negative sign in the denominator. This allows the gain to be arbitrarily large and in fact oscillate. The negative resistance can be expressed as

$$-R = -\frac{\gamma^2}{\omega_1 \omega_2 C^2 R_{T2}}. \tag{2.35}$$

In practice, these types of amplifiers are operated near oscillation to obtain high gain, however, extreme care must be taken to verify stability throughout the impedance conditions being used. Circulators and oscillators can aid significantly in stabilizing the input and output impedances and also help separate between input and output signals since another characteristic of these amplifiers is its bilateral nature.

Equation 2.34 describes the gain of the amplifier at the signal frequency ω_1, but as mentioned earlier, we can also choose to analyze the amplification of the signal at frequency ω_2 for the non-degenerate case. Again setting $V_{g2}^* = 0$, I_2 can be written as

$$I_2 = \frac{-Z_{21}V_{g1}}{(Z_{11} + Z_{T1})(Z_{22} + Z_{T2}^*) - Z_{12}Z_{22}}. \tag{2.36}$$

The transducer gain thus becomes

$$g_t = \frac{4R_gR_L \mid I_2 \mid^2}{\mid V_{g1} \mid^2} \tag{2.37}$$

which can be written as

$$g_t = \frac{4R_gR_2 \mid Z_{21} \mid^2}{\mid (Z_{11} + Z_{T1})(Z_{22} + Z_{T2}^*) - Z_{12}Z_{21} \mid^2}. \tag{2.38}$$

At resonance, the transducer gain becomes

$$g_t = \frac{\omega_2}{\omega_1}\frac{4R_gR_2R}{R_{T2}(R_{T1} - R)^2}. \tag{2.39}$$

The appearance of the negative sign in the denominator again represents the negative resistance -R that causes amplification. In this case, however, the signal frequency ω_2 arises from the mixing of the pump signal and the signal frequency ω_1. Thus, in this case we have a negative resistance converter whose gain is particularly dependent on the choice of pump frequency.

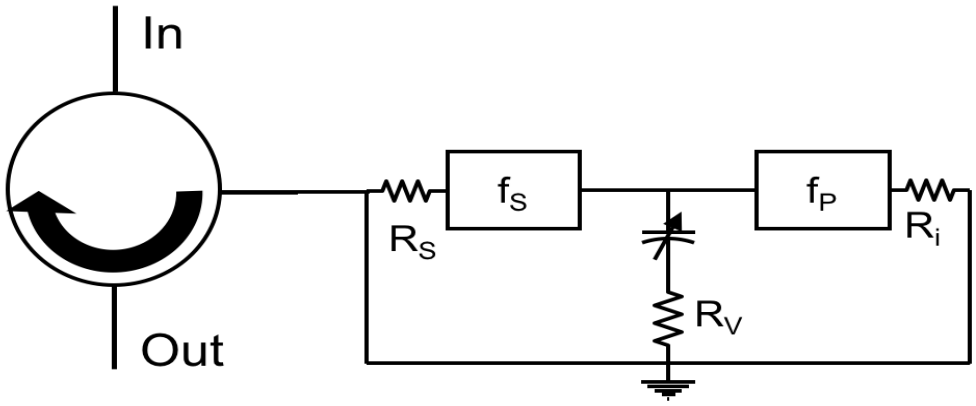

Figure 2.11: Configuration of parametric amplifier with a circulator.

2.3.4 Noise of Negative Resistance Amplifier

To aid in the derivation of noise figure, the circuit in figure 2.11 is assumed. The use of the circulator makes the circuit behave like a unilateral amplifier, greatly simplifying the derivation process. Furthermore, since in this work we intend to connect a parametric amplifier to structure that results in non-reciprocity, this simplification is appropriate. Utilizing the same methods to derive the transducer gain, the noise power at the outputs designated as ports In and Out in 2.11 are

$$N_1 = \frac{e_1^2(Z_{22} + Z_{T1})(Z_{22} + Z_{T2})}{(Z_{11} + Z_{T1})(Z_{22} + Z_{T2}) - Z_{12}Z_{22}} \tag{2.40}$$

$$N_2 = \frac{e_1^2 R_g \mid Z_{12} \mid^2}{(Z_{11} + Z_{T1})(Z_{22} + Z_{T2}) - Z_{12}Z_{22}}. \tag{2.41}$$

The noise figure is given by

$$F = \frac{N_1 + N_2}{g_a k T_0 B} = \frac{1}{g_a k T_0 B}(e_1^2 + e_2^2(\frac{\mid Z_{12} \mid^2}{\mid Z_{22} + Z_{T2} \mid^2})) \tag{2.42}$$

where $e_1^2 = 4kB(T_0R_g + T_dR_S + T_1R_S)$ and $e_2^2 = 4kB(T_dR_V + T_dR_V + T_2R_i)$.

At resonance, where $R_{T2} = Z_{22} + Z_{T2}$, the noise figure can be written as

$$F = 1 + \frac{T_1}{T_0}\frac{R_S}{T_g} + \frac{T_d}{T_0}\frac{R_V}{R_g} + \frac{\omega_1}{\omega_2}\frac{R}{R_g}\frac{1}{T_0}\frac{T_dR_V + T_2R_i}{R_{T2}} \tag{2.43}$$

While some intuition can be gained from equation 2.43, it is worth obtaining an expression for the minimum noise figure and the conditions required to attain it. To do this, let's assume $R_S = 0$ and that the idler load, R_i, is in absolute zero producing no noise. Under these conditions, the noise figure becomes

$$F = 1 + \frac{T_d}{T_0}\frac{R_V}{R_g} + \frac{T_d}{T_0}\frac{\omega_1}{\omega_2}(1 + \frac{R_V}{R_g})\frac{R_V}{R_i + R_V} \tag{2.44}$$

Assuming significant gain is required,

$$\frac{\gamma^2}{\omega_1\omega_2C^2R_{T1}R_{T2}} = \frac{\omega_1}{\omega_2}(\gamma Q)^2\frac{R_V}{R_i + R_g}\frac{R_V}{R_g + R_V} = 1 \tag{2.45}$$

where Q is the quality factor of the nonlinear capacitor. Substituting this expression into 2.44,

$$(F-1)\frac{T_0}{T_d} = \frac{(\frac{\omega_1}{\omega_2}\frac{R_V}{R_i+R_V}\gamma Q)^2 + 1}{\frac{\omega_1}{\omega_2}\frac{R_V}{R_i+R_V}(\gamma Q)^2 - 1} \tag{2.46}$$

By differentiating equation 2.46, the condition for optimum noise figure is obtained in

$$\frac{\omega_1}{\omega_2}\frac{R_C}{R_i + R_V} = \frac{1 + \sqrt{1 + (\gamma Q)^2}}{(\gamma Q)^2}. \tag{2.47}$$

Thus, the corresponding optimum noise figure is

$$F = 1 + 2\frac{T_0}{T_d}(\frac{1}{\gamma Q} + \frac{1}{(\gamma Q)^2}). \tag{2.48}$$

Equations 2.47 and 2.48 provide insight on how to choose the pump frequency to minimize noise, but it also demonstrates how crucial the characteristics of the nonlinear capacitor are. In

general, a nonlinear capacitor of high Q is desire to minimized the noise figure, however, the Q has an inverse relationship with the magnitude by which the capacitance changes. This is represented by the variables denoted as γ. As seen in equation 2.35, a γ is required to achieve a high negative resistance and attain high gain. Thus, there exists a trade-off between noise and high gain similar to conventional amplifiers.

CHAPTER 3

MODELING AND THEORY VERIFICATION VIA HARMONIC BALANCE SIMULATION

In chapter 2, a theory of how non-reciprocity can be achieved with asymmetric delay lines and parametric amplification was established. Simulations using fundamental components can serve as means of verifying theory. In this first section, Keysight's Advanced Design System (ADS) is used for simulating a simple version of the structure to affirm that a parametric amplifier can indeed function as the current source and when placed between asymmetrical delay lines leads to non-reciprocal propagation of EM waves.

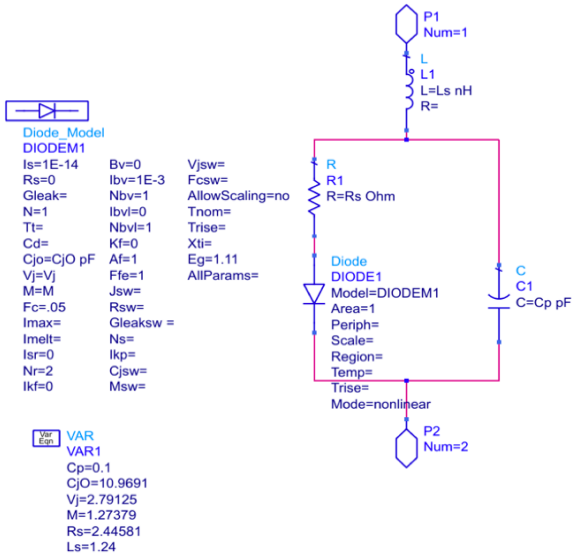

Figure 3.1: ADS model for a varactor using SPICE diode1 model. The model is based on the Infeneon BB857 varactor.

3.1 Varactor Modeling

First, a good model of the varactor is required. ADS has an extensive library of SPICE models for semiconductor devices including diodes. Manufacturers often have design kits for many of their devices or at least have the parameters for fundamental SPICE models. The latter is the case here. Figure 3.1 demonstrates the model as prescribed by Infeneon for their BB857 high Q varactor. (For fundamentals of varactors and semiconductor physics, refer to the first section in the appendices.)

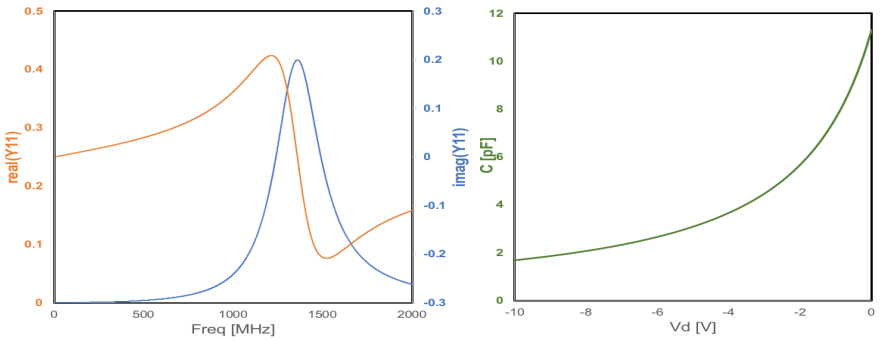

Figure 3.2: Y parameters and Capacitance-Voltage relationship of model Infeneon BB857 varactor.

Simulating the model in ADS yields the Y-parameters and the voltage dependent capacitance in 3.2. The quality factor of the varactor can be calculated to be 320 at 100MHz and at a reverse bias of -2 V. The self-resonant frequency (SRF) of the varactor occurs at 1,360MHz. This sets an upper limit on the pump frequency that can be used. Furthermore, at this point, it is convenient to define a term utilized to describe the degree of change in capacitance. Several conventions exist for this purpose, but to be consistent with how it was used in the derivation of gain and noise in chapter 2, the change in capacitance of the diode is defined as

$$M = \frac{C_{MAX} - C_{MIN}}{C_{MAX}}. \tag{3.1}$$

By this definition, according to derivation of gain, a $M = 1$ is highly desirable. For the varactor used here, $M = .82$. This high capacitance ratio along with the quality factor, makes this a great choice for parametric amplification design.

Considering the derivation of gain in chapter 2, with a non-linear capacitance with capacitance $C = C_0(1 + 2\gamma\cos(\omega_P))$ the general assumption $\gamma = \frac{M}{2}$ can be made.

3.2 Modeling of SAW Delay Lines

An important requisite for non-reciprocity in the structure discussed in chapter 2 is asymmetric delay lines with electrical lengths of 180° and 360°. In the electromagnetic domain, it is difficult to achieve these delays at RF due the large wavelength of light at these frequencies. Acoustic waves have a phase velocity up to 7 orders of magnitude slower than the speed of light. For this reason, acoustic devices are much more efficient in terms of form factor and thus will be used in the design and implementation of this structure since it can also incorporate signal processing functions such as filtering. To do this, an effective and accurate model compatible with circuit-aided design (CAD) software such as ADS is required for SAW transducers. In general, many models based on equivalent circuit elements have been proposed and validated to aid engineers in designing filters, correlators, and delay lines in CAD environments [42, 43, 44]. Here, the model demonstrated in [45] will be used due to its accuracy and its ability to model uni-directional transducers (UIDT) [46].

Most equivalent circuit models of SAW transducers can be split and thus described by the function they are intending to simulate. Figure 3.3 a) demonstrates the top view of a bi-directional SAW interdigitated transducer (IDT). The metallization (black) is patterned on the piezoelectric structure according to the frequency response that is desired. For the case in figure 3.3 a), the center frequency is written as

$$f_C = \frac{v_{SAW}}{\lambda}. \tag{3.2}$$

Figure 3.3 b) demonstrates the equivalent circuit utilized to model the performance of the IDT based on the work presented in [45]. The model first considers the capacitance and resistance due to metallization. A transformer is used to convert the signal from the electrical domain to the acoustic domain shown in red. The efficiency of this conversion is linearly proportional to the

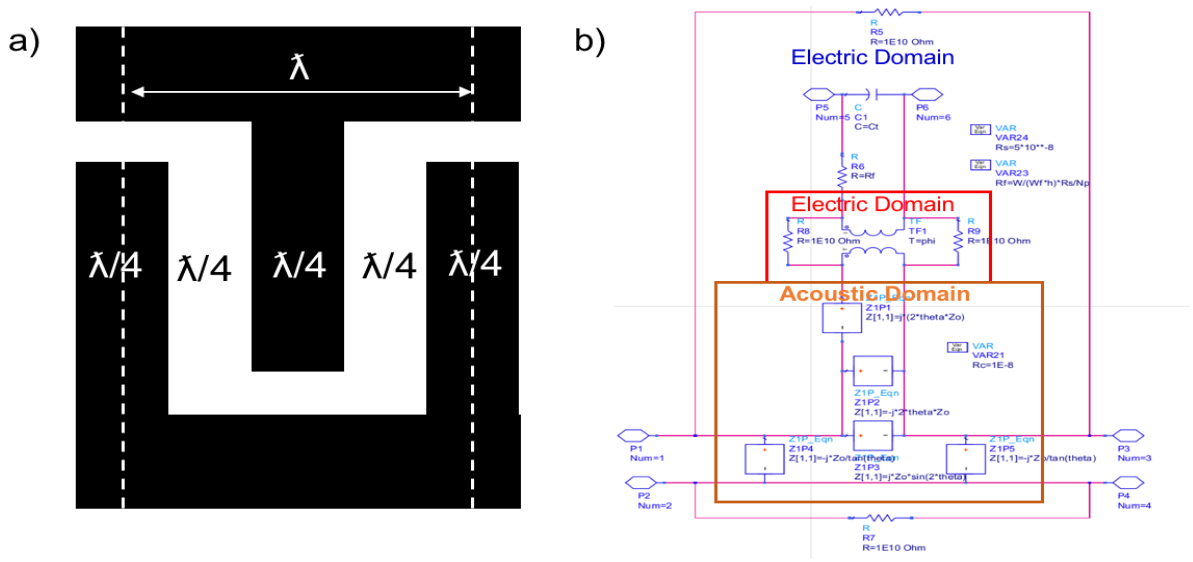

Figure 3.3: a) Topology for SAW bi-directional transducers. b)Equivalent circuit model based on the coupling modes as described in [45].

electromechanical coupling constant k^2. The model parameters are

$$Z_0 = \frac{1}{q\beta}$$

$$\phi = \eta N L$$

$$C_T = N C_S$$

where N is the number of transducer pairs, $\eta = \sqrt{2.268\omega_0 C_S}\frac{k^2}{\lambda}$, $C_S = \epsilon_p W$, W is the aperture of the transducer, and $\theta = \frac{\beta N L}{2}$. The quantities p and q are

$$p = \frac{\beta_1 - \delta - \kappa_{11}}{\kappa_{12}}$$

$$q = \frac{1}{\delta + \kappa_{11} + \kappa_{12}}$$

where $\delta = k - k_0$, $k = \frac{\omega}{v_{SAW}}$, and $k_0 = \frac{2\pi}{\lambda}$. For $LiNbO_3$, as recommended by [45], $\kappa_{11} = .02k_0$ and $\kappa_{12} = .0062k_0$.

The rest of the circuit can be described, in the bi-directional IDT case, as a power splitter

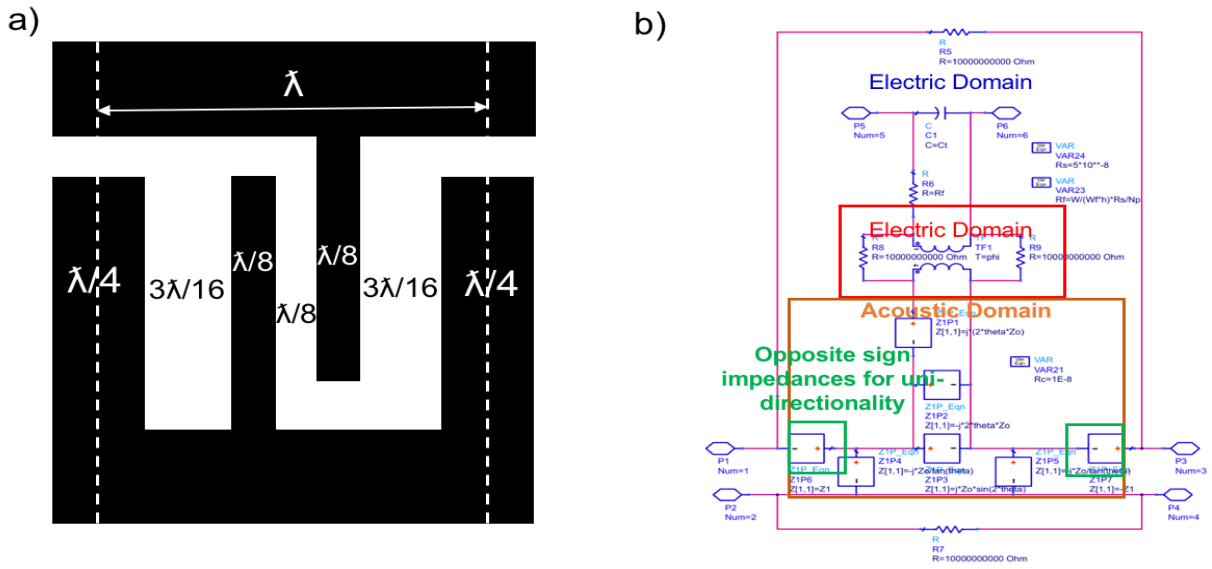

Figure 3.4: a) Topology for SAW uni-directional transducers. b)Equivalent circuit model of uni-directional IDT based on the coupling modes as described in [46].

and transmission line model. This signifies that a bi-directional IDT has a minimal loss of -3 dB since the power is split and acoustically actuated in two directions. For the purposes of minimizing acoustic loss due to bi-directionality, designers will often choose to use uni-directional transducers. These transducers achieve directionality by separating the centers of transduction and reflection [31, 30, 32]. Figure 3.4 a) and b) illustrates the topology utilized in this work to implement uni-directionality and the equivalent circuit model. The model is identical to the bi-directional transducer except with the addition of opposite sign impedances on either side of the acoustic transmission line. As described in [46], the introduction of opposite sign impedances results in the uni-directionality consistent with experiments.

To verify the model and the model parameters, a delay line with bi-directional transducers was fabricated in $LiNbO_3$ and compared to simulations. The delay line was designed with 24 pairs of transducers of $4\mu m$ finger widths, yielding a wavelength of $16\mu m$. Figure 3.5 a) and b) demonstrates the fabricated delay line and a comparison of the measured vs model of forward wave S-parameter, S_{21}. The phase velocity of the piezoelectric is $3776\frac{m}{s}$ resulting in a center frequency of 236MHz. Since both IDTs are bi-directional, the insertion loss is -6.9 dB. Theoretically, the

minimum insertion loss of a delay line with two bi-directional transducer delay line is -6 dB. As seen in figure 3.5 b), the model agrees very well with the measured data of the delay line, thus verifying the accuracy of the equivalent circuit.

A thing to note are the resistances that wrap the ports surrounding the entire model as depicted in Figure 3.3 a) and 3.4 a). These resistances are set to $10^{10}\Omega$ and function as a DC path for harmonic balance convergence.

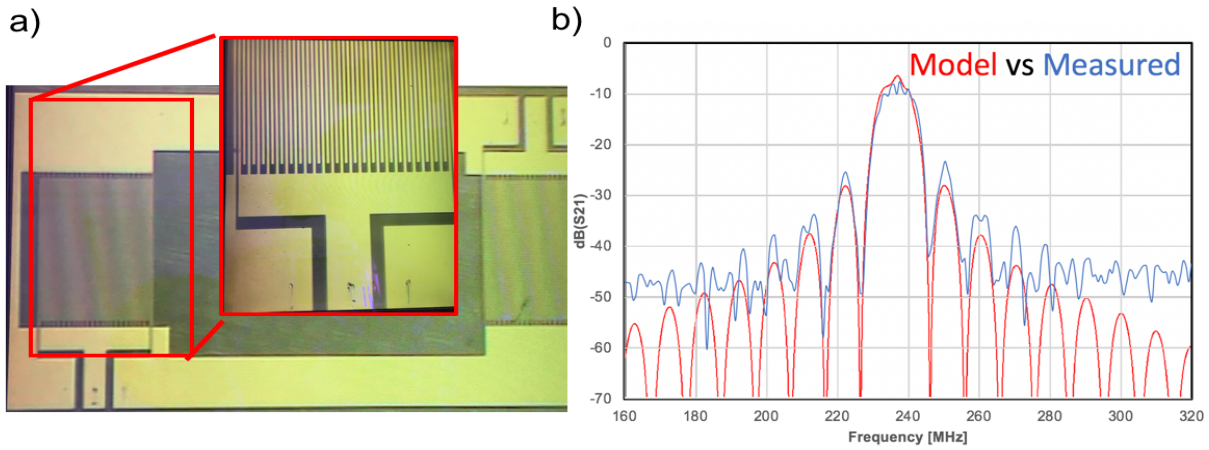

Figure 3.5: a) Micrograph of $LiNbO_3$ SAW delay line at 236MHz. b) Model vs. Measured of $LiNbO_3$ SAW delay line at 236MHz

3.3 Harmonic Balance Simulation with Ideal Transmission Lines

With the proper varactor model in place, verification of the theory with harmonic balance (HB) simulations in ADS can take place. Figure 3.6 shows the schematic test benches used in this purpose including the harmonic balance set up. As recommended by ADS technicians, when simulating systems where many orders of mixing and intermodulation products can exist, it is necessary to utilize as many harmonics as possible for accurate results. It was seen during simulation that the results did not change using an order past 8 harmonics. For this reason, an order of 10 was chosen. Since it is desired for the signal frequency to be swept while fixing the pump frequency in some

cases, the HB simulation is done a as a two-tone simulation.

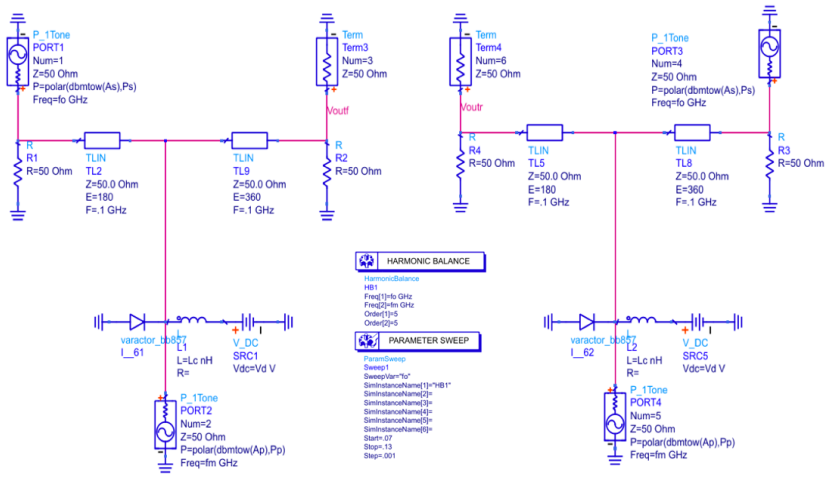

Figure 3.6: Circuit topologies used to simulate forward and reverse transmission of EM waves on asymmetric topology in ADS environment using a two-tone harmonic balance simulator.

The varactor is biased via the DC voltage supply labeled Vd with a series inductance L_c to resonate out the average capacitance of the varactor. The transmission lines have electrical lengths of $180°$ and $360°$ to implement the asymmetry required by theory for non-reciprocity.

Another important thing to note is that in order to simulate both the forward and reverse gain, the circuit needs to be simulated twice where the sources are reversed. This is simply done by replicating the circuit on the same bench with opposite port excitation as seen in figure 3.6.

Figure 3.7 demonstrates the results of the simulation at a center frequency of 100MHz where the signal and pump signals both have a phase of $0°$. Figure 3.7 a) and b) shows the forward and reverse transmitted power and phase when the pump power is 0 dBm. Figure 3.7b) and c) demonstrate how non-reciprocity arises when the pump power is 16 dBm. As the pump power is increased in Figure 3.7 d) and e), the non-reciprocity in magnitude becomes weak while there is a $180°$ phase difference between forward and reverse transmitted waves. These results closely resemble the theoretical calculations made in chapter 2 and illustrated in figures 2.2 and 2.4 thus verifying that non-reciprocity can indeed occur with parametric amplification and proper asymmetry designed in the connected structure.

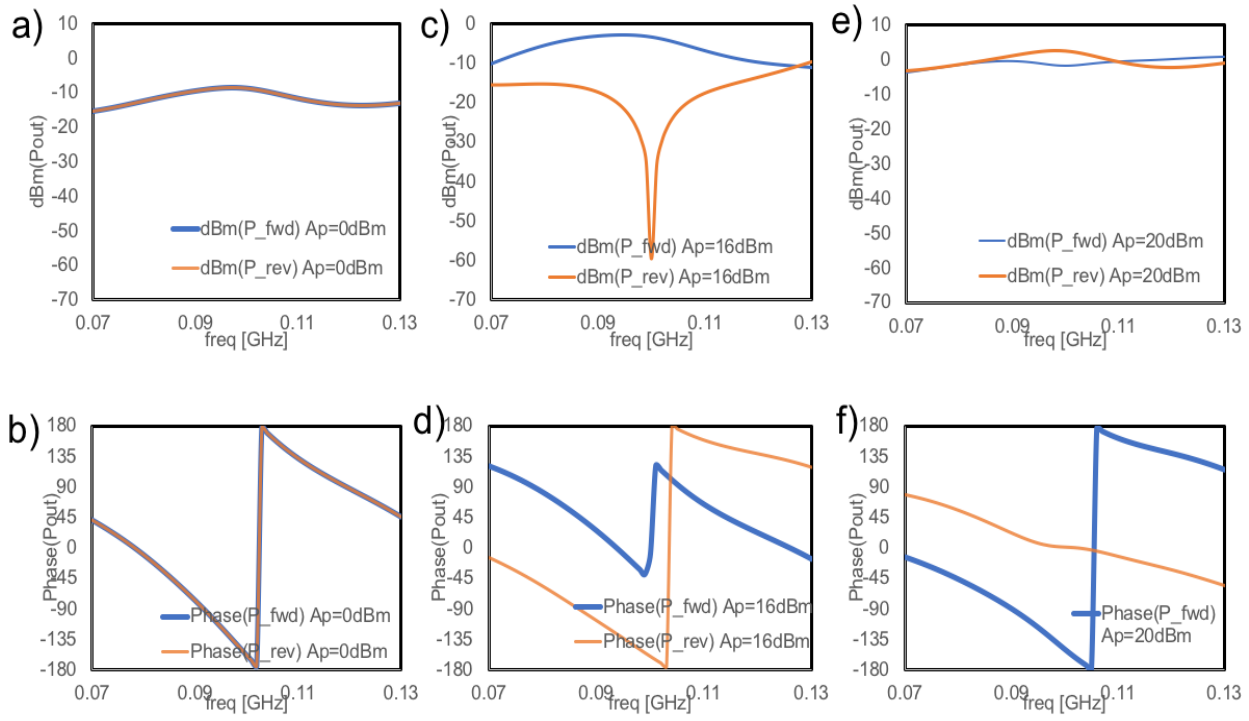

Figure 3.7: a) Magnitude of forward and reverse transmission with a pump power of 0 dBm. b) Phase of forward and reverse transmission with a pump power of 0 dBm. d) Magnitude of forward and reverse transmission with a pump power of 16 dBm. d) Phase of forward and reverse transmission with a pump power of 16 dBm. e) Magnitude of forward and reverse transmission with a pump power of 20 dBm. f) Phase of forward and reverse transmission with a pump power of 20 dBm.

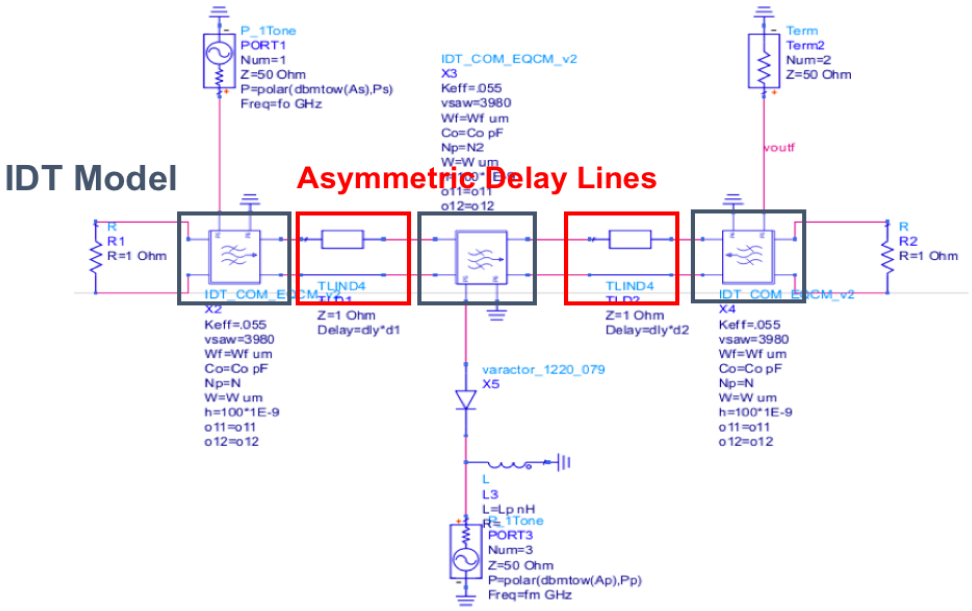

Figure 3.8: ADS harmonic balance simulation set up of non-reciprocal network based on asymmetric SAW delay lines.

3.4 Harmonic Balance Simulation with SAW delay lines

Figure 3.8 demonstrates the ADS circuit schematic of the non-reciprocal network utilizing the bi-directional transducer model previously covered. The model parameters are set to attain the same frequency response as the experimental device in figure 3.5. Each IDT has 24 pairs of transducer fingers and an aperture of $500\mu m$. The delay lengths between transducers are implemented via transmission lines whose characteristic impedance is set to the acoustic impedance Z_0 and time delay to $L\frac{\lambda}{2v_{SAW}}$ and $L\frac{\lambda}{v_{SAW}}$ where L here is 5. The center transducer is used to couple the pump circuit to the asymmetric delay lines. The shunt inductance of L_P resonates the time average capacitance of the varactor at the pump frequency. The input power in the simulation is -40 dBm. As in the previous example, a copy of the circuit is simulated in parallel with the source and terminations swapped to obtain the reverse transmission.

Figures 3.9a)-c) show the harmonic balance simulation results at a pump frequency of $2\omega_{IN}$. Figure 3.9a) is the case where the pump power is 0 dBm. As seen here, both the forward and reverse

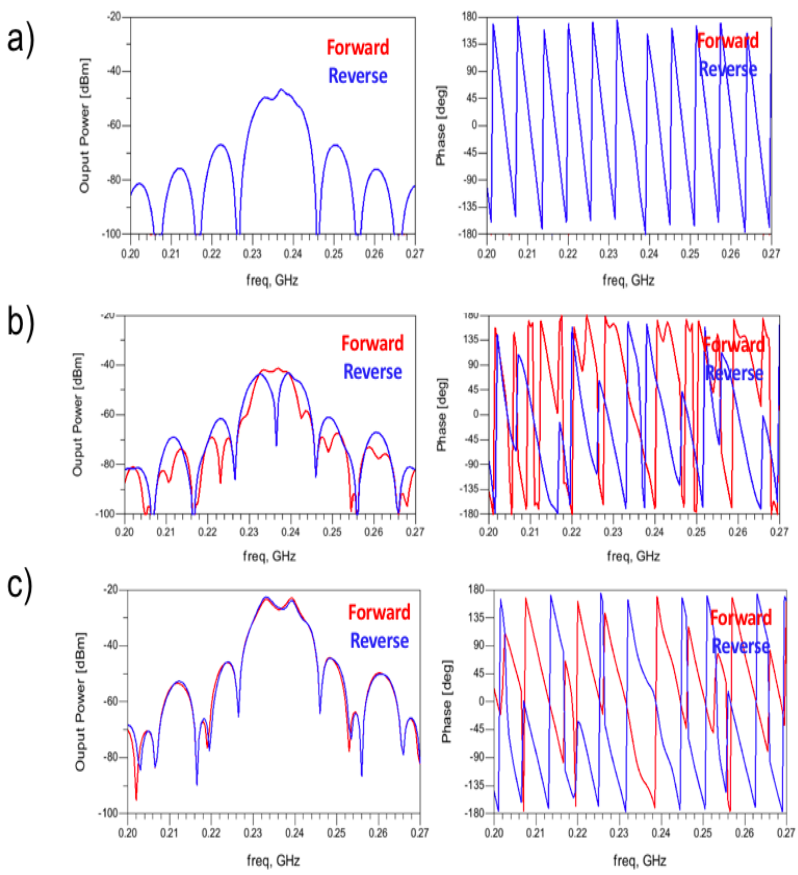

Figure 3.9: a) Magnitude and phase of forward and reverse transmission at a pump power of 0 dBm. b) Magnitude and phase of forward and reverse transmission at a pump power of 10 dBm. c) Magnitude and phase of forward and reverse transmission at a pump power of 15 dBm

transmitted power are the same and thus reciprocal. However, when the pump power is increased to 15 dBm, non-reciprocal transmission is observed (figure 3.9b)). If the power is increased to 20 dBm (Figure 3.9c)), the same behavior is observed as before where the magnitudes are equal with about +20 dB of gain, however there is a non-reciprocal phase shift of 180° between forward and reverse waves. This again agrees very well with the behavior predicted by the theoretical derivation and the simulation with ideal transmission lines signifying that the SAW device is an effective method of implementing the required asymmetry to obtain non-reciprocity.

CHAPTER 4

DESIGN AND PERFORMANCE OF NON-RECIPROCAL ACOUSTIC DEVICES BASED ON DEGENERATE PARAMETRIC INTERACTIONS

With all of the modeling and simulation tools now in place, the structure can now be designed. In this chapter, two versions will be covered: phase coherent non-reciprocal topology, and a phase incoherent topology. While most of the performance discussion will focus on the later, it is useful to review both generations.

4.1 Design, Fabrication, and Performance of SAW Devices

The first SAW device utilizes uni-directional transducers for input and output ports and a bi-directional center transducer. The gaps between transducers are $\frac{11\lambda}{2}$ and 5λ. The IDTs and UIDTs have the same finger scheme as shown in figures 3.3 and 3.4 where the wavelength is $20\mu m$. The input and output UIDTs have 18 pairs of transducers while the center bi-directional transducer has 24. Since the minimum feature size of the UIDT is $\frac{\lambda}{8}$, the frequency of operation was chosen to accommodate conventional lithographic processes. The piezoelectric substrate used in this work is 128° Y-cut $LiNbO_3$. The phase velocity of the substrate is $3800\frac{m}{s}$ which should result in a center frequency of 190 MHz. The aperture of the IDTs was chosen to be $500\mu m$ to obtain a good match to 50Ω. The second SAW device utilizes a UIDT for the center transducer as well. In this case all three transducer have 24 pairs of fingers, a $500\mu m$ aperture width, of All of the UIDTs have a directivity of 5 dB.

Figure 4.1 illustrates the fabrication used to create the SAW devices. After the substrate is cleaned with acetone and isopropyl alcohol rinses and dried, a layer of LOR 3A resist is spun at 3000 rpm for 1 minute to a thickness of about 300 nm. It is then baked in a hotplate at $160^\circ C$ for 3 minutes. A photosensitive of S1805 is then spun at 5000 rpm for 45 seconds to a thickness of 500nm then baked at $105^\circ C$ for 2 minutes. The spinning and baking process take place in the hood

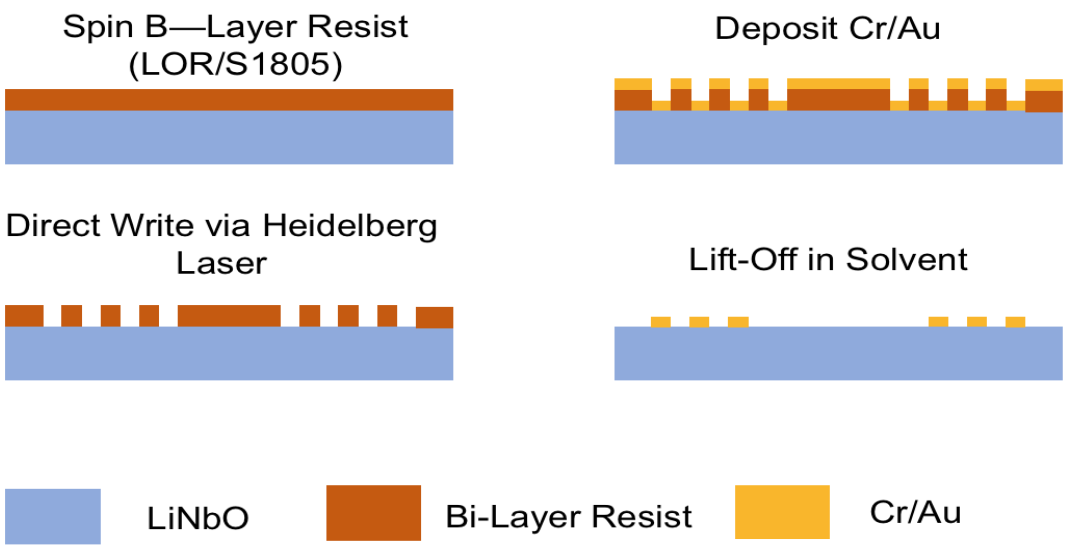

Figure 4.1: Fabrication process developed to create SAW devices.

depicted figure 4.2, which is equipped with programmable spinners and hot plates.

The samples are then exposed via a Heidelberg laser writer model dwl66 at a power of 70mW with an intensity of 30% and a filter setting of 25%. Figure 4.3 depicts the laser writer utilized in this process.

The samples then dipped in a TMAH bath for development for 45 seconds. After development, the 5 nm layer of chrome is deposited via E-beam evaporation as an adhesive layer. Immediately following this, 100nm of gold is deposited. It is worthy to note that most SAW designs utilize aluminum for IDTs due to low density, however, for the purposes of creating robust IDTs for gold wire-bonding, gold was used instead. Additionally, the loading effects of Au should not greatly increase the acoustic losses at 190 MHz. Both designs have identical gaps between transducers.

Figure 4.4 demonstrates the finalized SAW structures. Device 1 in figure 4.4 a) utilizes a bi-directional center IDT while the device in figure 4.4 b) utilizes an identical UIDT for the center transducer. The measured results are plotted in figure 4.5 a) and b). The insertion loss of the input and output transducers of device 1 is -16 dBm with a bandwidth of 12 MHz. The center transducer has equal insertion loss to either input or output transducers of -10 dB. The matching of the input and output transducers could be improved with a matching circuit. Figure 4.5 b) demonstrates

Figure 4.2: Hood equipped with spinners and hot plates for baking resist.

the frequency pertinent S-parameters of device 2. The insertion loss between input and output transducers is improved to -10 dB with a bandwidth of 10 MHz. The center transducer has an insertion loss of -7.2 dB to the output transducer and an insertion loss of -12 dB signifying the transducer has a directivity of 4.8 dB. The matching of the transducers is slightly improved for device 2 by the increase in transducer capacitance.

4.2 Design and Performance of Non-Reciprocal SAW Device Based on Phase-Coherent Degenerate Parametric Amplification

With the SAW devices in place, the pump circuit can now be designed. For this first iteration, a single tuned device will be used to obtain an experimental verification. As mentioned in chapter 2, the varactor of choice for this work is Infeneons's BB857 whose Q is 320 and has a $\gamma = 0.82$.

The first step in the design flow is to resonate the transducer capacitance at the center frequency. Figure 4.6 demonstrates the capacitance and S_11 of the transducer. Electrically, the transducer can be simply thought as a load capacitance. With a series inductance L_P between the transducer and varactor, the inductance can be determined by

$$L_P = \frac{1}{\omega_S^2(C_T + C_V)}. \tag{4.1}$$

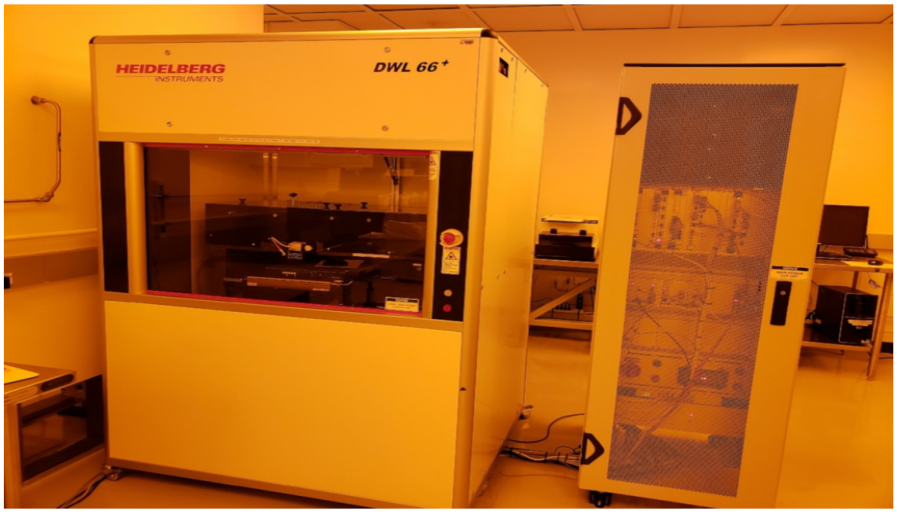

Figure 4.3: Heidelberg DWL66 laser writer with a 405nm laser. This is utilized to write the pattern on the resist.

where ω_S is the frequency of operation, C_T is the transducer capacitance, and C_V is the average capacitance of the varactor. At 190 MHz, the transducer capacitance is 12pF and the varactor capacitance of the varactor is estimated to be 8pF, thus equation 4.1 yields an inductance of 35nH.

Next step is to match the signal generator to the varactor. However, as stipulated by Manley-Rowe, the pump and signal frequencies need to be isolated so the matching network for the varactor needs to accomplish this as well. The matching circuit was designed by finding the input impedance at the pump frequency of the varactor loaded by the inductor, L_P and the transducer. A 2nd order high pass circuit was then designed to match to this impedance as seen in figure 4.7.

The resulting pump circuit is illustrated in figure 4.8a. The inductors are implemented via Coilcraft 0402DS series inductances of the values shown. The capacitors used are AVX 0402 ACCU-P series capacitors. An important thing to note is that this high pass design is a low Q design by choice to optimize the pump frequencies. The completed board is shown in figure 4.8b.

With the pump circuit design in place, a simulation of the performance can made. Figure 4.9a shows the ADS harmonic balance test bench used to simulate the circuit. As described before, the harmonic balance set-up is a two-tone simulation where the signal and pump frequencies maintain the relationship for the degenerate case, $\omega_P = 2\omega_S$. An identical circuit is run simultaneously

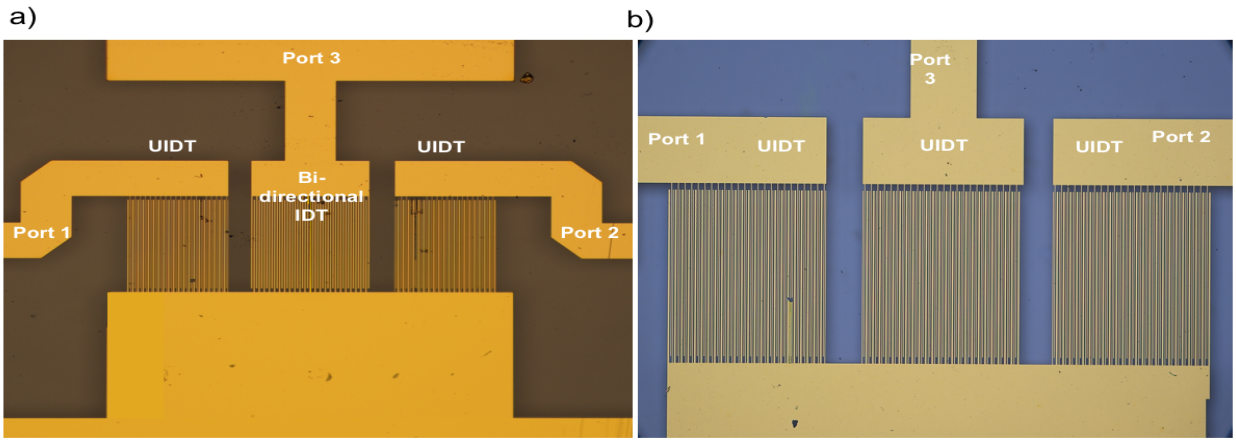

Figure 4.4: Micrograph of Gold IDT structures for a) with bi-directional center transducer and b) an identical UIDT center transducer

where the termination and source are swapped to simulate the reverse propagation. It was observed that 20 dBm was required to achieve the non-reciprocal propagation in figure 4.9b. The input power is -20 dBm in the simulation.

The simulation results demonstrate an improvement in insertion loss of -10 dB considering the loss of the SAW structure is -15 dB. An isolation of 15 dB exist between forward and reverse transmitted power. The non-reciprocal action is band-limited by the single tuned network used to resonate out the center transducer capacitance.

4.2.1 Measurements and Performance with Bi-Directional Center Transducer: Device 1

Figure 4.10a demonstrates the measurement set-up for the phase-coherent case. Beginning with the phase coherent case, as described in the analysis in chapter 2, the negative resistance is maximized when the phases of both the pump and signal frequencies are synchronized as $\theta = \phi = 0$. Given the available equipment, the only possible way to measure this case is by utilizing a spectrum analyzer and two signal generators whose phases are synchronized via the 10 MHz reference as shown in figure 4.10a. The spectrum analyzer is a Keysight model 9320B. The signal frequency to be amplified is generated via the Keysight 9310A signal generator. The pump signal is generated

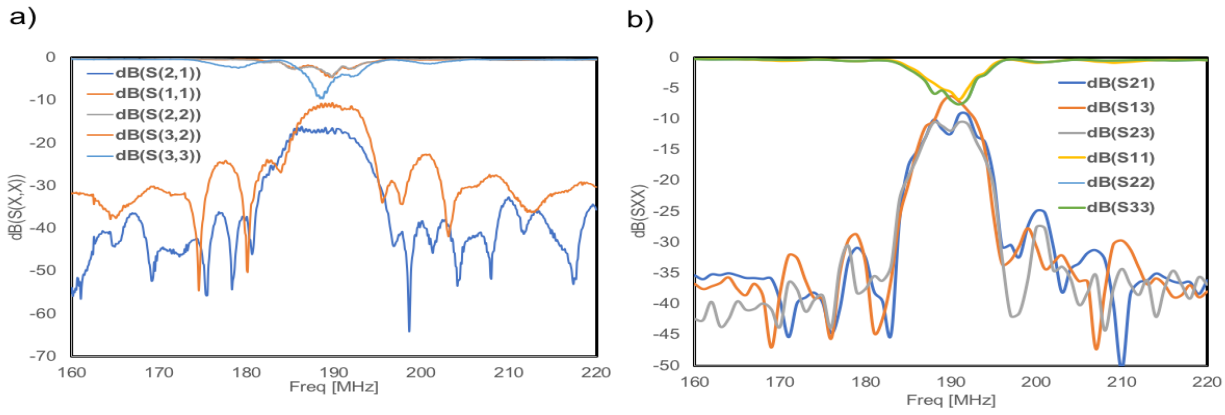

Figure 4.5: a) S-parameters of SAW Device 1 b) S-Parameters of SAW Device 2

with an Agilent E8257D. This signal generator possesses a phase adjustment feature that makes this approach possible.

The measurement is performed as follows. The signals are set to $\omega_P = 2\omega_S$ and are swept in 1 MHz steps maintaining the phase-coherent degenerate relation. An oscilloscope was used to ensure the two signals were in phase before the measurement was taken. The process was repeated to obtain the results for the reverse case by simply swapping the signal generator and spectrum analyzer connections.

Figure 4.13 a) and b) demonstrates the results for the phase-coherent degenerate case where the input signal power is -20 dBm and the pump power is 23.3 dBm. The case for when the pump signal generator is off is plotted for reference. When the pump is on, gain is observed in the forward direction with an improvement of 12 dB at 186 MHz. In the reverse direction, the signal in attenuated by 6 dB at 186 MHz attaining an isolation of 18 dB. The bandwidth of non-reciprocity, however, only occurs for 5 MHz which is nearly half of the bandwidth of the filter. This is likely limited by the singly-tuned network used to resonate out the transducer capacitance. Furthermore, as seen in figure 4.5 a), the bi-directional center transducer has a narrower band than the input and output UIDTs.

An additional measurement was done with the set-up illustrated in 4.10b where a Keysight

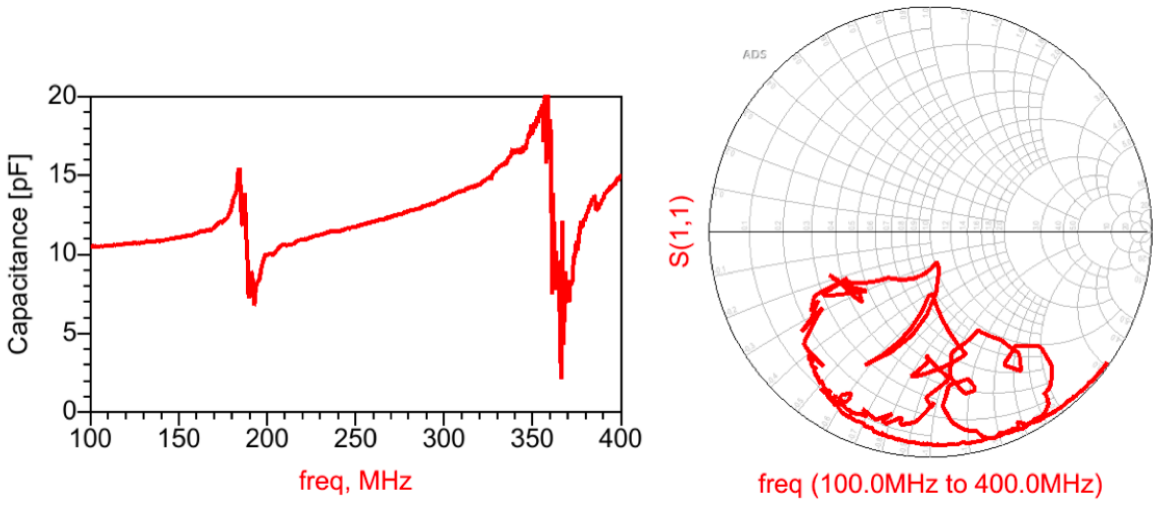

Figure 4.6: Measured Capacitance of bi-directional IDT center transducer. Smith chart plot of S11 of center IDT

E5063A vector network analyzer (VNA) was utilized to measure the S-parameters to investigate if the device is capable of operating in a phase-incoherent manner. Figure 4.13 demonstrates the case where $\omega_P = 368MHz$ at a pump power of 21 dBm. As seen here, phase-incoherent operation is possible, however, it is very weak. The forward gain of 3dB is observed with only an isolation of 5.2 dB. This measurement was done with aid of a mechanical tuner at the pump circuit to improve matching and maximize the bandwidth of non-reciprocity. To probe further, new center transducer and pump circuit designs are required.

4.2.2 Measurements and Performance with Uni-Directional Center Transducer: Device 2

For this second generation, an identical UIDT designed was used for the center transducer with the same offset relative to the input and output. As seen in figure 4.5 b), the center transducer has a directivity of 4.8 dB to the output transducer. As result of a duplicate design, the bandwidth of 7 MHz the UIDTs match around the center frequency. To investigate any benefits this design has over the other, considering the transducer capacitance changes very little, the phase-coherent

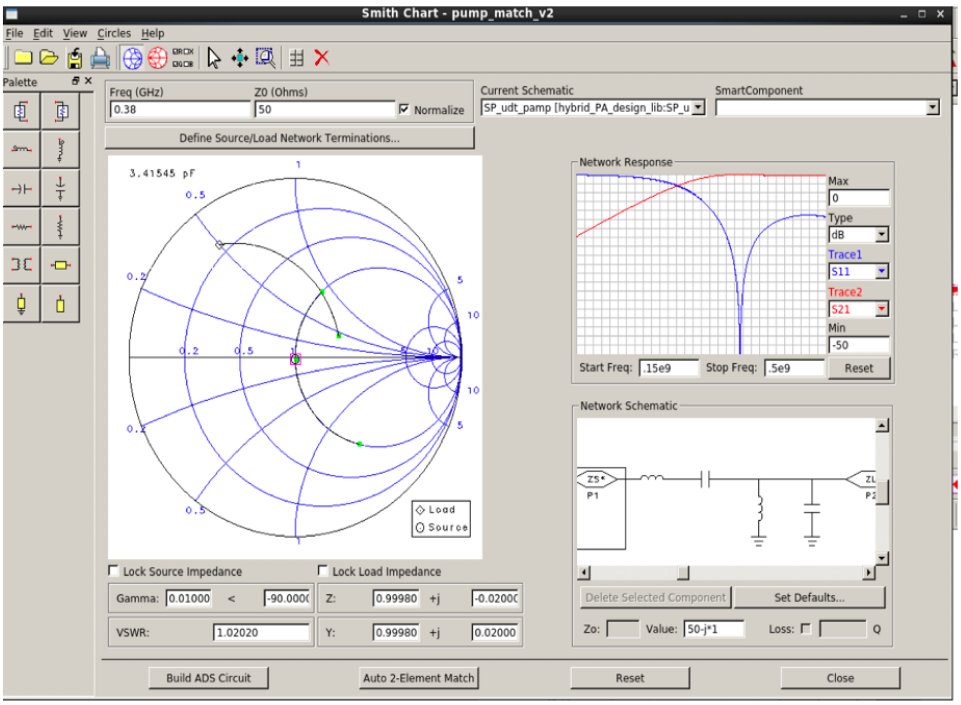

Figure 4.7: Design of pump circuit with ADS smith chart tool. A 2nd order high pass circuit was topology was used to obtain isolation between pump and signal frequencies.

measurements were repeated on device 2 utilizing the same pump circuit.

Figure 4.13a) and b) show the forward and reverse transmission of the phase-coherent case and resulting forward and reverse gain when the pump and input signal phases follow $\theta = \phi = 0°$. It is quickly obvious that the maximum gain has increased to 17.5 dB. The isolation is improved up to 24 dB. If the phase relationship between the input and pump is changed to $\theta - \phi = 180°$, the reverse transmission exhibits gain, while in forward transmission, the signal experiences attenuation as seen in figure 4.13 c) and d). This verifies another aspect of theory in chapter two, where the pump phase can be used to change the forward and reverse responses. The maximum reverse gain when $\theta - \phi = 180°$ is 3.3 dB lower than the forward gain when $\theta - \phi = 0°$. This is due to the directionality of center transducer. Although the bandwidth of non-reciprocity was improved to 8 MHz, the full bandwidth is still limited by the pump circuit.

To rectify this, the same design process described earlier was used to design a second-order resonant circuit on the transducer side of the pump circuit. The varactor was changed to Skyworks

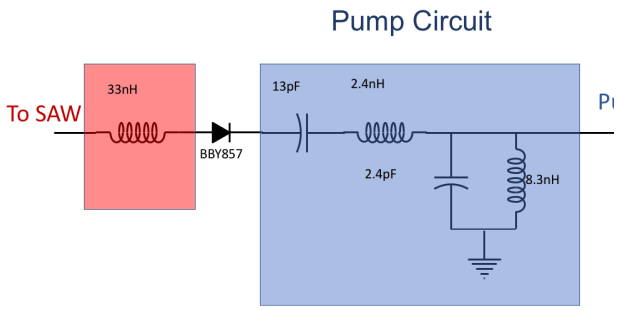

(a) Designed Pump Circuit.

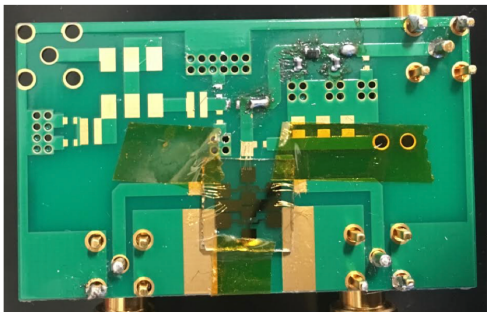

(b) Completed board with SAW device 1 bonded via 2mil Au bond-wires.

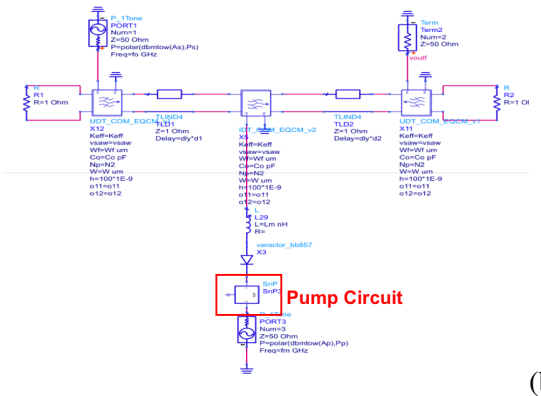

(a) Schematic used in HB for simulation of non-reciprocity.

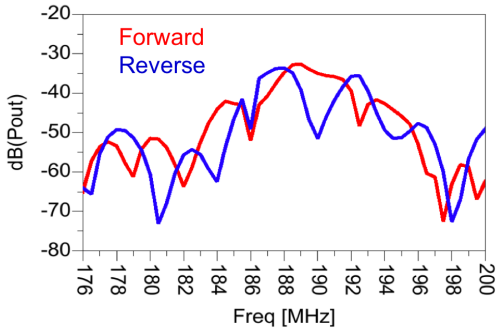

(b) Harmonic Balance simulation results with a pump frequency of $\omega_P = 2\omega_S$ and the Pump power is 20 dBm

SMV1248 which as a $C_{MAX} = 22.2pF$, a $C_{MIN} = 1.3pF$, a $\gamma = .942$, and a Q=80.

Figure 4.14 illustrates the new pump circuit, where the new circuit is shown in red. The shunt inductor and capacitor of values 48nH and 20pF are chosen to resonate at the lower end of the bandwidth at approximately 162 MHz, while the series inductor is chosen to resonate out the transducer capacitance along with the varactor average capacitance. Furthermore, this new topology allows the ability to bias the varactor and utilize the average capacitance as a tuning element. For this purpose, a bias tee is added between the pump match and the pump circuit. Additionally, a modular design is adapted for the implementation to avoid exposing the SAW to high soldering temperatures. Figure 4.15 demonstrates the completed boards connected in the proper order. This modular design also grants the ability to compare how the pump and match circuits compare. Fig-

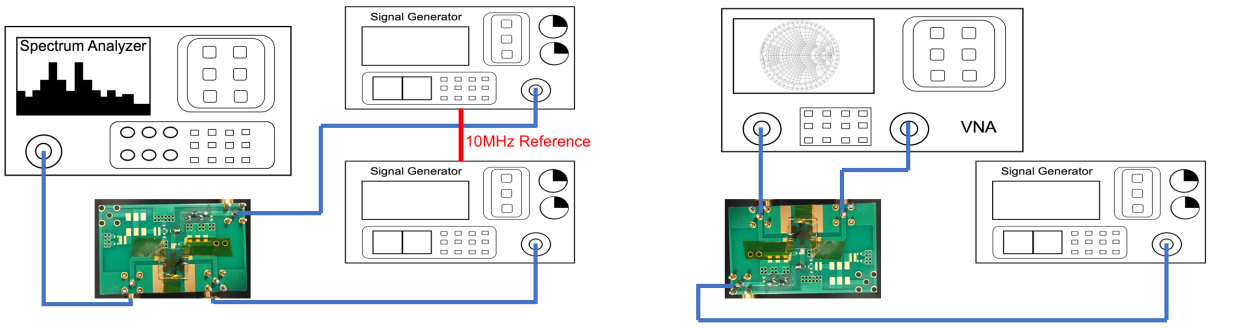

(a) Measurement set-up for phase-coherent degenerate case $\omega_P = 2\omega_S$.

(b) Measurement set-up for phase-incoherent degenerate case $\omega_P \neq 2\omega_S$.

ure 4.16a) and b) demonstrate the measured S-parameters of the single resonant pump circuit (a) and 2nd order pump circuit (b). As seen here, the first design, while attaining a large bandwidth, fails to properly isolate the pump and signal frequencies. The 2nd order pump circuit matches the filter over the required bandwidth even though being a narrower band design, yet it also provides a significant improvement in isolation between the pump and signal frequencies. The pump match circuit, as mentioned before, is able to support a wide selection of pump frequencies.

The ADS harmonic balance simulation results for the phase-coherent degenerate case with this new pump circuit design is shown in figure 4.18. The input power is -20 dBm, the pump power is 12 dBm and the varactor is biased at -1.9V and $\theta = \phi = 0°$. From these results, non-reciprocity occurs over the entire bandwidth signifying the 2nd-order resonant circuit is functioning as desired. A gain of 15.1 dB is observed at 192 MHz with an isolation of 17.2 dB between forward and reverse transmission.

The measurement results of the phase-coherent case are shown in figure 4.18a)-d). For the $\theta = \phi = 0°$ case, a gain of 12 dB is observed with a total isolation of 24.5 dB. For $\theta = \phi = 180°$, the max gain is 9.8 dB due to the directivity of the center transducer. The maximum isolation also suffers due to directionality decreasing to a value to 16 dB. Both cases show a large improvement in bandwidth which now show non-reciprocal behavior throughout the entire usable bandwidth. This is likely due to insufficient isolation between the pump and signal frequencies in the previous pump circuit design. The required pump power decreased to 13 dBm signifying the matching to

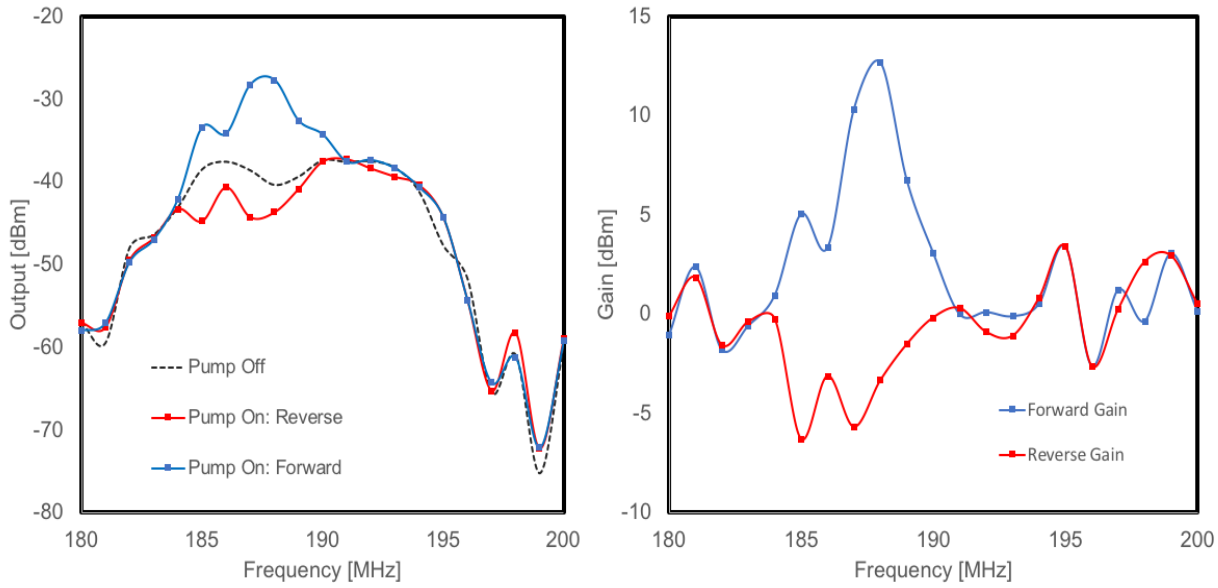

Figure 4.11: a) Measured output power of forward and reverse transmission for $\omega_P = 2\omega_S$. Pump power is 23.3 dBm. b) Forward and reverse gain for $\omega_P = 2\omega_S$ at a pump power is 23.3 dBm. The input signal power is -20 dBm.

the signal generator has improved. The measurement for $\theta = \phi = 0°$ was again repeated with two mechanical phase shifters in the pump signal to obtain a $90°$ phase shift. Figure 4.19 shows the measured response from the spectrum analyzer. This further verifies the theory in chapter two and demonstrates this structure can be used aa a tunable non-reciprocal filter.

4.3 Phase-Incoherent Operation of Non-Reciprocal SAW Filter Based on Degenerate Parametric Amplification

The non-reciprocal behavior theorized in chapter 2 and experimentally verified in this chapter requires that the parametric amplifier function as a current source. It does this only under the phase-coherent degenerate condition $\omega_P = 2\omega_S$ where the signal and idler frequencies are equal, $\omega_S = \omega_i$. Since both of these occupy the same frequency, they can either interfere constructively or destructively dependent on the phase relationship between both signals. As derived in equation

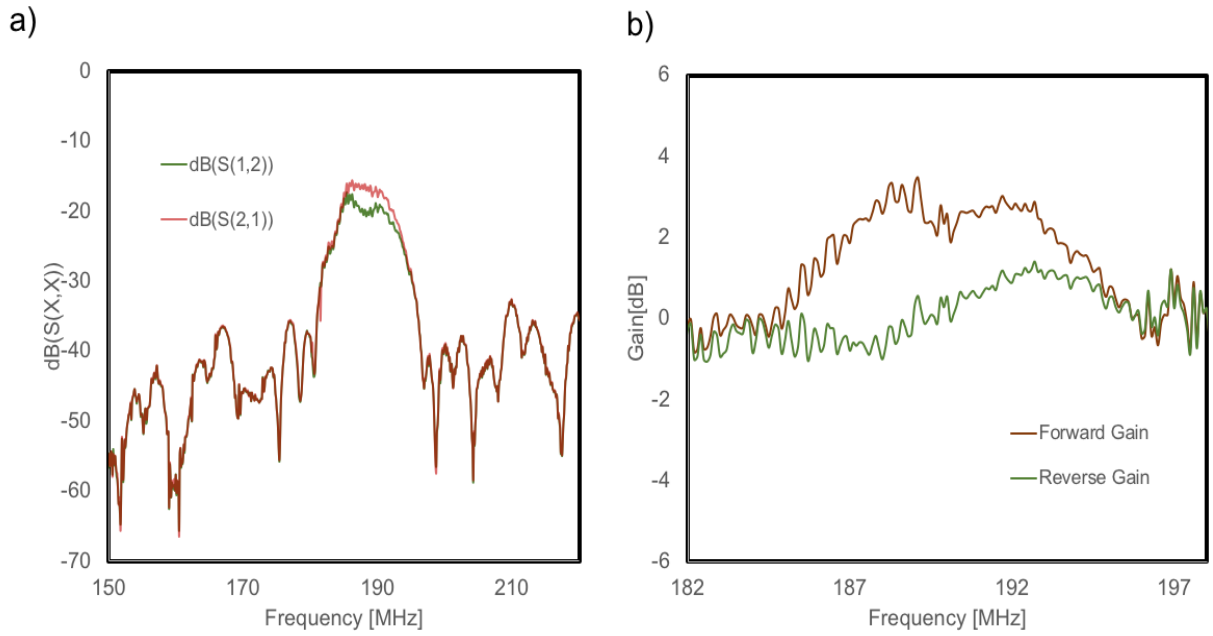

Figure 4.12: a) Measured output power of forward and reverse transmission for $\omega_P = 368MHz$. Pump power is 21 dBm. b) Forward and reverse gain for $\omega_P = 368MHz$ at a pump power is 21 dBm

2.28, the phase is dependent on the phase relationship between the pump and input signal, which grants the structure discussed here the ability to change the frequency response according to the pump phase. However, this comes at the price of requiring knowledge of what the phase of the input signal is, thus the name phase-coherent degenerate amplifier. While surely an interesting structure for phase-coherent systems, it is generally desirable in communications for devices to function properly when this is not possible. Here, we will discuss how this structure can operate in a phase-incoherent architecture.

The idler signal is a mixing product as a result of the nonlinear capacitance being pumped by a large signal. We have discussed the phase-coherent degenerate case in some detail, however, the instances where $\omega_P \neq 2\omega_S$ and $\omega_S \neq \omega_i$ commonly referred to as the non-degenerate case has only been covered briefly. The case in which $\omega_P \neq 2\omega_S$ and $\omega_S \neq \omega_i$, but the idler and signal frequencies can inhabit the same resonant structure is considered degenerate phase-incoherent.

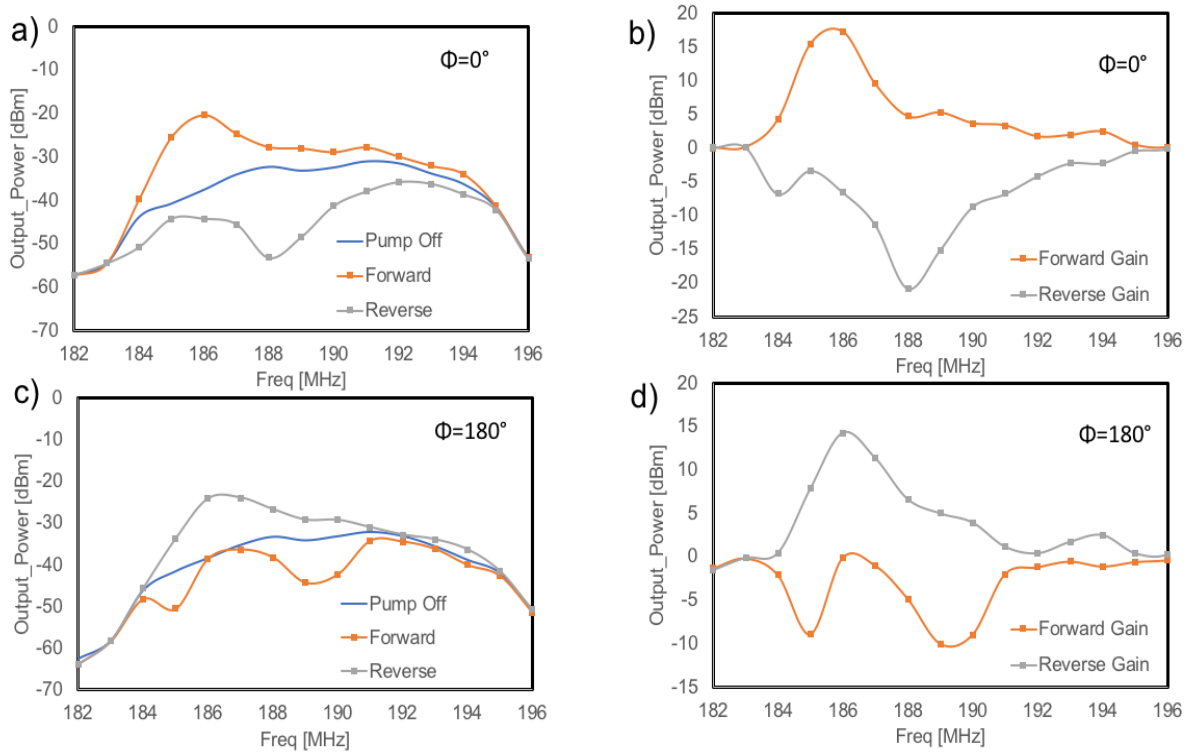

Figure 4.13: a) Measured output power of forward and reverse transmission for $\omega_P = 2\omega_S$, Pump power of 15 dBm, and $\theta = \phi = 0$. b) Forward and reverse gain for conditions in a). c) for $\omega_P = 2\omega_S$, Pump power of 15 dBm, and $\theta = \phi = 180$. d) Forward and reverse gain for conditions in c)

The difference can be explained in figure 4.20a) and b). The measurement is made with the same spectrum analyzer set-up as previously described. Figure 4.20 a) demonstrates the phase-coherent case where $\omega_S = 2\omega_P$. When the pump is off, a single tone, the input signal at ω_S, is clearly visible at 190 MHz. When the pump is on and the phases are aligned, the pump signal appears at 380 MHz and causes amplification of input signal to take place. Figure 4.20 b) demonstrates the phase-incoherent case where the pump signal no longer satisfies the condition $\omega_S = 2\omega_P$. Here, the idler appears at $\omega_P - \omega_S$. Since the pump frequency in this example is 366 MHz, the idler tone appears at 176 MHz. As seen, in this case, the structure is still capable of gain at the expense of pump power. Since the idler can inhabit the bandwidth of the SAW structure, this is still considered as a degenerate. In a non-degenerate amplifier, the idler is generally chosen so that $\omega_i \gg \omega_S$ typically requiring its own resonant tank to support and isolate it from the rest of the signal frequencies.

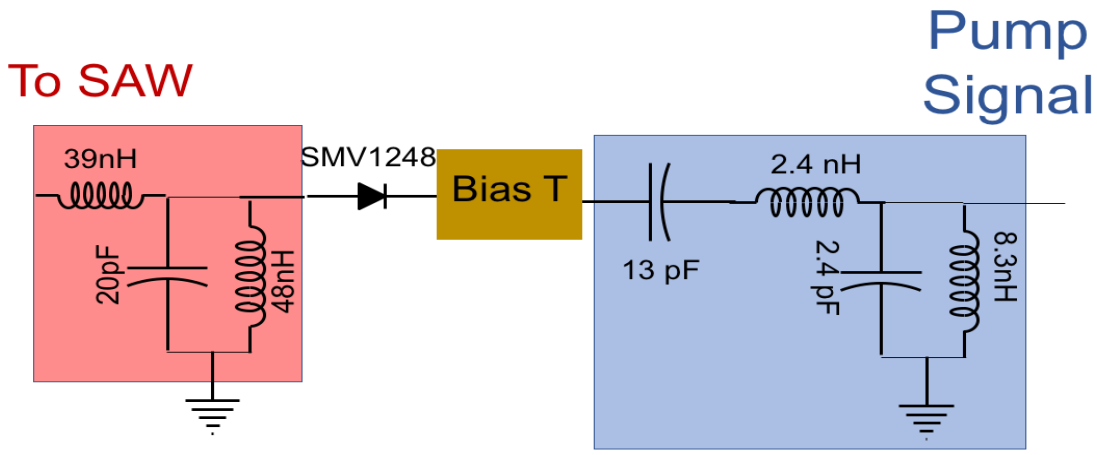

Figure 4.14: Pump circuit designed with 2nd order resonant topology for the transducer.

Unlike the phase-coherent degenerate case, the two other cases are unaffected by pump phase and the input signal frequencies. While this is a desired characteristic for amplification, it causes the structure discussed in this work to lose its non-reciprocal behavior. However, as shown in section 2.2, the structure is capable of operating in a phase-incoherent mode where the asymmetry in delay lines causes there to be a non-reciprocal phase shift of 180° between forward and reverse waves. This was seen experimentally in figure 4.13 with the aid of a tune at the pump circuit. However, as predicted by theory, this is at the cost of pump power and is very weak. In order to increase the degree of non-reciprocal propagation, another form of asymmetry must be introduced into the circuit. This is another area where SAW transducers can provide some aid.

An additional asymmetry can be introduced in the structure by a UIDT. UIDTs function by introducing reflections within the structure to separate the reflection and transduction centers. As the acoustic wave is actuated within the gratings, the waves traveling in the direction of directionality will interfere in phase as in the case in a bi-directional transducer. The waves traveling in the opposite direction of the directionality will reflect, change directions, and interfere constructively. Figure 4.21a) demonstrates the typical orientation of a UIDT based SAW delay to minimize insertion loss. Most of the wave is transmitted to the direction of directionality, while if the receiving

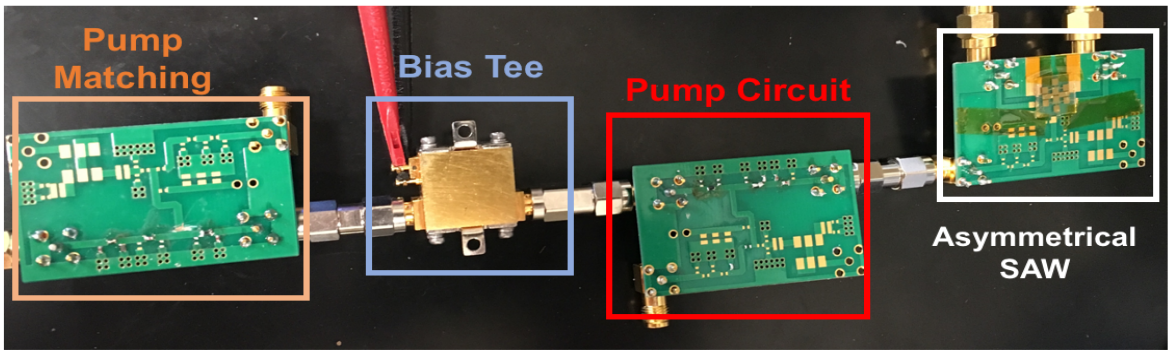

Figure 4.15: Picture of modular design depicting separate boards for SAW design, pump circuit, and pump matching network.

transducer's directionality is opposite that of the source transducer, most of the SAW will be absorbed. The opposite is also true as seen in 4.21 b). If the receiving transducer is oriented in the same direction as the source UIDT, most of the wave passes through the transducer. This behavior is observed experimentally in device 2 in figure 4.5 b) where all three transducers are UIDTs. The center transducer to the output transducer insertion loss of -7.2 dB, while the insertion loss at the center frequency from center UIDT to the input UIDT is 12 dB. The loss between the input and output transducers is 10 dB signifying that most of the signal is being passed through the center transducer, while little of it is absorbed. This can be leveraged to attain the additional asymmetry desired. Specifically, the unequal absorption of SAWs traveling from different directions.

Figure 4.22a) and b) demonstrates how a structure with a UIDT center transducer connected to a parametric amplifier can provide the additional asymmetry. For the forward case, the SAW actuated by the input transducer goes through the center transducer due to the and is absorbed by the output UIDT. The SAW that was absorbed by the center transducer experiences the parametric conversion and amplifications. Most of the amplified signal then gets actuated to the output transducer where it constructively interferes. In the reverse case, since the now the center transducer

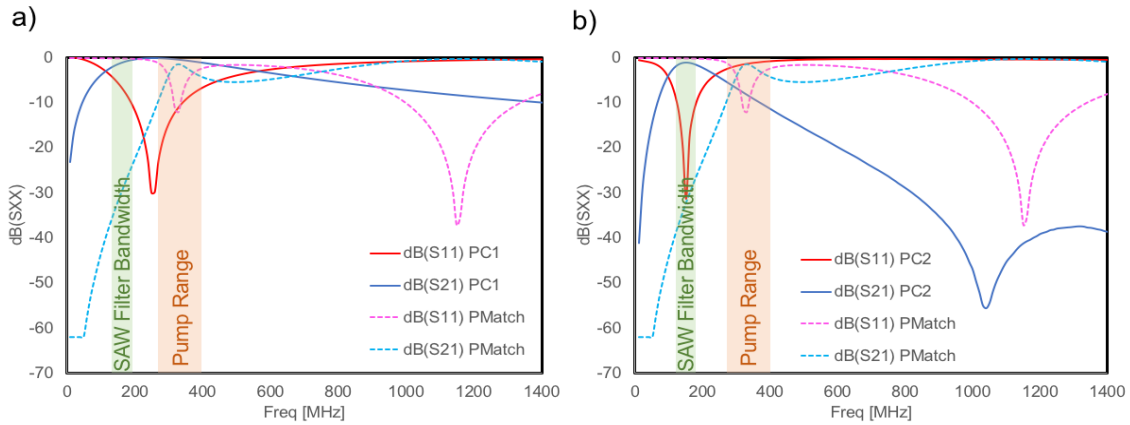

Figure 4.16: a) S-parameters of single resonant pump circuit compared to pump match circuit. b) S-parameters of 2nd order pump circuit compared to pump match circuit.

is oriented opposite to the input transducer, most of the SAW gets absorbed, amplified, and gets reflected back to the input. This action can result in instability and oscillation. This is discussed further in upcoming sections.

A simulation of the structure (device2) can be made in ADS where this time, $\omega_P \neq 2\omega_S$ and ω_S is swept while the ω_P is kept constant. Figure 4.23 demonstrates the simulation results where $\omega_P = 366MHz$ and ω_S is swept from 160 MHz to 220 MHz. the pump power is 15 dBm and the varactor is biased at -0.8V. As seen here, the structure exhibits an insertion loss for the forward transmission of -3.52 dB, signifying a gain of 7 dB. The isolation between forward and reverse waves is 45 dB at the center frequency. This result demonstrates that a very strong non-reciprocity is possible.

To verify this experimentally, the S-parameters of device 2 with the 2nd-order pump circuit is measured via network analyzer in the set-up demonstrated 4.10b. The measurements were performed for pump frequencies where strong non-reciprocity was observed, namely 365 MHz, 366 MHz, and 375 MHz. Each condition is measured across different varactor biases and pump power to optimize operating conditions.

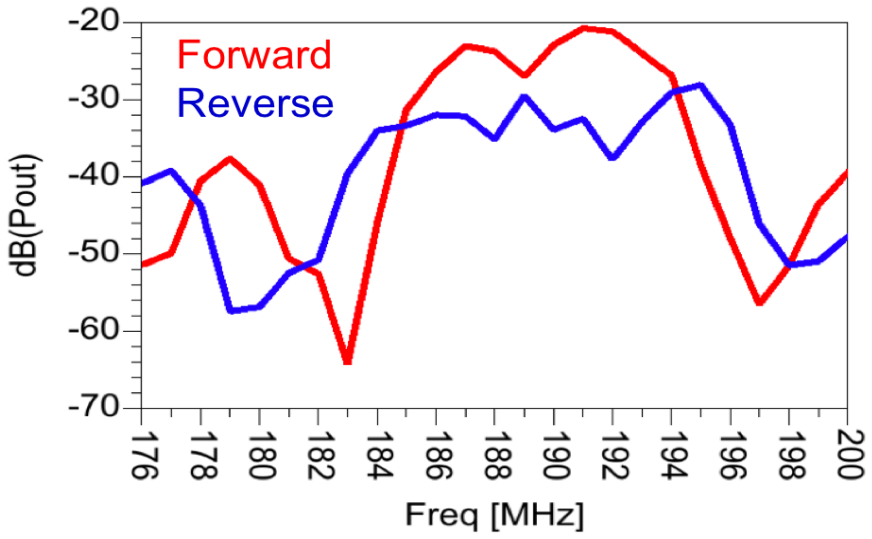

Figure 4.17: ADS harmonic balance simulation results of phase-coherent degenerate case $\omega_P = 2\omega_S$. Pump power=11 dBm, and $\theta = \phi = 0°$. Varactor biased at $V_B = -1.1V$

Figure 4.24 a)-d) show the case where $\omega_P = 365MHz$ at a pump power of 19 dBm across different varactor biases. One characteristic that is observed throughout is that the strength of non-reciprocity in increases with varactor bias. The more positive the varactor bias, the more non-linear it behaves. The optimum point is seen at -1.8V, where the insertion loss is -5.2 dB and isolation is 35 dB. At a bias of -1.7V, the device becomes unstable, causing the performance to degrade. A similar behavior is seen if the varactor is fixed and the pump power is changed as in figure 4.25 a)-d). As power in increased, so does the degree of non-reciprocity until it reaches severe instability at a power of 21 dBm. A similar behavior is observed for the cases when $\omega_P = 366MHz$ in figures 4.26a)-d) and 4.27a)-d). Under these conditions, the minimum insertion loss is -6.4dB and the isolation is 27dB. Again, instability occurs at a pump power 19 dBm when the varactor is biased at -1.7V and at 21 dBm when the varactor is biased at -1.9V.

A significant change is observed when the pump frequency is 375 MHz in figures 4.28 a)-d) and 4.29 a)-d). For pump frequencies 366 MHz and 365 MHz, the idler frequency, given by $\omega_i = \omega_P - \omega_S$, is only partially supported by the SAW filter. This limits the bandwidth of the parametric amplification but also causes the need for increase pump power for operation. However,

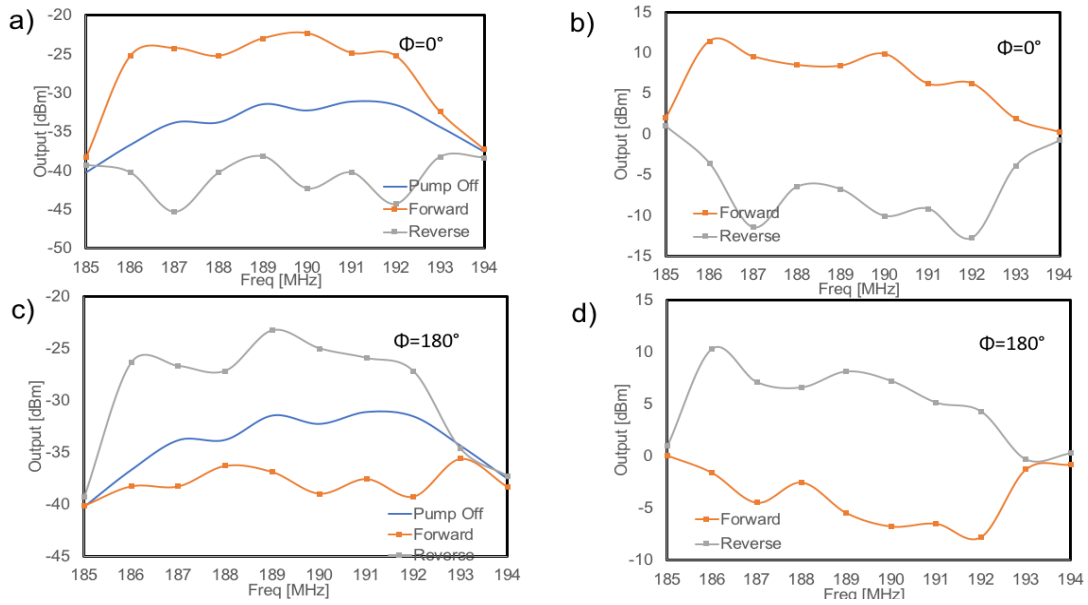

Figure 4.18: a) Forward and reverse transmission for the $\theta = \phi = 0°$ case. b) Forward and reverse gain of the $\theta = \phi = 0°$ case. c) Forward and reverse transmission for the $\theta = \phi = 180°$ case. d) Forward and reverse gain of $\theta = \phi = 180°$. All measurements have the following additional conditions: $\omega_P = 2\omega_S$, pump power=13 dBm, and varactor biased at $V_B = -1.9V$

when $f_P = 375MHz$, the idler exists for the entire bandwidth of the filter. This reduces the required power for non-reciprocity down to 11 dBm. Furthermore, more gain is available in this condition. Unlike in the previous conditions, changing the varactor biasing in figure 4.28 a)-d) doesn't have the same effect as increasing the power. It changes the shape of the non-reciprocity, while increasing the pump power (figure 4.29 a)-d)), increases the gain. When the power is 13 dBm the insertion loss decreases to -1.2 dB as seen in figure 4.29 c). A gain of +0.21 dB when the pump power is 14 dBm (figure 4.29 d) is possible, however, the device becomes unstable at this point. Another issue that arises from using pump conditions that allow the idler to exist under the same bandwidth as the signal, is the appearance of tones at the areas where the idler might resonate strongly as seen in all the measurement of this condition. This can also lead to instability and in general is an undesired artifact of this operating condition.

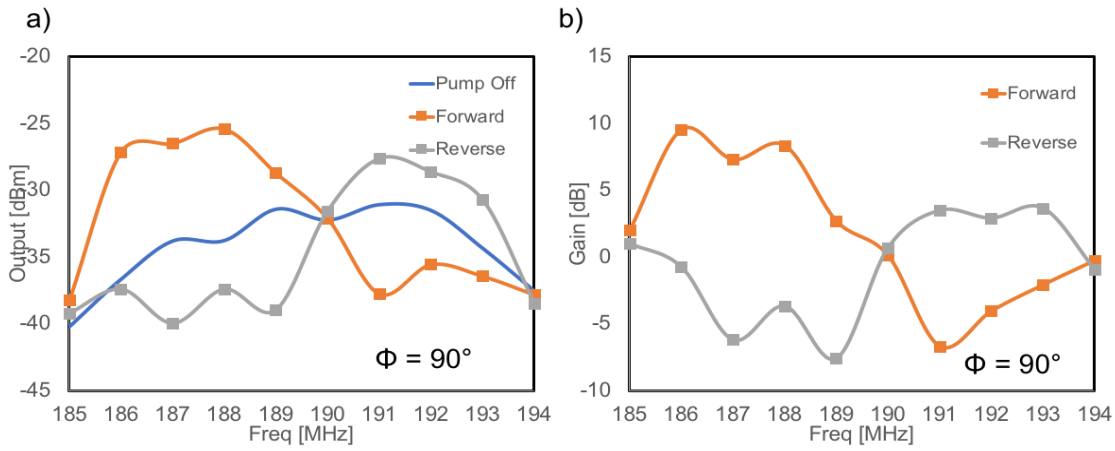

Figure 4.19: a) Forward and reverse transmission for $\theta = \phi = 90°$ case. b) Forward and reverse gain of $\theta = \phi = 00°$ case.

4.3.1 Non-Degenerate Non-Reciprocal Operation

All of the measurements phase-incoherent measurements up to now, have been of the degenerate case in one form or another. This is due to the idler sharing some of the bandwidth with the signal frequency. Another possibility is to operate the device in a non-degenerate condition where $\omega_i \gg \omega_S$ so that the idler frequency no longer shares the same bandwidth with the signal frequency. The drawback of this case is that a separate resonant tank, is required to support the idler frequency. Although such a network hasn't been designed, it is possible to use the higher order resonances due to the parasitic elements of the current board implementation. Figure 4.30 shows a measurement of just this case. The pump frequency was swept under the same set-up with the network analyzer until non-reciprocal operation was observed. The pump frequency of $f_P = 950MHz$ was seen to cause a small amount of non-reciprocal behavior demonstrating an improvement in insertions loss of -0.5 dB and an isolation of 2 dB.

At this condition, the idler frequency will lie between 795 MHz to 805 MHz. Well beyond the bandwidth of interest. This provides verification that non-degenerate operation of the structure is possible. This merits further investigation as non-degenerate amplifiers have not only a stability

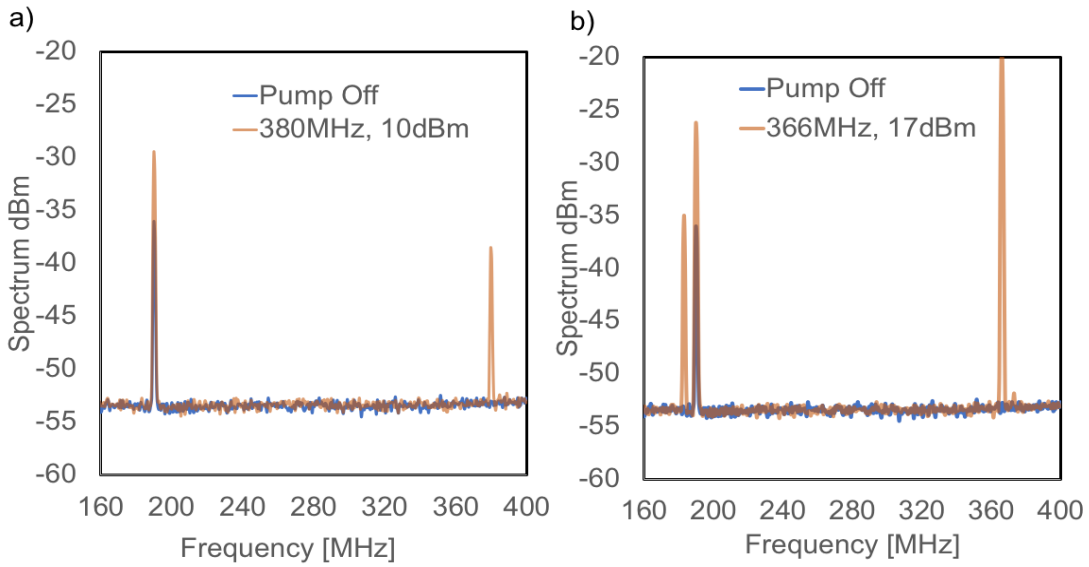

Figure 4.20: a) Phase-coherent degenerate parametric amplification case where $\omega_S = 2\omega_P$. b) Phase-incoherent degenerate parametric amplification $\omega_P \neq 2\omega_S$ and $\omega_S \neq \omega_i$

advantage for this structure but also a noise advantage as will be seen in upcoming sections.

4.3.2 Large Signal Performance

Like conventional amplifiers, there is a limitation as to how much power can be delivered by a reflection amplifier although the limiting properties are quite different. To better understand this, lets revisit the transducer gain in equation 2.39. This small signal representation can be turned into a large signal model described in [40, 47]. The large signal transducer gain can be written as

$$g_t = \frac{4G_{g1}G_L}{G_{T1} - \frac{G_0}{(1+\alpha P_S)^2}} \tag{4.2}$$

where P_S is the input power at ω_S, G_{g1} is the conductance of the source generator at ω_S, G_L is the load conductance, R_{T1} is the total conductance at ω_S, G_0 is the negative resistance given by

$$G_0 = \frac{\omega_S \omega_i K^2 R_{GP} P_P}{G_{Ti} G_{TP}^2}. \tag{4.3}$$

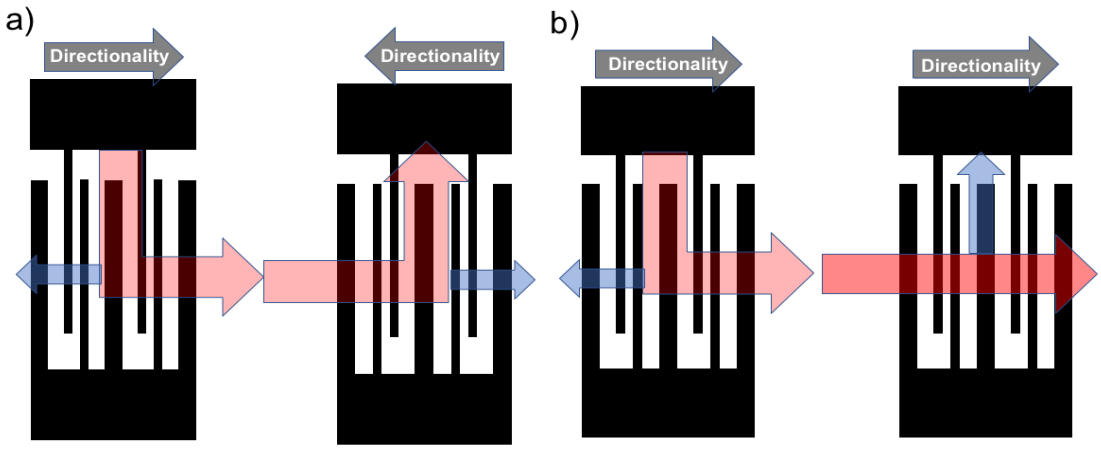

Figure 4.21: a) Typical orientation of UIDTs for minimum insertion loss. b) Atypical orientation of UIDTs where most of SAW wave is not absorbed by the transducer

The term α is given by

$$\alpha = \frac{\omega_i \omega_P K^2}{4 G_{Ti} G_{TP} G_L}. \tag{4.4}$$

K quantifies the non-linearity of the varactor and is given by $K = \frac{\partial C(v)}{\partial v}$. P_P is the pump power and G_{T2} and G_{TP} are the total loading at the idler frequency ω_i and pump frequency ω_P respectively.

From equation 4.2, the saturated power can be derived by setting $\alpha P_S = 1$. At this point, the gain has decreased by 3 dB from its small signal value. Using this condition, the saturated power can be written as

$$P_{SAT} = \frac{4 G_{Ti} G_{TP} G_L}{\omega_i \omega_P}. \tag{4.5}$$

From equation 4.6, it can be surmised that to increase the saturated power, the non-linearity of the varactor should be decreased by further reverse biasing for example or the heavily loading the structure. An increase in saturated power results in an increase of required pump power as well

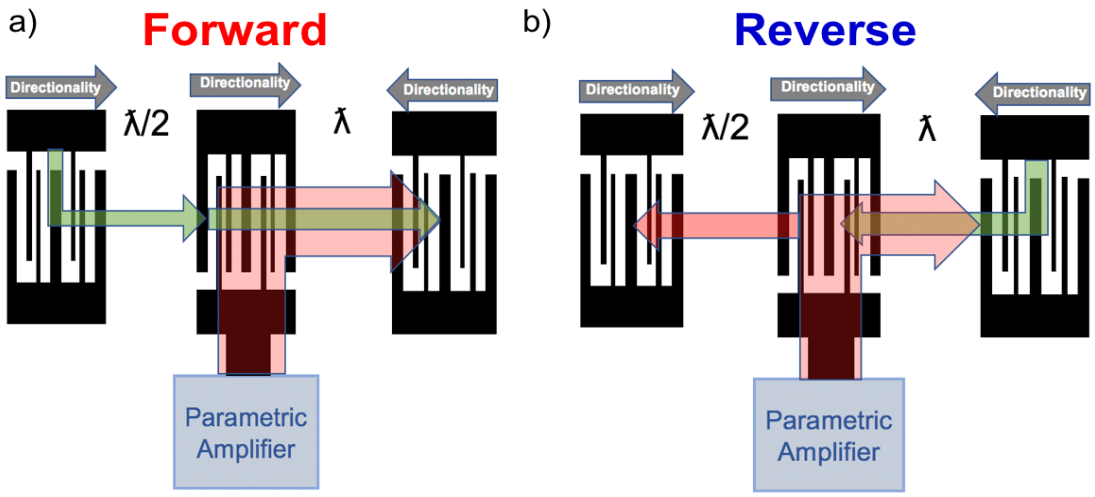

Figure 4.22: a) Forward transmission. b) Reverse transmission

as an increase in noise figure. This can be further examined by setting the input power $P_S = 0$ in equation 4.2. Solving for the pump power and then taking the ratio of P_{SAT} and pump yields

$$\frac{P_{SAT}}{P_P} = \frac{4\omega_S G_{GP} G_L}{\omega_P G_{T1} G_{T3}}. \tag{4.6}$$

As seen here, the pump power can be used to increase the saturated power. It also verifies that a higher pump frequency decreases saturated power.

Figure 4.31 shows the AM to AM distortion measurements of the non-reciprocal SAW parametric amplifier of two operating conditions previously discussed at a signal frequency of 189 MHz. The behavior described by theory is evident in the two cases demonstrated. For $P_P = 12dBm$, $\omega_P = 375MHz$, and $V_B = -1.6V$, the saturated power is -17.1 dBm. For $P_P = 18dBm$, $\omega_P = 366MHz$, and $V_B = -1.9V$, the saturated power is improved to -11.6 dBm. This improvement comes from a combination of factors. First, the varactor is biased in a further reverse condition effectively decreasing K. Secondly, as discussed in the previous section, the idler circuit is only partially supported by the SAW filter. For a signal frequency of 189 MHz and a pump frequency of 366 MHz, the idler appears at 177 MHz, which is outside the bandwidth of the filter.

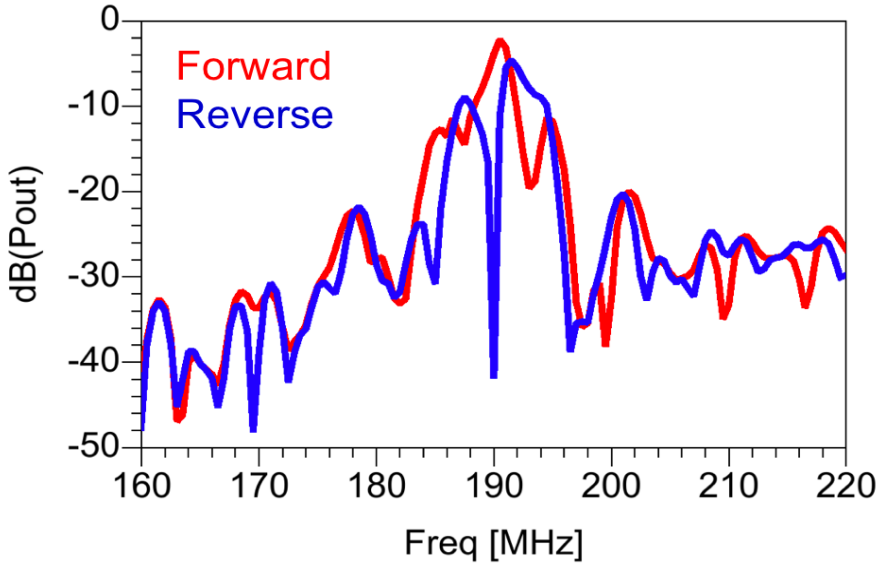

Figure 4.23: ADS two-tone harmonic balance simulation of forward and reverse transmission where $\omega_P = 366MHz$ and ω_S is swept from 160 MHz to 220 MHz. The pump power is 15 dBm and the varactor is biased at- 0.8V.

Thus R_{T2} is significantly increased in equation 4.6. Additionally, the pump power is increased to 18 dBm, while not obvious from 4.6, impacts overall linear gain. This is due to the fact that in order for linear operation of a parametric amplifier, generally $P_P \gg P_S$. This can be understood intuitively in that the negative resistance is an artifact of pumping nonlinear reactance with a large pump signal. Depending on the magnitude of the pump signal, the input signal can eventually interfere with this action if increased to a high enough level.

4.3.3 Noise Performance

In section 2.3.4, the noise figure of negative resistance amplifiers was derived. It is important to note that the noise of a degenerate parametric amplifier has two noise figures much like mixers since the device operates under frequency conversion principles. These are namely single-sideband noise figure (F_{SSB}) and double-sideband noise figure (F_{DSB}). The distinction exists because mixers can generate lower and upper sideband mixing products who both contribute to noise. Figure 4.32 demonstrates the appearance of the signal in a band-limited parametric amplifier with a pumping frequency exactly twice the center frequency of the filter. If the signal in the upper side-band

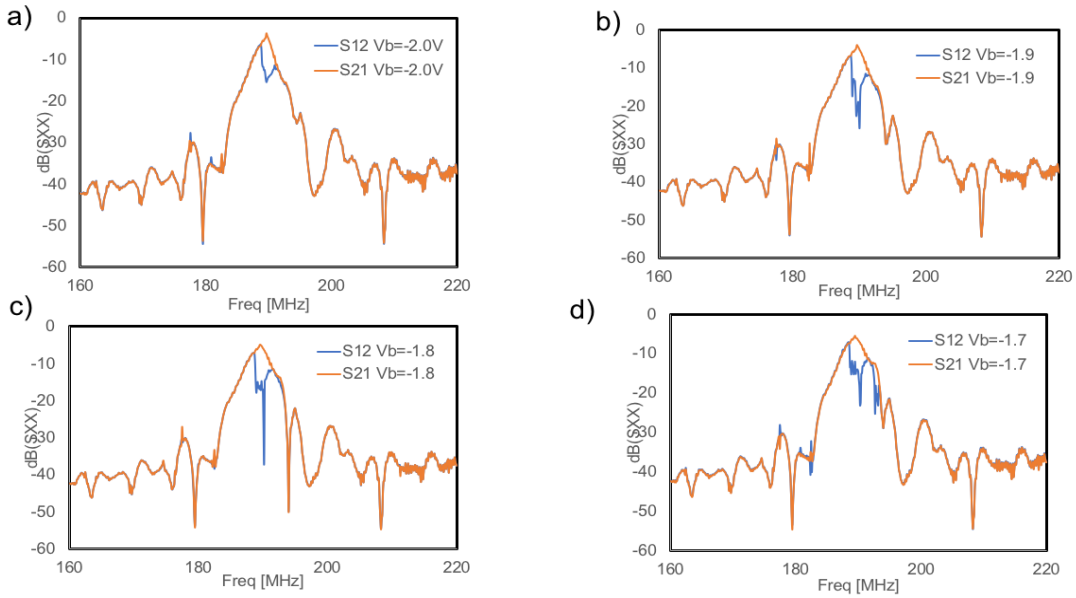

Figure 4.24: a) Forward and reverse S-parameters at varactor bias of -2V. b) Forward and reverse S-parameters at varactor bias of -1.9V. c) Forward and reverse S-parameters at varactor bias of -1.8V. d) Forward and reverse S-parameters at varactor bias of -1.7V. For all measurements $\omega_P = 365MHz$ and pump power is 19 dBm

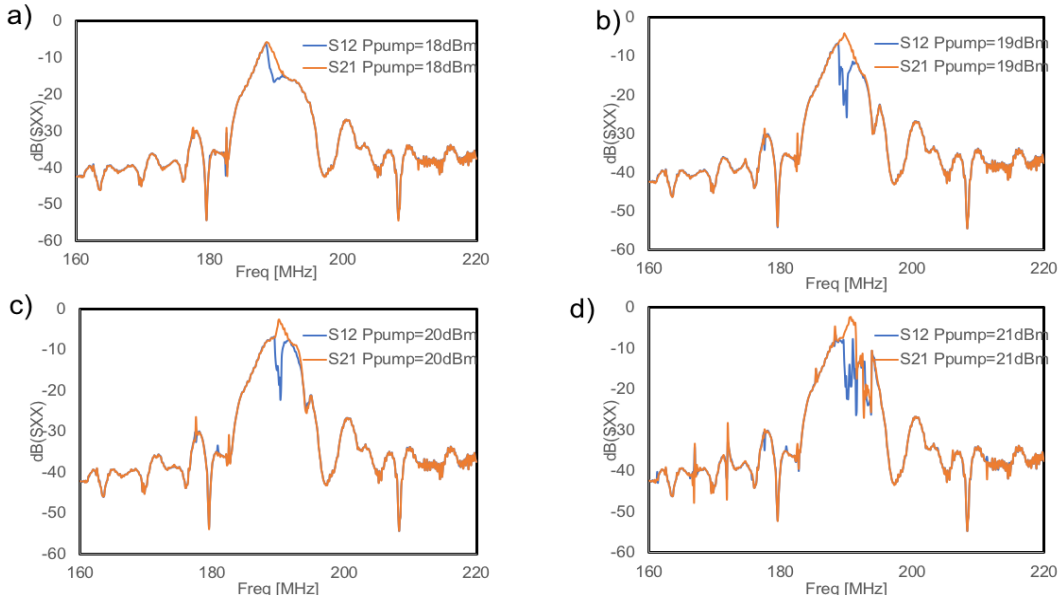

Figure 4.25: a) Forward and reverse S-parameters at a Pump power of 18 dBm. b) Forward and reverse S-parameters at a Pump power of 19 dBm. c) Forward and reverse S-parameters at a Pump power of 20 dBm. d) Forward and reverse S-parameters at a Pump power of 21 dBm. For all measurements $\omega_P = 365MHz$ and varactor biasing of -1.9V.

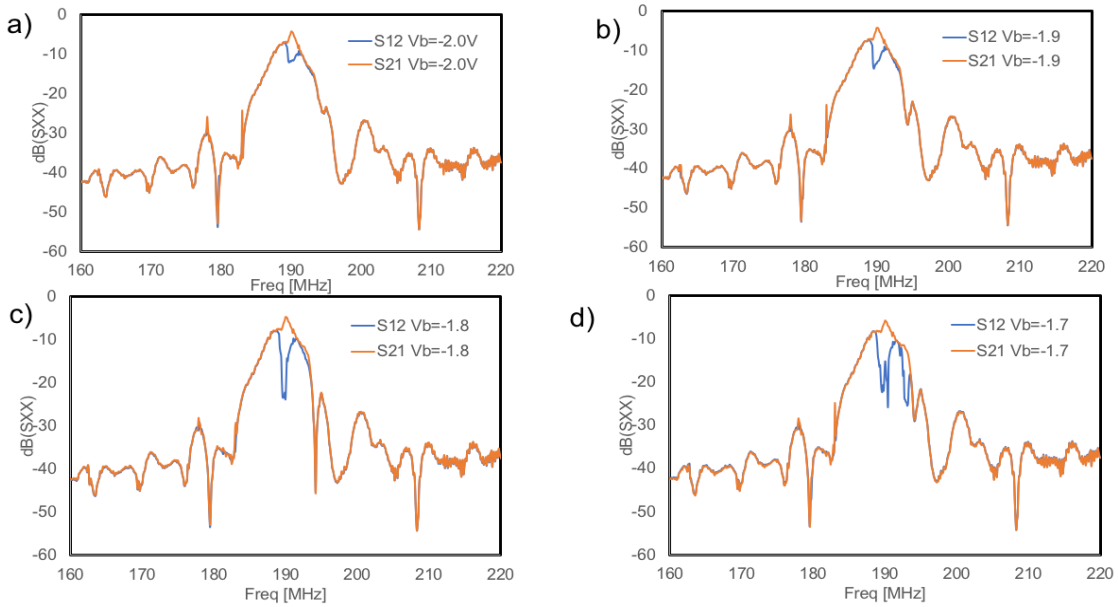

Figure 4.26: a) Forward and reverse S-parameters at varactor bias of -2V. b) Forward and reverse S-parameters at varactor bias of -1.9V. c) Forward and reverse S-parameters at varactor bias of -1.8V. d) Forward and reverse S-parameters at varactor bias of -1.7V. For all measurements $\omega_P = 366MHz$ and pump power is 19 dBm.

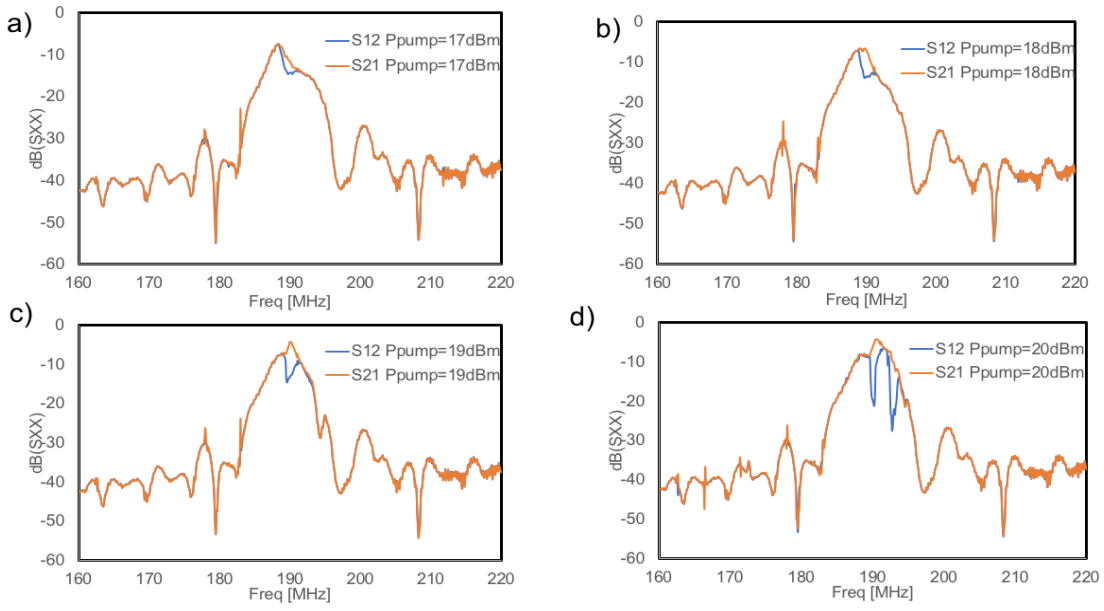

Figure 4.27: a) Forward and reverse S-parameters at a Pump power of 18 dBm. b) Forward and reverse S-parameters at a Pump power of 19dBm. c) Forward and reverse S-parameters at a Pump power of 20dBm. d) Forward and reverse S-parameters at a Pump power of 21 dBm. For all measurements $\omega_P = 366MHz$ and varactor biasing of -1.9V.

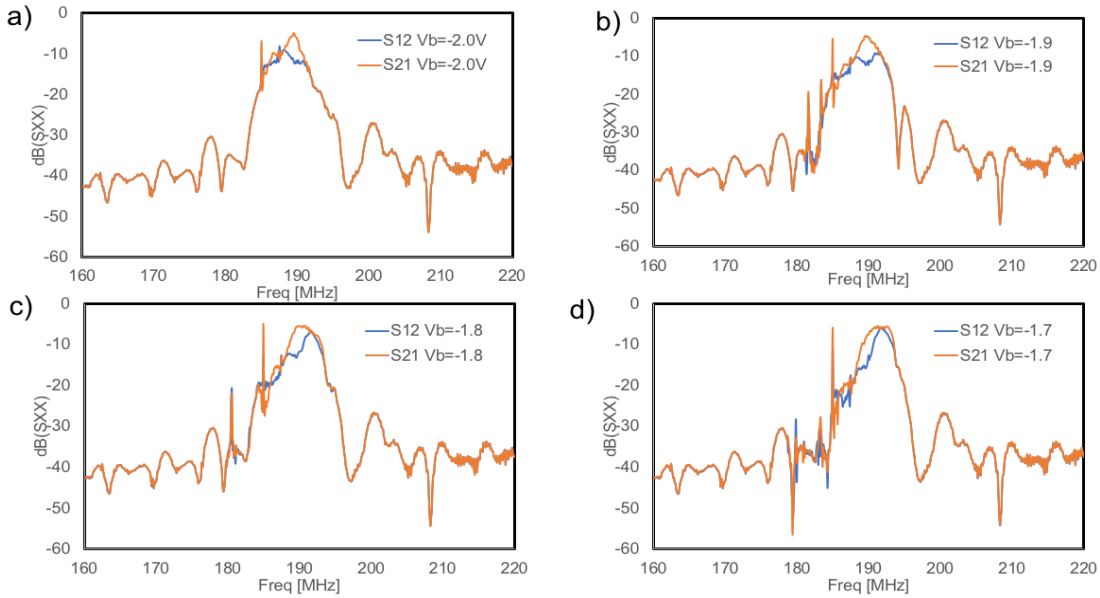

Figure 4.28: a) Forward and reverse S-parameters at varactor bias of -2V. b) Forward and reverse S-parameters at varactor bias of -1.9V. c) Forward and reverse S-parameters at varactor bias of -1.8V. d) Forward and reverse S-parameters at varactor bias of -1.7V. For all measurements $\omega_P = 366MHz$ and pump power is 12 dBm.

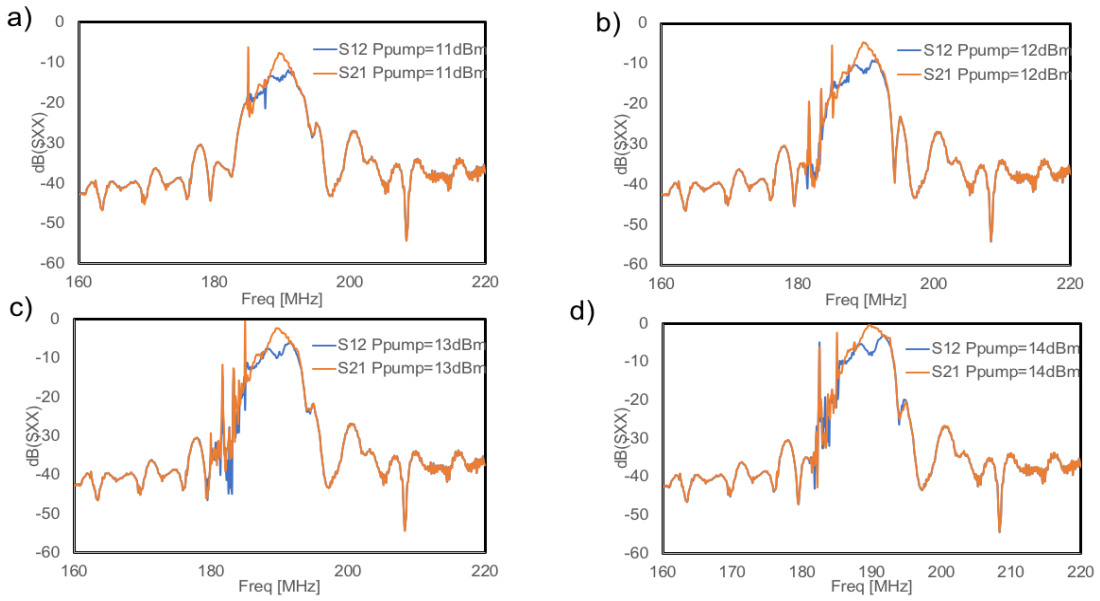

Figure 4.29: a) Forward and reverse S-parameters at a Pump power of 11 dBm. b) Forward and reverse S-parameters at a Pump power of 12 dBm. c) Forward and reverse S-parameters at a Pump power of 13 dBm. d) Forward and reverse S-parameters at a Pump power of 14 dBm. For all measurements $\omega_P = 366MHz$ and varactor biasing of -1.9V.

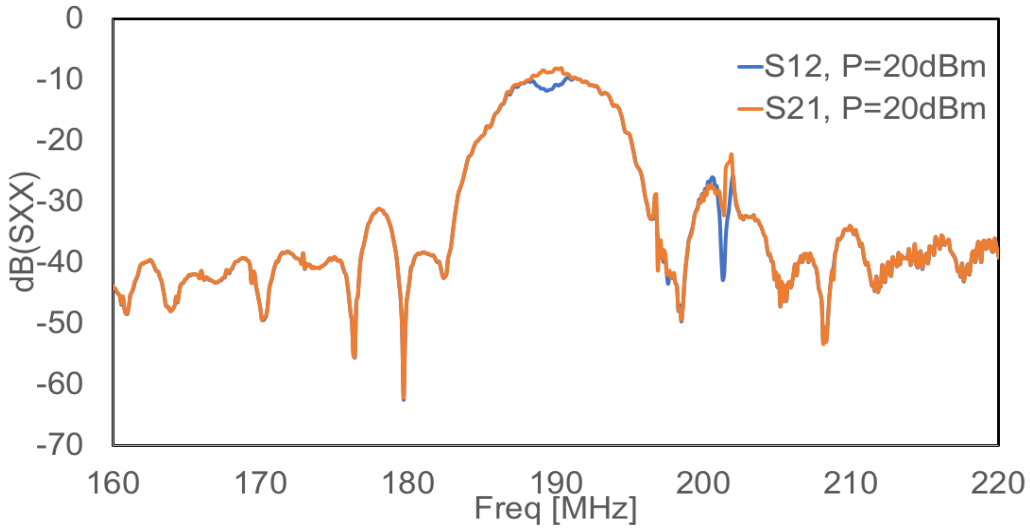

Figure 4.30: Non-degenerate operation where $f_P = 950MHz$ and pump power of 20 dBm. Varactor is biased at -1.6V.

of the filter, the idler will appear at $f_P - f_S$ in the lower side-band. Depending on the applications, only one or both sidebands are considered. If both sidebands are taken into the account, the minimum noise figure can be written as

$$F = 1 + \frac{T}{T_0}(\frac{1}{\gamma Q} + \frac{1}{(\gamma Q)^2}), \tag{4.7}$$

which is very similar to equation 2.48. If only one side-band is considered, the noise figure becomes

$$F = 2\left(1 + \frac{T}{T_0}(\frac{1}{\gamma Q} + \frac{1}{(\gamma Q)^2})\right). \tag{4.8}$$

In the single-sideband case, the minimum noise figure is 3 dB as seen in 4.8. For the purposes of this work, both bands are considered when referring measured noise figure of the parametric amplifier.

Figure 4.33 demonstrates the set-up used to measure the noise figure of the device. The CXA is a vector spectrum analyzer capable of measuring noise figure using the Y-factor method. The measurement results are reported in figure 4.34 for several operating conditions. First, the phase-

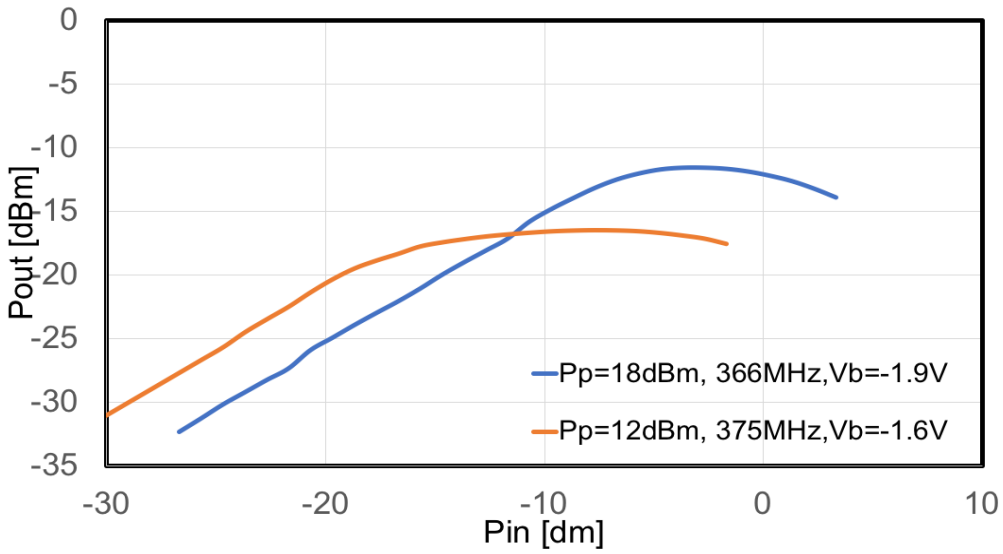

Figure 4.31: AM to AM distortion of degenerate case where $\omega_P = 375MHz$ and P_P=12 dBm (orange) and$\omega_P = 366MHz$ and P_P=18 dBm (blue). Both measurements are made at a signal frequency of 189 MHz

incoherent operating conditions $P_P = 12dBm$ and $f_P = 375MHz$ and $P_P = 17dBm$ and $f_P = 366MHz$ in orange and green have noise figures of 5.6 dB and 16.4 dB at 190 MHz. The large difference in noise figure is a result from the higher quality factor of the operating condition when $f_P = 375MHz$. When the pump is 366 MHz, the idler is not supported by the SAW filter. The low Q termination of the idler causes a degradation in noise figure which is also contributed to by the increase pump power required for operation. Additionally, by inspection of 2.44, when $f_P = 366MHz$, the contribution of the third term is increased since under these conditions $\frac{\omega_S}{\omega_i} > 1$. In contrast, when $f_P = 375MHz$, the pump frequency is approximately twice the center frequency of the filter, thus the idler is fully supported. The required power is decreased; thus, the noise figure is greatly improved.

Similar improvements are made in the non-degenerate case when $f_P = 950MHz$. In this case, the idler frequency will reside around 790MHz and is supported by the pump match network. Since, $\frac{\omega_S}{\omega_i} << 1$, the third term which represents noise current contribution from the idler, is further minimized, resulting in a noise figure of 10dB at 190MHz. This result generates more interest in the non-degenerate operation of the amplifier as a viable high-performance mode of operation.

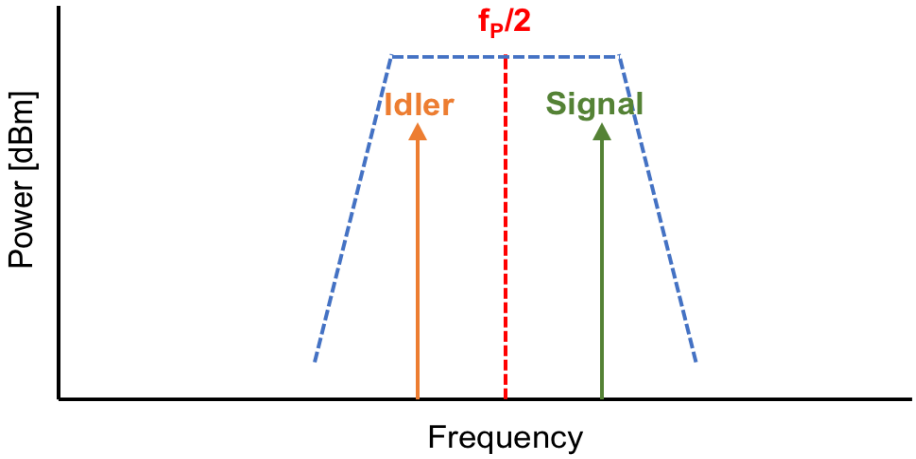

Figure 4.32: Illustration of signal and idler frequencies in band-limited parametric amplifier.

Up to now, the noise figure measurements discussed have been all been of phase-incoherent operation or non-degenerate. The phase-coherent case where $\omega_P = 2\omega_S$ is a special case in which both the signal and idler frequency inhabit the same frequency. In this instance,2.44 is not applicable since this is a single frequency device. In the ideal case, a phase-coherent degenerate amplifier has a noise figure of -3dB, however, this is not obtainable in practice with the use of a separate pump signal as is done here. Thus, most of the noise contributions will arrive from the pump circuit. Utilizing the same measurement set-up for previous noise measurements, the noise figure of the phase-coherent case was performed by recording the noise figure at signal frequencies where $f_S = \frac{f_P}{2}$. This was repeated for pump conditions of 372 MHz to 388 MHz in steps of 2 MHz. The measurement shows an improvement in noise figure down to 4.1 dB at 190 MHz and as low as 3.8dB. The phase incoherent noise at pump frequency 375 MHz converges with the phase-coherent case at 188 MHz near the $\frac{f_P}{2}$ point, thus verifying this method of measuring phase-coherent noise figure. A phase-coherent noise of 4.1 dB signifies there is plenty of room for improvement in optimizing the pump circuit for noise figure.

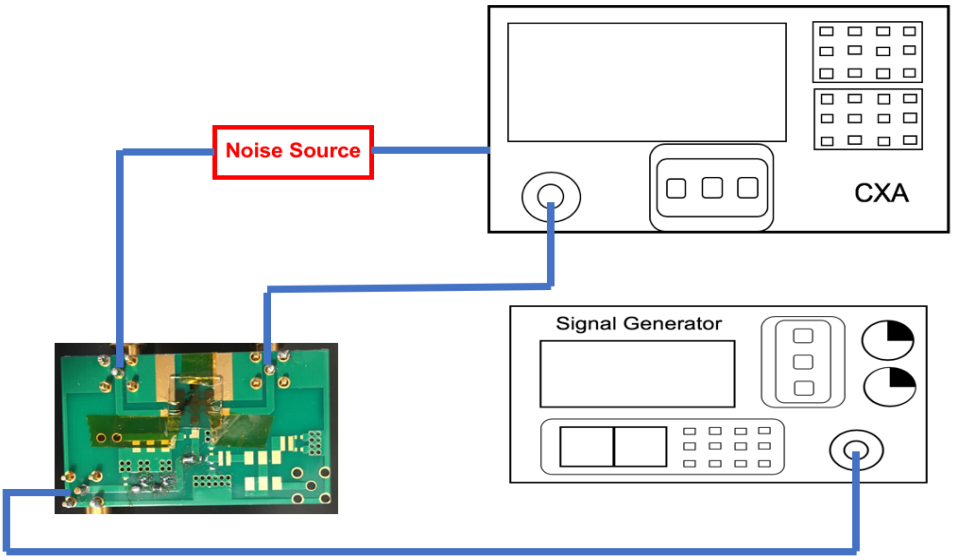

Figure 4.33: Measurement set-up for noise figure measurements. The CXA model N9000A is a vector spectrum analyzer capable of noise figure measurements using the Y-factor method.

4.4 Stability and Design Considerations

Degenerate and non-degenerate parametric amplifiers operate under strong non-linear interactions that result in a large negative resistance. If the effective negative resistance exceeds the intrinsic losses in the circuit, the system will become unstable and oscillate. The structure investigated in this work will be even more sensitive to this instability due to the SAW device behaves as a resonant cavity. This is evident in figure 4.22 where an incoming signal at the output port is transmitted to the center transducer and reflected with gain back to the output port according to the directionality of the transducer. It is again reflected back to the center UIDT where the process will repeat causing an oscillation. Figure 4.35 illustrates the typical network used for stability analysis of a device. Generally, a system is stable if the source and load reflection coefficients Γ_{in} and Γ_{out} abide by

$$\Gamma_{in} = S_{11} + \frac{S_{12}S_{21}\Gamma_L}{1 - S_{22}\Gamma_L} < 1 \tag{4.9}$$

and

$$\Gamma_{out} = S_{22} + \frac{S_{12}S_{21}\Gamma_S}{1 - S_{11}\Gamma_S} < 1 \tag{4.10}$$

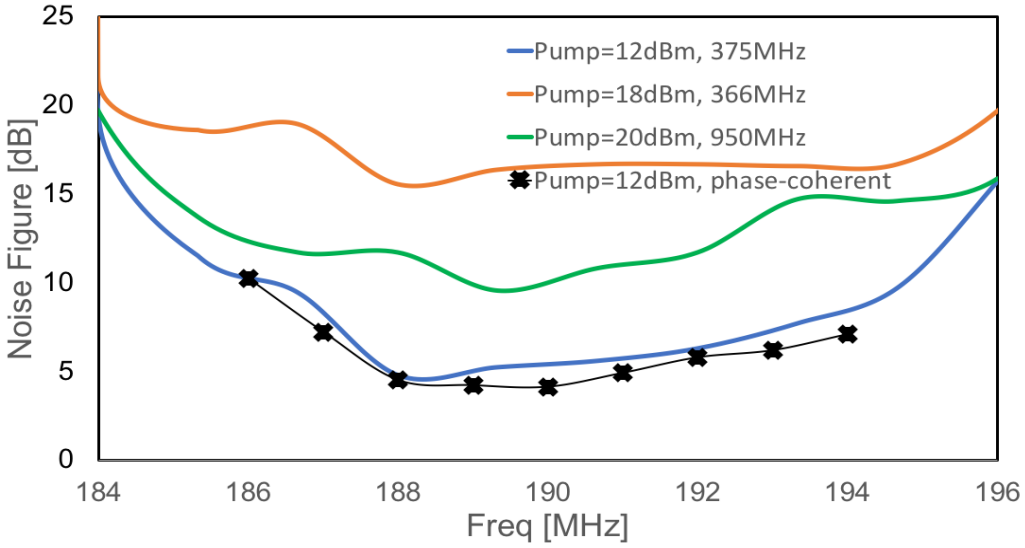

Figure 4.34: Noise figure of non-reciprocal SAW filter under the different operating conditions: phase-coherent condition where $\omega_P = 2\omega_S$ in black, phase-incoherent degenerate cases $P_P = 12dBm$ and $f_P = 375MHz$ in blue and $P_P = 17dBm$ and $f_P = 366MHz$ in orange, and non-degenerate condition $P_P = 20dBm$ and $f_P = 950MHz$ in green.

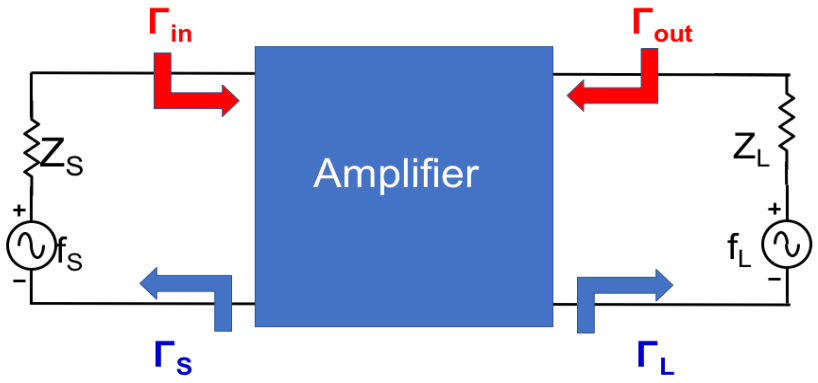

Figure 4.35: Network for stability analysis

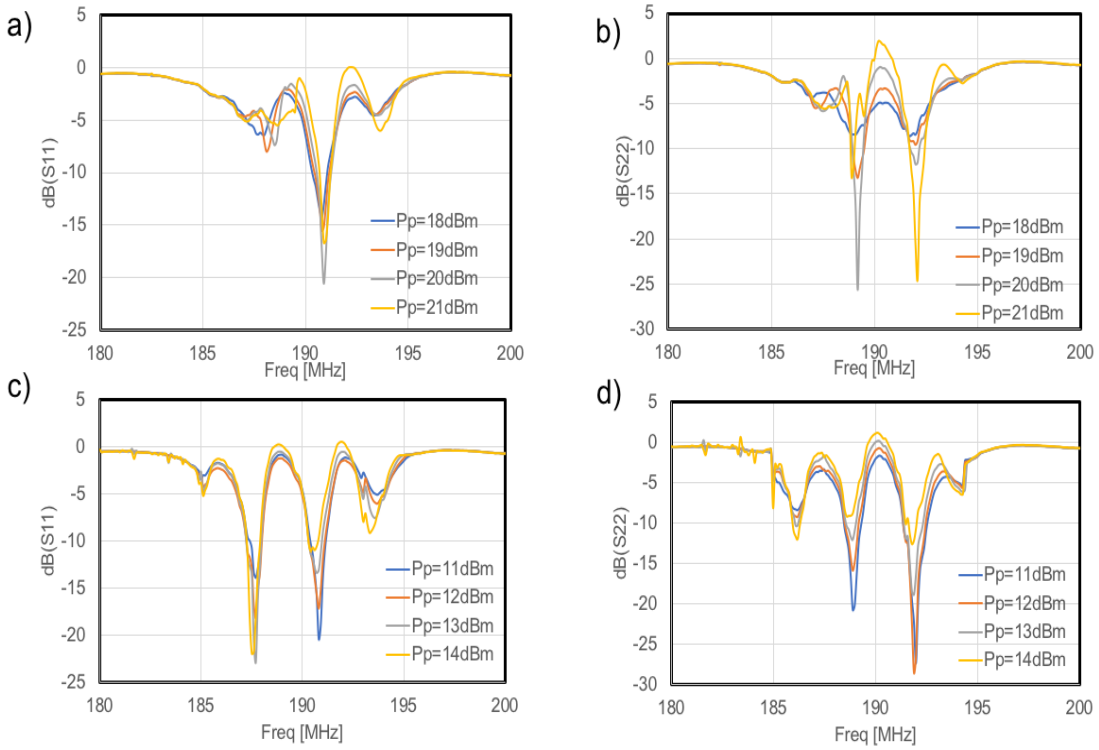

Figure 4.36: a) Input reflection parameter of operating conditions $f_P = 366$ MHz and $V_B = -1.9V$. b) Output reflection parameter of operating conditions $f_P = 366$ MHz and $V_B = -1.9V$. c) Input reflection parameter of operating conditions $f_P = 375$ MHz and $V_B = -2V$. d) Output reflection parameter of operating conditions $f_P = 375$ MHz and $V_B = -2V$

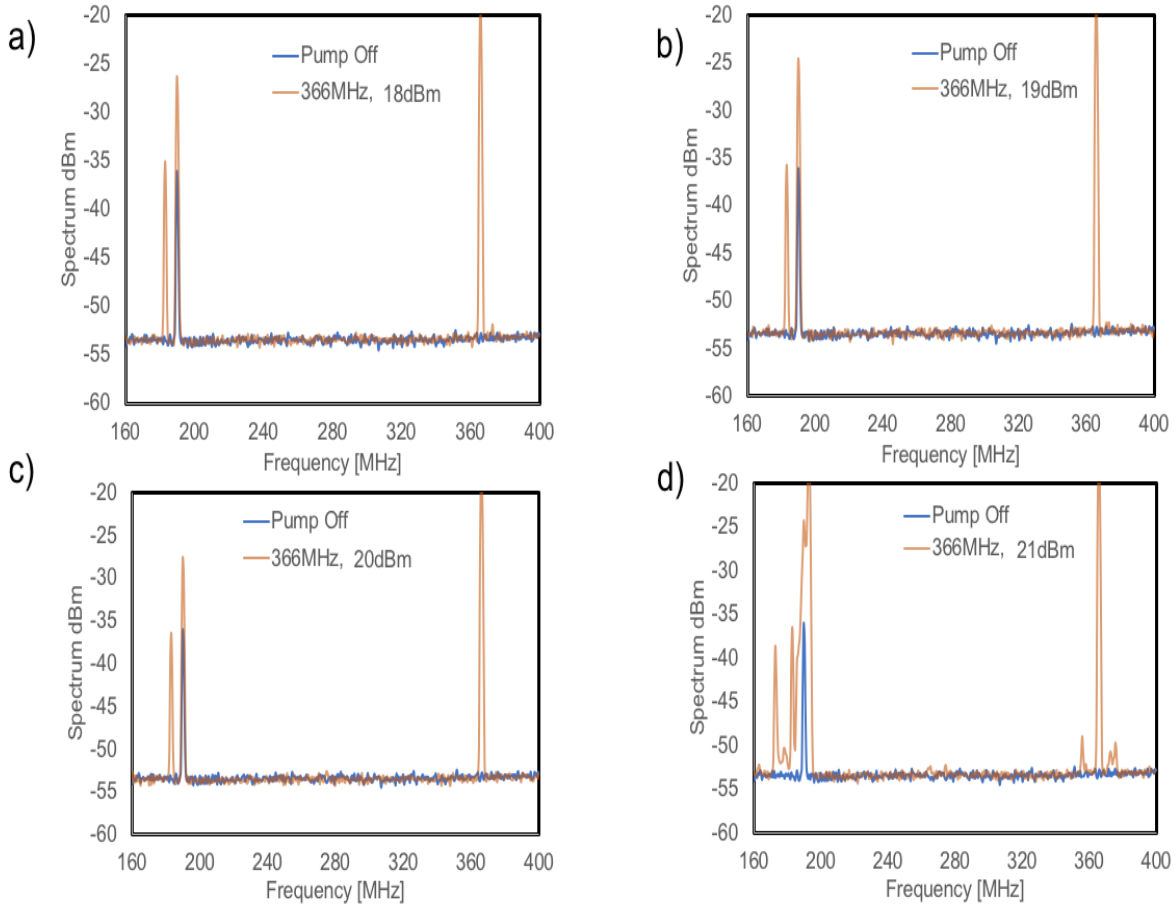

Figure 4.37: a) Output spectrum of operating conditions $f_P = 366$ MHz and $V_B = -1.9V$ at 17 dBm. b) Output spectrum of operating conditions $f_P = 366$ MHz and $V_B = -1.9V$ at 18 dBm. c) Output spectrum of operating conditions $f_P = 366$ MHz and $V_B = -1.9V$ at 19 dBm. d) Output spectrum of operating conditions $f_P = 366$ MHz and $V_B = -1.9V$ at 20 dBm.

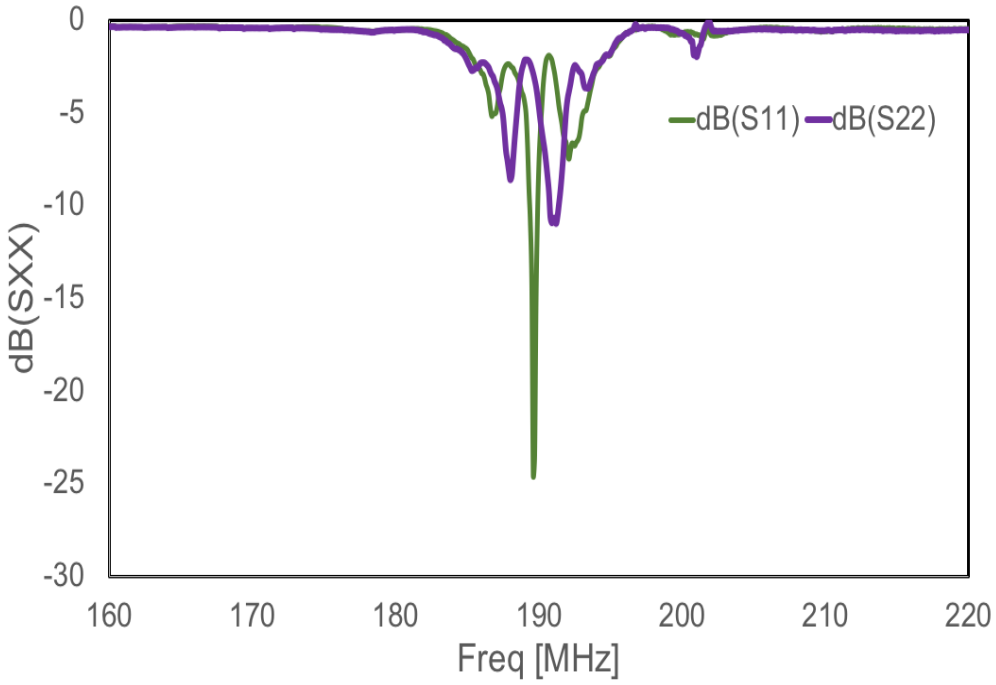

Figure 4.38: a) Input reflection parameter of operating conditions $f_P = 950$ MHz, $P_P = 20dBm$, and $V_B = -1.7V$.

where parameters S_{11}, S_{12}, S_{21}, and S_{22} are the s-parameters of the device and Γ_S and Γ_L are the reflections coefficients of the source and load from the perspective of the device. If the reflection coefficients exceed a value of 1, the signifies that the incoming wave is greater in magnitude than the wave being transmitted at the port which is specifically what is in danger of happening in a resonant cavity.

Given equations 4.9 and 4.10, instability can be detected by inspection of the S-parameters. Figure 4.36 shows the measured S_{11} and S_{22} of the two phase-incoherent operating modes where $f_P = 366MHz$ and $f_P = 375MHz$ at increasing power levels which increases the effected negative resistance. If $dBm(S_{11,22})$ exceeds 0 dBm then $|S_{11,22}| > 1$ thus the device is unstable. For $f_P = 366MHz$, the device becomes unstable at a power level of 21 dBm where both S_{11} and S_{22} exceed 0 dBm. Similarly, the device becomes unstable in the $f_P = 375MHz$ case when the pump power is 13 dBm. In both cases, the output s-parameter S_{22} exceeds 0 dBm by a significant amount. This is due to the directionality of center and output transducers. Since the directivity

of the transducers are opposite, any reflected wave from either transducer will be reflected back by the other if the output transducer is mismatched. This will result in a growing oscillation. The effect can be seen in figure 4.37 a)-d) for a pump frequency of 366 MHz where a 190 MHz signal frequency is presented at the input of the device at -25 dBm. For pump levels of 18 dBm, 19 dBm, and 20 dBm, the device seems stable where only the signal tone, the idler, and the pump tones are visible . However, at 21 dBm, a very large tone appears at 194 MHz indicating an oscillation at that frequency. Other tones appear as well at172 MHz and 187 MHz at lower magnitudes.

The stability of the non-degenerate case is also inspected in 4.38 for $f_P = 950MHz$, $P_P = 20dBm$, and $V_B = -1.6V$. In this case, only one measurement was made due to the equipment not able to source more power at this frequency. The device, however, seems perfectly stable as both S_{11} and S_{22} are well below 0 dBm. This is likely due to the lower negative resistance generated by the pump circuit, but another clear difference from the other operating modes is absence of the idler tone which can be as much of a source of instability as the amplified input signal. This is another potential benefit of a non-degenerate design.

4.4.1 Two-Port Stability Analysis

These results show that precautions must be taken when designing parametric amplifiers to ensure instability, however, parametric amplifiers are a class of circuits where traditional stability analysis is not suffice. As discussed previously, the frequency of oscillation shown in 4.37 d) along with the other tones that appear are unrelated to the signal or pump frequency and their harmonic combinations. Since the oscillation can occur at a frequency that is incommensurate with the pump and signal frequencies, parametric amplifiers are categorized as autonomous circuits. Stability analysis of these type of circuits is difficult and inconclusive due to the existence of multiple solutions [48]. Simulation techniques have been developed for autonomous circuits in [48] based on advanced harmonic balance simulations and analysis. These were specifically adapted for parametric amplifiers in [49]. These techniques, however, are computationally intensive and only focus on the design of the parametric circuit. The structure discussed in this work couples the parametric am-

plifier to a resonant cavity. Therefore, the SAW device plays a very important role in the stability of the overall structure and thus will be the focus of the analysis here.

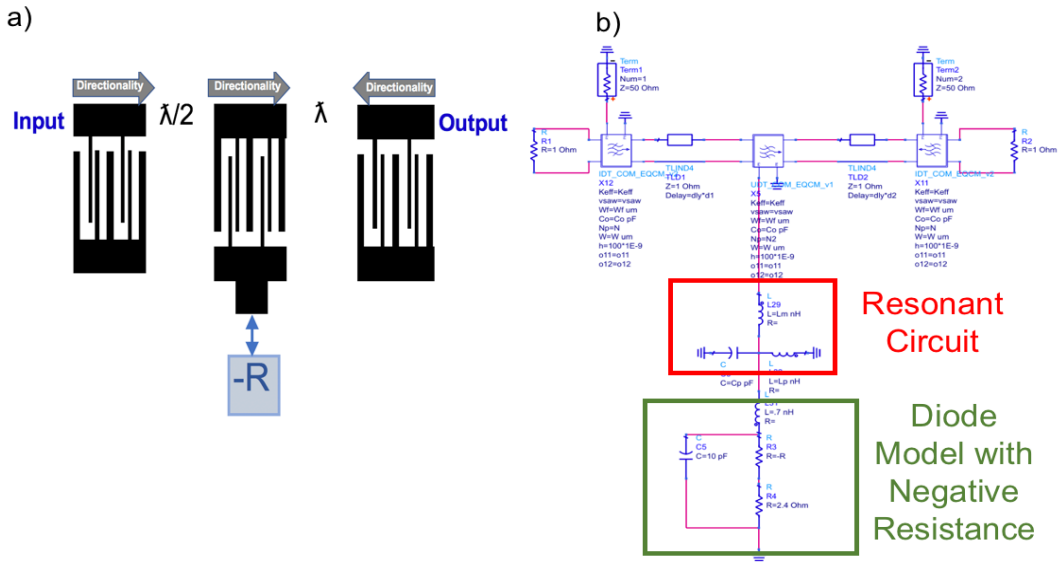

Figure 4.39: a) Linearized version of non-reciprocal SAW filter based on parametric amplification. b) ADS schematic for stability analysis based on small signal modeling. The pump circuit is highlighted in red while the diode model with the negative resistance is highlighted in green.

Traditional stability analysis of an amplifier is based on the inspection of s-parameters to probe under what conditions the input and output impedances have a negative real part. In the fundamental work in [50], Rollett provides a stability factor, k, which is a measure of the stability of the device. The amplifier is said to be stable if $k > 1$ for the frequencies of interest. This analysis however, requires a linearized version of the amplifier. Typically, this is done by extracting a small-signal model of the amplifier or using measured s-parameters of the device. Additionally, the analysis is strictly based on two ports networks.

To begin the analysis, a linearized version of the device is required. Since the SAW device structure is passive, it is inherently linear and stable, however, non-reciprocity occurs due to the non-linear processes of the parametric circuit. Thus, linearization of the circuit does not model the structures actual behavior, but for the purposes of designing the SAW structure, the same approach utilized in [51] is employed here. The parametric circuit can be represented by its resonant circuits and an equivalent circuit model of the diode, where a negative resistance is introduced to simulate

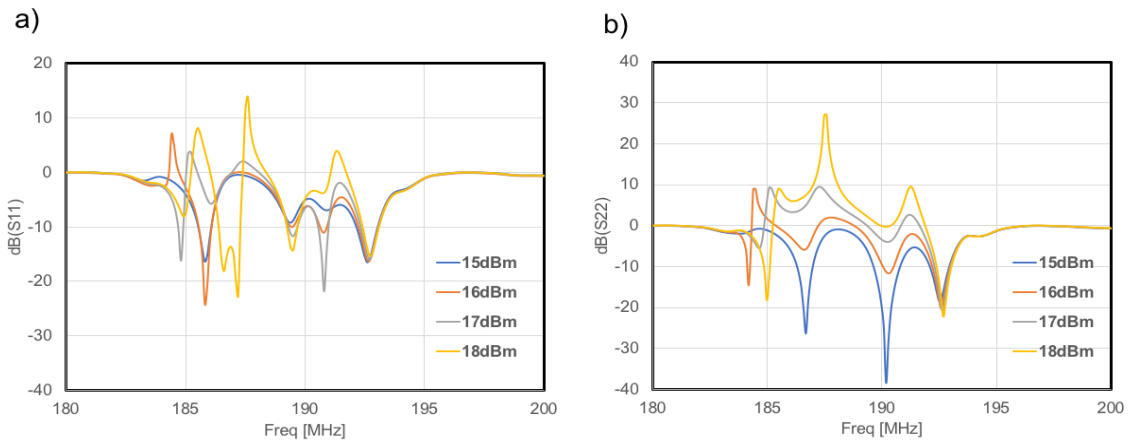

Figure 4.40: a) Input reflection (S11) from ADS simulation of linearized model at different power levels. b) Output reflection (S22) from ADS simulation of linearized model at different power levels.

the gain. Figure 4.39a) demonstrates a diagram of the structure where the center transducer is connected to a negative resistance. This method can then be used to create a small signal simulation to investigate the stability of the network. Figure 4.39a) shows the schematic assembled in ADS highlighting the pump circuit used to resonate the center transducers and the equivalent circuit model of the diode with an added negative resistance, where the negative resistance is given by equation 4.3.

The simulation results of the input and output reflections (S11 and S22) are given in figure 4.40 a) and b) where the transducers have a directionality of 5 dB. The results show a close resemblance to the measurements portrayed in figure 4.36, however, with severe instability. It is quite obvious from the simulations the reflection at port 2 is displaying significant instability reaching values in excess of +20 dB. This is also supported by measurements and is likely due to the directionality of the center and output transducers. To explore this, the simulation was repeated again with a bi-directional output transducer.

Figure 4.41a) and b) demonstrate the simulation results with a bi-directional output transducer. As seen in figure 4.41b), the instability at the output is drastically improved. The input side is

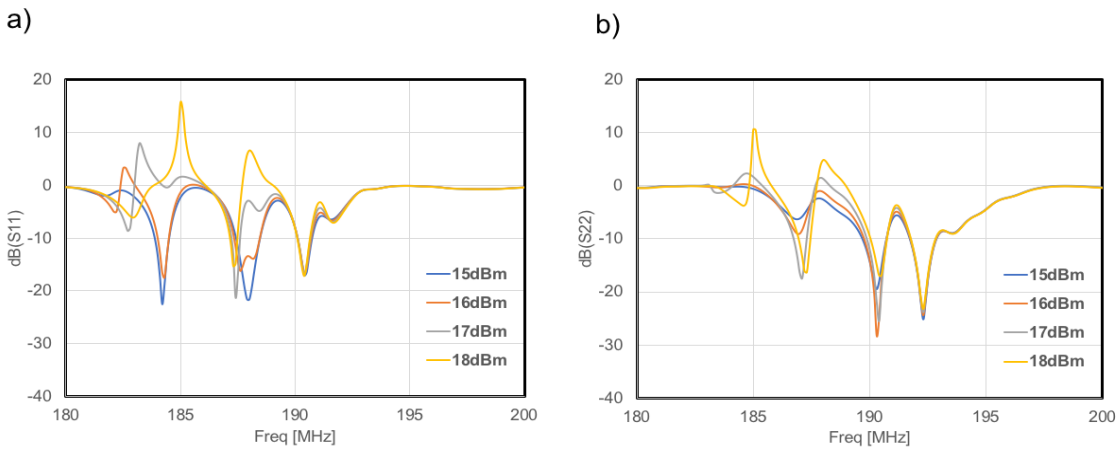

Figure 4.41: a) Input reflection (S11) from ADS simulation of linearized model at different power levels. b) Output reflection (S22) from ADS simulation of linearized model at different power levels. Only input and center transducers are uni-directional.

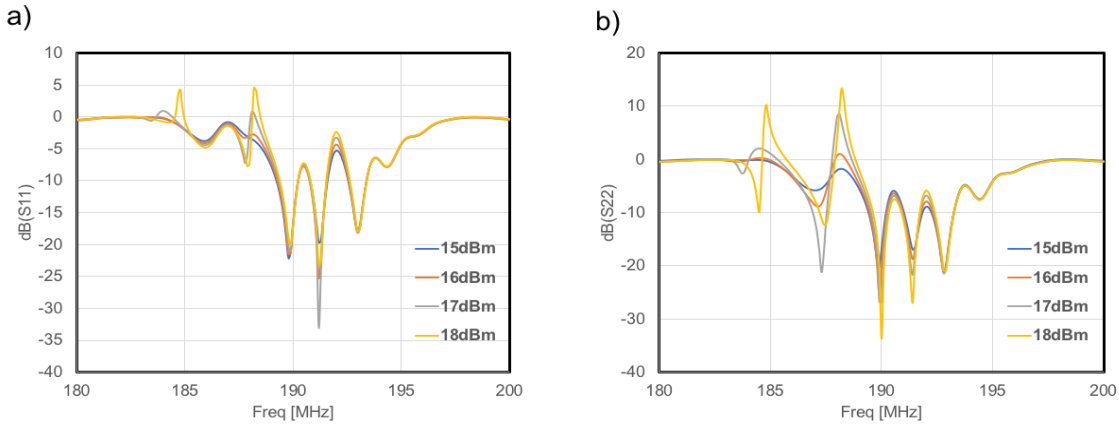

Figure 4.42: a) Input reflection (S11) from ADS simulation of linearized model at different power levels. b) Output reflection (S22) from ADS simulation of linearized model at different power levels. Only center transducer is uni-directional.

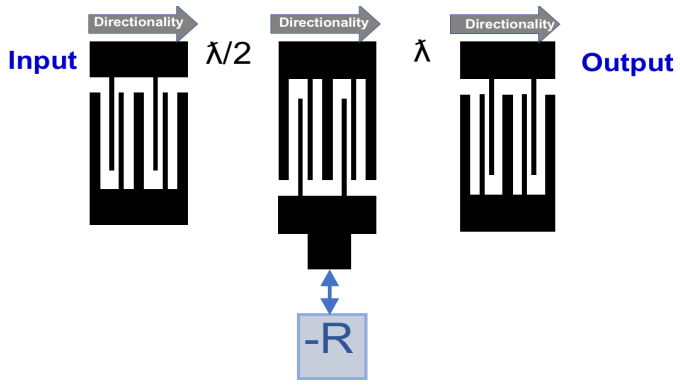

Figure 4.43: Configuration with matching directionality to improve stability.

changed slightly showing little if any improvement, however, this verifies the theory that the combination of uni-directional center and output transducers with opposite directivity, while optimum for insertion loss, is dangerous one for instability. A similar result is observed when both input and output transducers are bi-directional as seen in figure 4.42 a) and b). The input reflection is drastically improved, thus improving overall stability of the circuit.

Another option is to have input and output transducers as uni-directional with matching directivity as seen in figure 4.43. In this configuration, the reflection from the output transducer to the rest of the circuit is minimized. The simulation results are demonstrated in figure 4.44. Compared to the original simulation results in figure 4.40, there is a vast improvement. The drawback of this configuration, as with any configuration other than the original directional transducers with opposite directivity, is the increase in insertion loss and limit the isolation of the device under operation.

Since the insertion loss can somewhat be compensated for, the high isolation is a desired metric that needs to be preserved. Thus, it may be necessary to attempt to stabilize the circuit. Employing traditional amplifier design techniques on the original structure with uni-directional IDTs, the Rollett stability criterion, K, can be used as a metric to gauge the stability of the design. Figure 4.45 shows the stability factor at different power levels for the band edges and center frequency of the bandwidth of interest. Rollett's analysis states that a system is stable if $K > 1$ [50]. As seen in figure 4.45, the K factor becomes lower than 1 at power levels above 15 dBm signifying instability

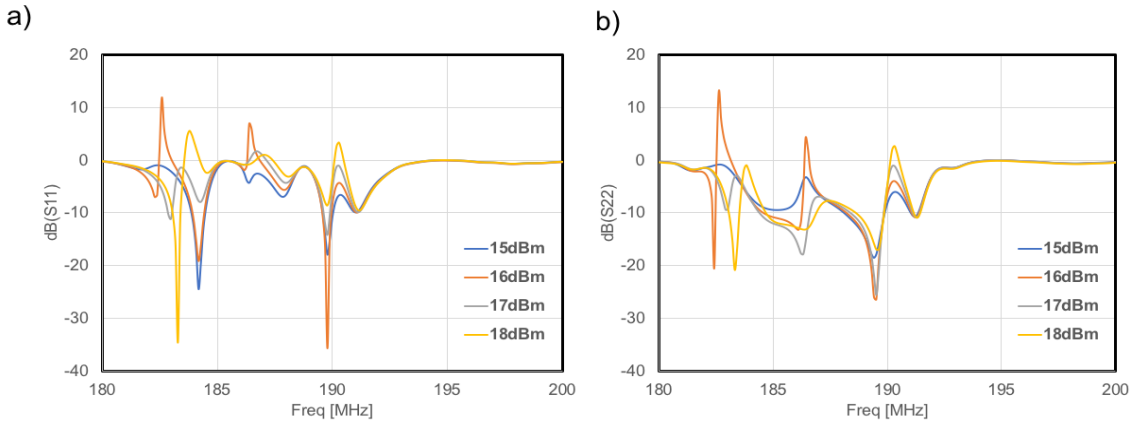

Figure 4.44: a) Input reflection (S11) from ADS simulation of linearized model at different power levels. b) Output reflection (S22) from ADS simulation of linearized model at different power levels. Simulations are based on the configuration in figure 4.43

at those power levels. Since we can assume that we desire to be able to operate the device at these power levels it is necessary to attempt to stabilize the device.

One method of stabilization is to load the input and output with matching networks that stabilize the device. To select impedances that will accomplish this, it is necessary to examine the stability circles of the device on the smith chart. Figure 4.46a)-b) demonstrates the source and load stability circles for the device at the power levels in question for the lower band edge, the center frequency, and the higher band edge. At the frequencies 186 MHz and 190 MHz, the stability conditions are $|S_{11}| > 1$ and $|S_{22}| > 1$ and $K < 1$, thus the area outside the circles are the stable regions. At 194 MHz, the conditions change to $|S_{11}| > 1$ and $|S_{22}| > 1$ and $K < 1$, signifying that the stable region is inside the circle. Ideally, overlapping stability circles are desired, however, in this case, the stability circles require a matching network with large rotations of impedances that is difficult to implement. Thus, it is necessary to modify the circuit to stabilize it.

Stabilizing amplifiers is normally done by introducing loss in feed-back or at the ports. Since any feed-back circuit needs to operate at the bandwidth of interest, it will modify the frequency response of the entire structure. The only choice here is to introduce stabilization networks at the

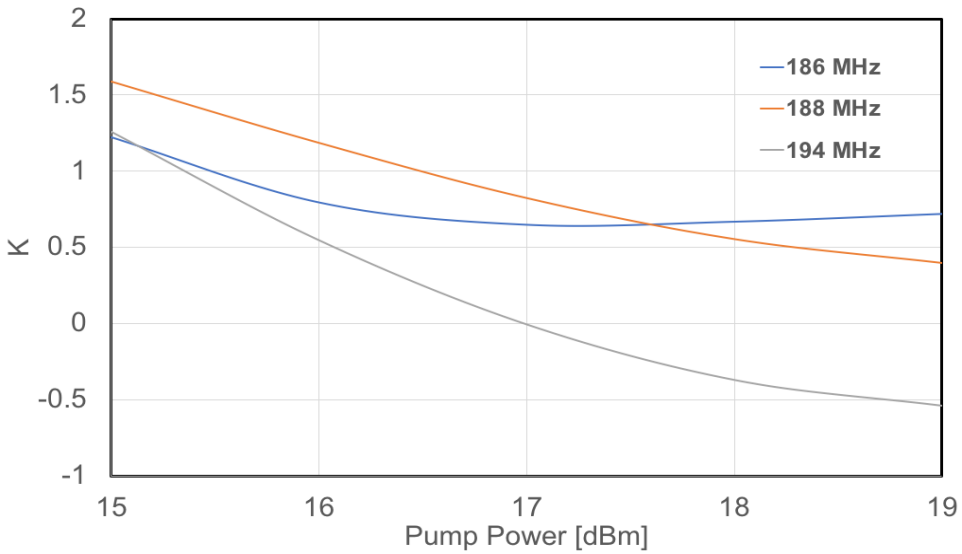

Figure 4.45: Rollett stability factor vs Pump Power.

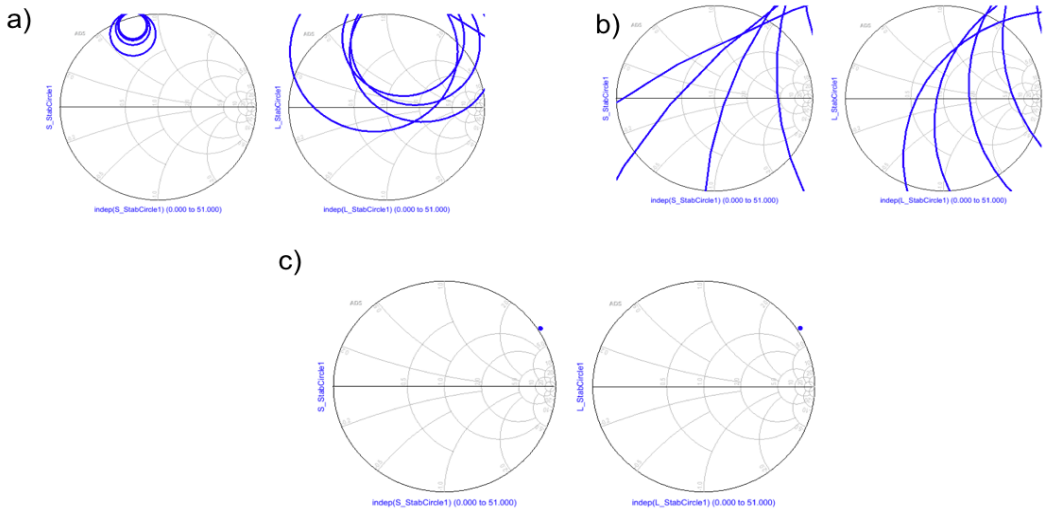

Figure 4.46: a) Source and load stability circles for 186 MHz. b) Source and load stability circles for 190 MHz. c) Source and load stability circles at 184 MHz.

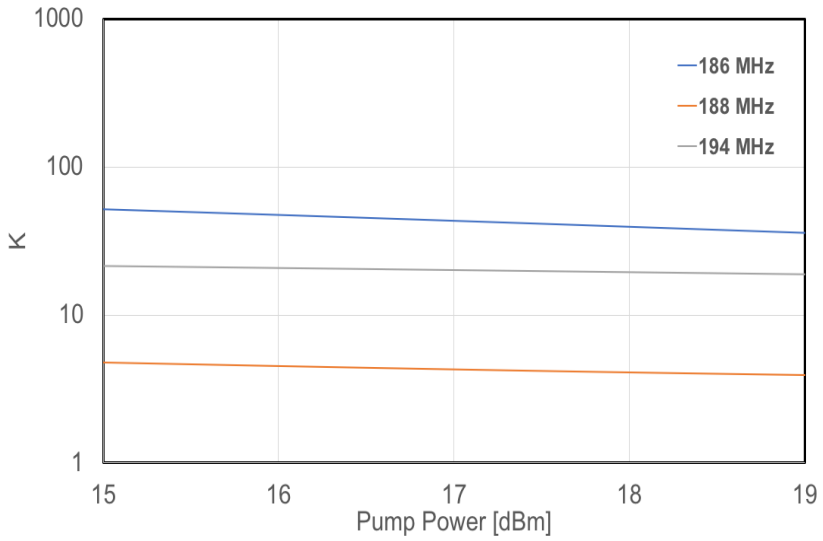

Figure 4.47: Rollett stability factor vs Pump Power with input and output RC stabilization network.

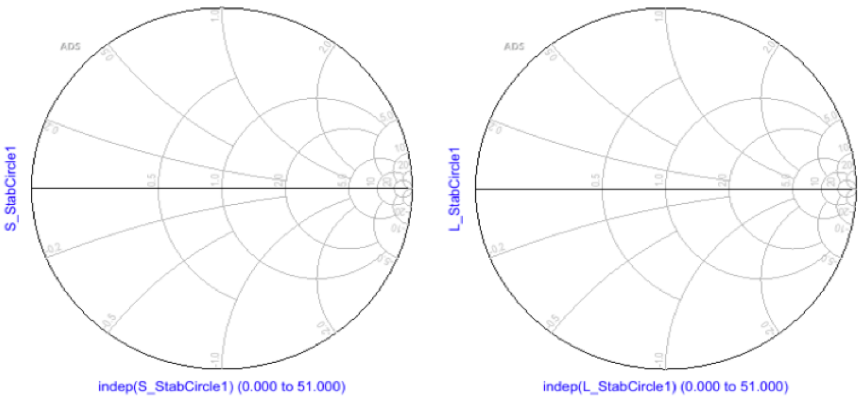

Figure 4.48: Stability circles at all frequencies with RC stabilization network.

input and outputs of the device. In this case, 50pF capacitance and a series resistance of 50Ω were utilized. Figure 4.47 demonstrates Rollett's stability criterion with the stability circuits. As seen here, $K \gg 1$ for all pump power levels signifying the network is stable. The stability circles are then plotted for all frequencies in figure 4.48 to examine any potential instabilities. Since $|S_{11}| > 1$ and $|S_{22}| > 1$ and $K > 1$, the areas inside the stability circles are the unstable regions. As seen here, the circles have been completely shifted outside the smith chart for all frequencies signifying the device is unconditionally stable.

4.4.2 Design Considerations

The previous exercise demonstrates what steps can be taken to examine stability and ensure the SAW structure optimizes the stability of the device. Further investigation into the potential instability of the device requires more advance analysis on the parametric circuit and loading [49]. In this section, the design trade-offs are summarized, focusing on the phase-incoherent non-reciprocal structure. Furthermore, simple relationships are established to obtain first pass designs with first order performance metrics.

Since non-reciprocity is generally desired, the center transducer should be uni-directional. The input and output transducer are acoustically coupled to the center transducer so these play a peripheral role to performance parameters such as gain and noise. Thus, these can be chosen to optimize stability and insertion loss. Therefore, a good point to start is with the center transducer. From

[52], the following simple relations can be defined for SAW transducers at resonance:

$$
\begin{aligned}
G_A &= 8k^2 C_S L f_0 N \\
C_S &= \epsilon N \\
C_T &= C_S L \\
\delta f &= \frac{2f_0}{N} \\
Z_{SAW} &= \frac{1}{G_A + j(\omega f_0 C_T + G_A)} \\
Q_{SAW} &= \frac{f_0}{\delta f}
\end{aligned}
$$

where G_A is the radiation conductance, δ_f is the bandwidth, N is the number of transducer pairs, L is the aperture length of the transducer, and $\epsilon = \epsilon_r \epsilon_e$. Additionally, a behavior model was developed for this work for the directivity of the transducer assuming the electrodes are patterned to maximize directivity. In other words, where the reflection and transduction centers are shifted by $45°$. The directivity in dB can be written as

$$D = 10 \log \frac{N^2}{\mu}. \tag{4.11}$$

where $\mu = \frac{4L}{\lambda}$. The directivity can be used to gauge the amount of minimum isolation when under operation. These equations, along with transducer gain equation 2.39 and single-side band noise figure 4.8 can be used as a means of examining design and performance trade-offs. As an example, figure 4.49 a)-c) demonstrates how the number of transducer pairs impacts important metrics. For the purpose of consistency, the analysis is done for $LiNbO_3$ where $k^2 = .055$, $v_{SAW} = 3780\frac{m}{s}$, and $L = 500\mu m$. The calculations are done at a center frequency of $190MHz$ and a $\frac{\omega_P}{\omega_S}$ ratio is 2, and a varactor Q of 100.

Figure 4.49 a) shows how the fractional bandwidth and SAW quality factor changes. The trade-off here is well known where the quality factor increases and inversely proportional to fractional bandwidth. The directivity of the SAW increases with number of transducers pairs within the

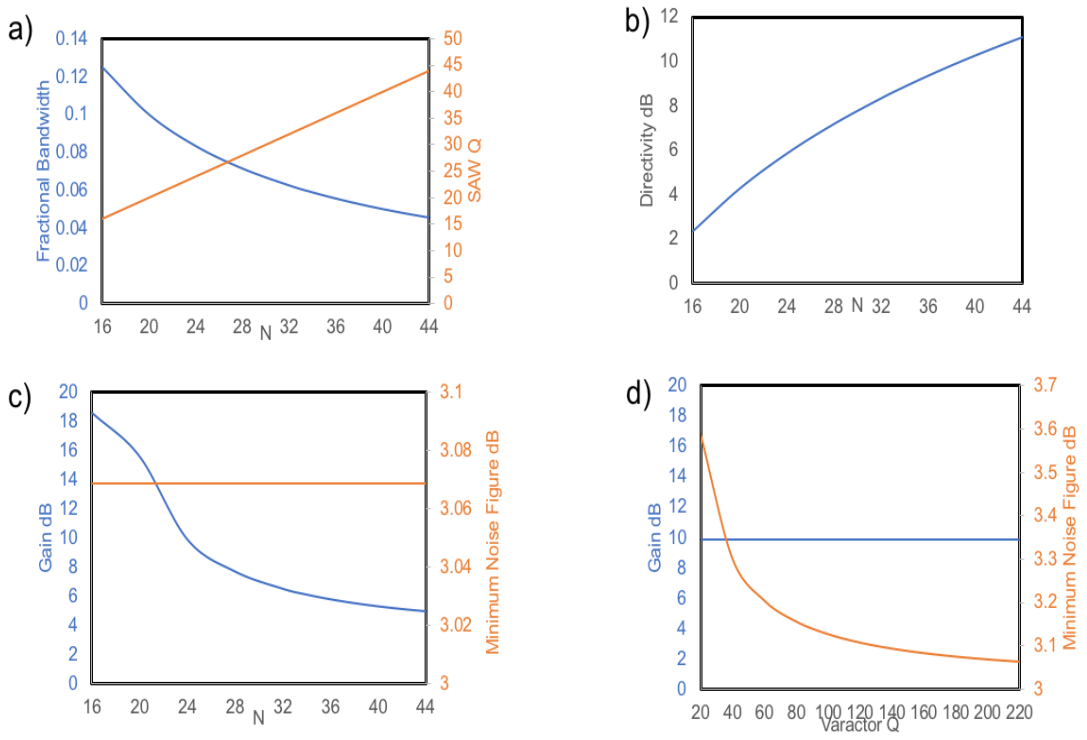

Figure 4.49: Design Tradeoffs. a) Fractional Bandwidth vs. Number of transducer pairs. b) Directivity vs. Number of transducer pairs. c) Gain and Minimum Noise Figure vs. Number of transducer pairs. d) Gain and Minimum Noise Figure vs. varactor quality factor. Number of transducer pairs is 24.

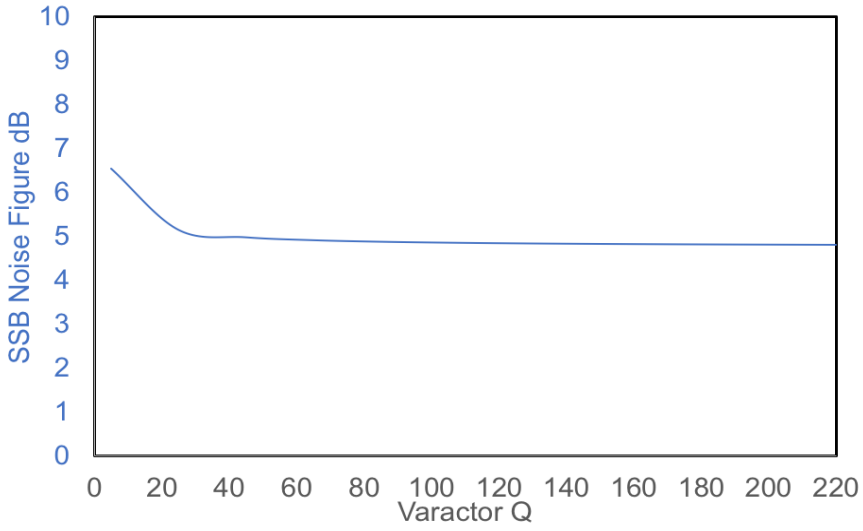

Figure 4.50: SSB noise figure for $N = 24$ vs. varactor Q.

uni-directional transducer as seen in figure 4.49 b). The gain and minimum noise figure are seen in figure 4.49 c). At resonance, the input impedance of the center transducer can be written as $Z_{SAW} = \frac{1}{G_A}$. Thus, the gain decreases with N due to the decreasing load impedance from the perspective of the varactor. The minimum noise figure (F_{MIN}), is impacted very little by the design of the SAW. The noise figure is most impacted by varactor Q. For this reason, F_{MIN} was re-calculated for $N = 24$ where the quality factor of the varactor was changed. The results are displayed in figure 4.49 d). In this case, the gain is not strongly dependent on varactor Q, however, the SSB noise figure is strongly dependent.

From the experimental data, these simple calculations agree reasonably well. For $N = 24$ at $190MHz$, the observed gain is 5-8 dB, while the minimum isolation is 4.8 dB. From 4.49, the predicted gain and isolations are 9 dB and 6 dB respectively. Of the metrics, the minimum noise figure is yet to be verified. However, the unoptimized SSB noise figure can be estimated by equation 2.44. Figure 4.50 shows the re-calculated SSB noise figure. As seen here, a noise figure of 5 dB is observed, which agrees well with 5-6 dB observed in measurement when the pump frequency is $f_P = 375MHz$. An issue arises in the case where $f_P = 366MHz$, where the idler frequency is not fully supported by the SAW filter leading to higher power consumption and

increased noise.

CHAPTER 5
CONCLUSIONS AND FUTURE WORK

This chapter summarizes the work described in this thesis as well as providing a comparison with current state-of-the-art. Possible applications are discussed for both modes of operation. Future work is also discussed to improve device performance to meet the necessary requirements for implementation in systems.

5.1 Summary

The goal of this work has been to introduce, implement, and characterize a novel topology based on surface acoustic waves and parametric amplification capable of non-reciprocal gain of forward waves and attenuation of reverse waves. The architecture can operation under two modes of operation: phase-coherent and phase-incoherent. When operating in the phase-coherent mode, the pump frequency must be maintained $\omega_P = 2\omega_S$ along with the phase relationship between the input and pump signals. The asymmetry designed in the SAW structure causes the reflected-phase shifted current from the parametric circuit to add constructively in the output port and destructively at the input port with the input signal. The device is capable of +10dB of gain and an isolation of up to 20dB. By controlling the phase relationship between pump and input signals, the device can be tuned to operate selectively within the bandwidth of the SAW filter and reverse the gain and isolation relationships.

Figure 5.1 demonstrates a practical implementation of the phase-coherent mode. The input signal can be split, doubled, and amplified to serves as the pump signal. A phase shifter can also be used to tune the non-reciprocity of the device. Other methods would require foreknowledge of the phase of the input signal or more complicated implementations with phase-comparators and phase-locked loops. While there are benefits to this device including high-gain, isolation, and low noise, the requirement of phase-coherence adds a considerable difficulty for deployment in modern

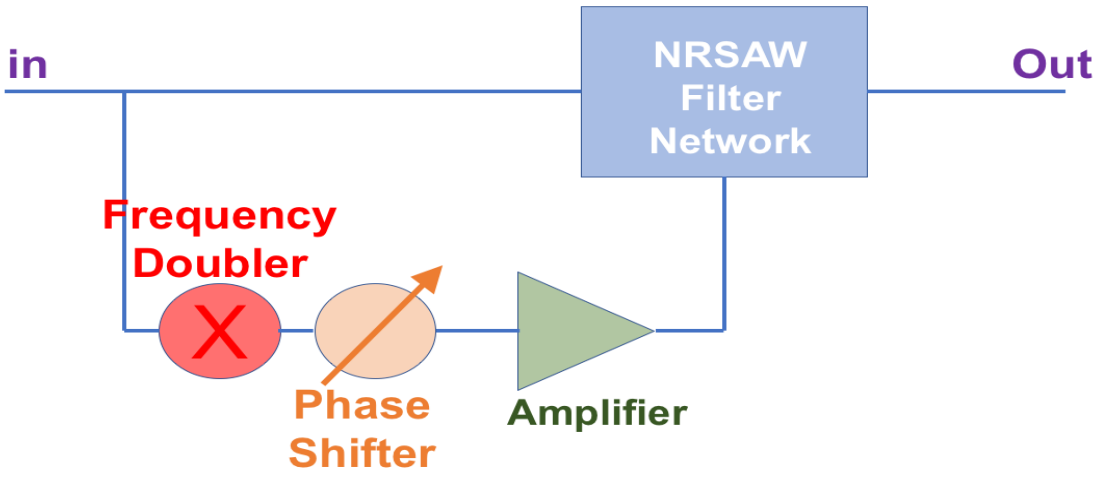

Figure 5.1: Diagram demonstrating implementation of phase-coherent mode.

Table 5.1: Comparison with state-of-the-art work in non-reciprocal acoustic devices. (NR refers to the parameter not reported in the publication).

Works	IL [dB]	Isolation [dB]	f_0 [MHz]	# of LOs	LO freq. [MHz]	NF [dB]
[12] (2019)	-60	16	252	0	-	NR
[9] (2018)	-6.6	25.4	155	4	0.87722	NR
[10] (2018)	-5.6	15	1000	6	10	NR
[11] (2018)	-2.8	12	172	4	47	NR
This work	-5.6	35	189	1	366	16
This work	-3.2	8	189	1	375	5-6

systems. For this reason, the phase-incoherent mode is covered and characterized in more detail.

By introducing a secondary form asymmetry into the SAW structure in the form of a uni-directional center transducer, which couples the parametric circuit with the SAW structure, phase-incoherent non-reciprocity is obtained. The device is capable up to +7dB of internal gain and 30dB of isolation when the pump frequency is 365 MHz at a power of 19dBm. Unfortunately, the noise figure registers at 15-16dB. This is due to the idler frequency not supported by the SAW structure. This also leads to more larger pump power. When the pump frequency is 375MHz, the idler is mostly supported by the SAW filter, thus requiring a lesser power of 12dBm and more gain of up to +10dB. The noise decreases to 5-6dB which agrees well with first order calculations.

A comparison of this to the state-of-the-art, focusing on the phase-incoherent operative mode, is seen in table 5.1. The work in [12] is based on asymmetrical transduced resonators to implement a non-reciprocal filter. While exhibiting a lot of potential, a loss of -60 dB prevents a practical implementation. The works in reported in [9, 10, 11] are topologies based in some form of spatio-temporal-modulation where numerous modulation signals with precise phase relationships are required for operation. This work demonstrates very comparable results with the use of only 1 pump signal. When the pump frequency is 366 MHz, the device outperforms the work in [9] and [10] with better or equal insertion loss (IL) and 10dB or more of isolation. When the pump frequency is 375MHz, the device performance is comparable to that of the work in [11] with a similar insertion loss and isolation. This has the added performance of lower noise figure.

These results demonstrate that this topology possesses significant potential. Additionally, unlike the phase-coherent case, this operative mode does not require foreknowledge of the phase of the incoming signal nor complex phase-synchronization systems. However, both configurations suffer from poor linearity. This metric would need to improve for implementation in practical systems.

5.2 Applications

The applications space for these structures lie mostly in RF and microwave communications. As discussed in chapter 1, filtering is a function that is dominated by acoustic devices. Introducing non-reciprocity of these devices would greatly improve overall performance of the front-end circuits by minimizing losses due to miss-match and providing isolation between signals. This is a promising opportunity for the phase-incoherent mode of operation of the SAW devise proposed in this work. Especially as a way of enhancing the receiver port in full duplex (FD) implementations where the transmitter and receiver share the antenna port via a circulator.

In FD systems, the transmitter and receiver operate over the same bandwidth simultaneously leading to a significant improvement in spectral efficiency and data rates, however, the high-power transmitter signal causes severe self-interference (SI) on the receiver side even with the isolation

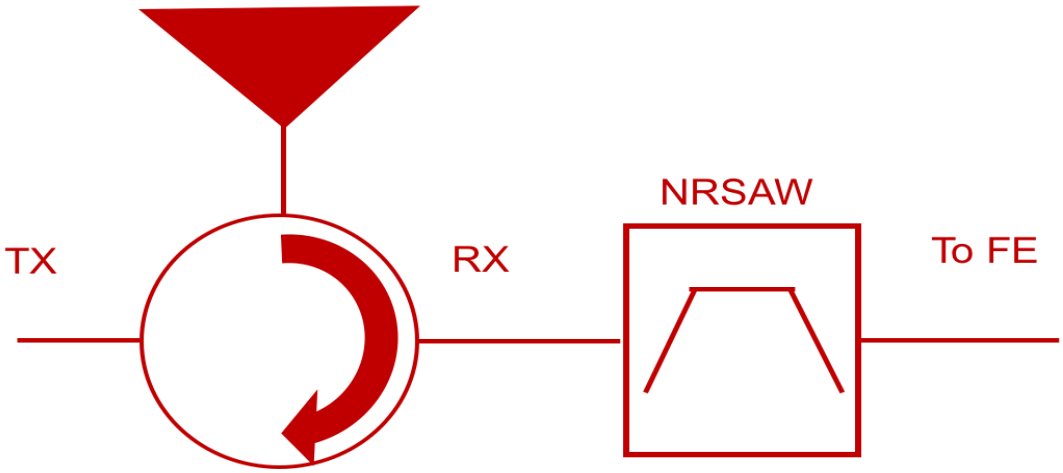

Figure 5.2: Diagram of FD front end with non-reciprocal SAW filter.

provided by a circulator. An FD system with -6dBm of transmit power, 10MHz signal bandwidth and 12 dB of NF budget requires an 86dB of SI suppression to reach the -92 dBM noise floor [53]. With a circulator and analog base-band cancellation, the authors in [53] achieve an SI suppression of 85 dB. If a non-reciprocal filter, as the one demonstrated in this thesis, was introduced on the receiver end with an excess of 20 dB of isolation as illustrated in figure 5.2, it would greatly improve the performance of the system and relax design requirements offering another domain of SI cancellation, however the linearity of the device needs to improve considerably for implementation.

Another system that suffers from the same issues as FD, is magneto-resonance-imaging (MRI) systems. MRI systems operate by placing a patient within an electromagnetic coil and temporarily applying a high magnetic field oscillating at the appropriate resonant frequency. The magnetic field causes the hydrogen atoms in the body to be excited and emit a radio frequency that is then received by the coil and used to create an image. Because of the very strong applied magnetic field and very weak receive signal, this process has to happen in a time-duplex fashion where the equivalent transmit and receive functions are separated in time. This greatly increases the time required to image the patient and is very sensitive to any movement within the cavity. It is clear that an FD implementation would greatly shorten the imaging time and non-reciprocal devices would

aid in the movement issue since this is equivalent to changing impedance. Historically, this has been very difficult to implement due to circulators being based on magnetically-biased materials. However, with advent of magnetic-free circulators, full-duplex MRI (FDMRI) has become possible and has generated interest from the medical community. Recently, the author in [54] demonstrates an analog cancellation method to isolate transmit and receive signals in an MRI system obtaining 100 dB of isolation. Further improvement can be made by introducing non-reciprocal SAW filters. It is especially convenient that MRI operate at RF frequencies in the range of 150 MHz-180 MHz where the performance of SAW devices is unmatched.

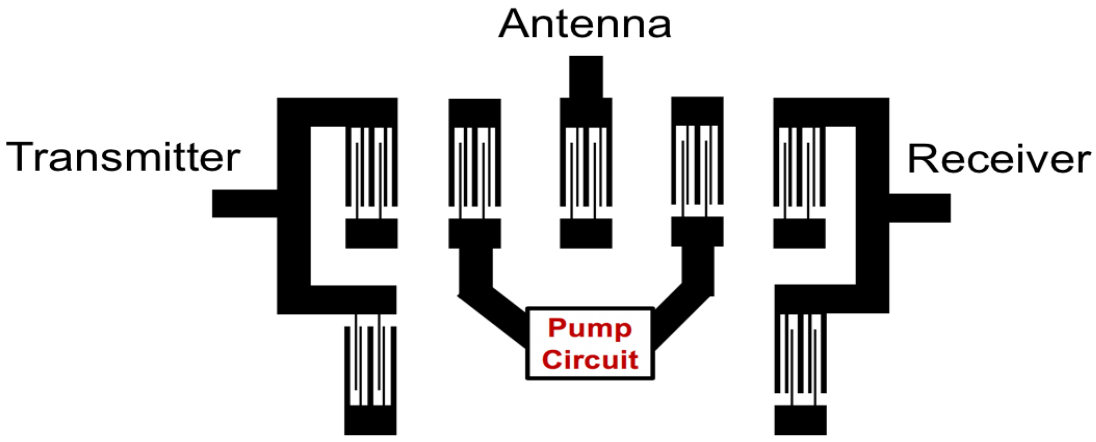

Figure 5.3: Diagram of non-reciprocal SAW used as a circulator.

A very popular application for non-reciprocal devices is that of a circulator. As described in chapter 1, circulators enable FD operation of radio systems greatly impacting the overall performance. A circulator based on the device is illustrated in figure 5.3. The topology consists of two back to back non-reciprocal filters. The directionality goes from left to right from transmitter to receiver with the antenna port in between. The transmitter and receivers are both power split and couple to secondary transducers where the polarity of the transducer is switched from the perspective of the transmitter. This creates the isolation between the transmitter and receiver. Figure 5.4 demonstrates ADS simulation results of the structure. A limiting factor of the device presented in

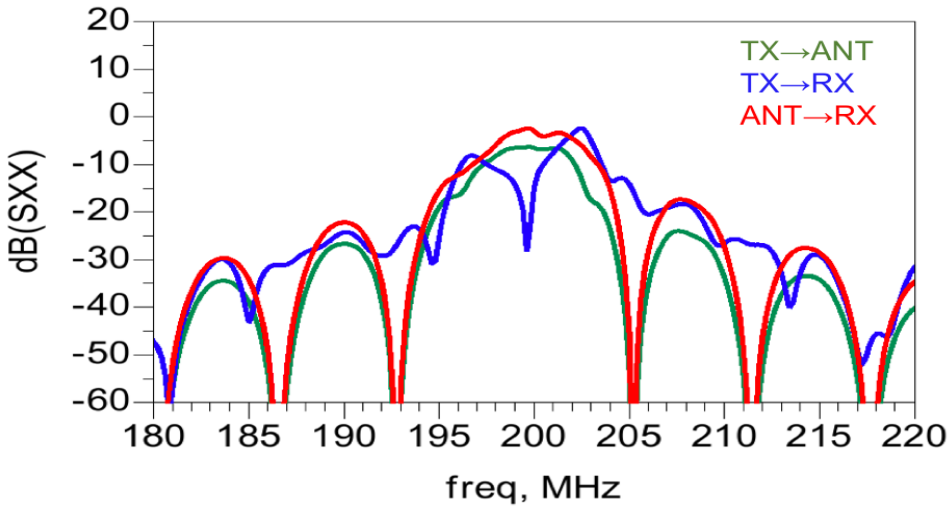

Figure 5.4: Simulation of circulator based on non-reciprocal SAW structure.

this work is the saturated power. The device demonstrates a saturated power of -12 dBm and as seen in equation 4.6, the it is limited by the loading and choice of pump frequency. Due to low antenna impedance, this will be difficult to increase.

5.3 Future Work

5.3.1 Improving Noise Figure

The demonstrated performance of the non-reciprocal filter in this work shows significant promise, however, further work is required to optimize its metrics such as the noise figure. Although the noise is mostly affected by the varactor Q in equations 2.44 and 2.48, the analysis assumes $\omega_P = 2\omega_S$ and consider a poorly supported idler signal which leads to the high noise observed in when $f_P = 366MHz$. More work is required to properly understand the operation of the device under these conditions and how to optimize noise.

Furthermore, a non-degenerate version of the device was briefly investigated, however not designed. A non-degenerate operation offers the ability to completely separate the idler and signal frequencies which is observed to enhance noise figure compared to the degenerate case $f_P =$

$366MHz$ and is theorize to improve stability. The separation of the idler and signal frequencies adds a degree of freedom in design since it allows the pump frequency to be chosen to optimize for gain and noise figure. This, however, requires another resonant circuit to support the idler whose bandwidth is conforms with

$$f_P - f_{SL} = f_{iH}$$
$$f_P - f_{SH} = f_{iL}$$

where f_{SL} is the low end of the signal bandwidth, f_{SH} is the high end of the signal bandwidth, and f_{iL} and f_{iH} are the low end and high end of the bandwidth of the idler. From equation 2.46, this extra degree of freedom allows the designer to choose a pump frequency according to the available varactors to optimize noise figure.

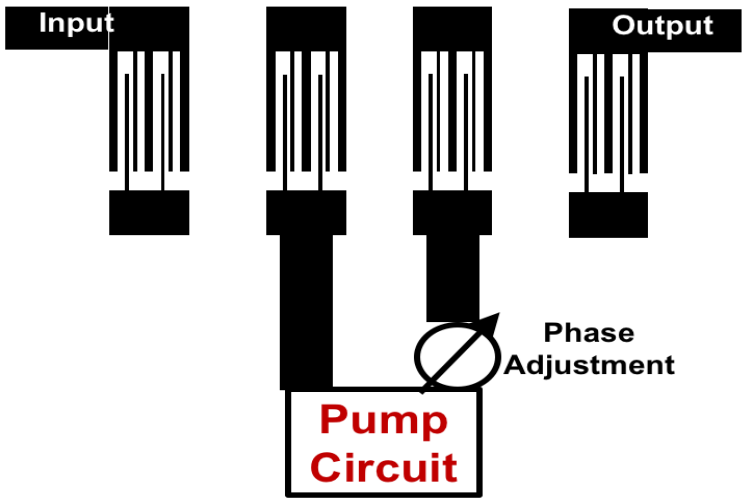

Figure 5.5: Topology to introduce tunability in the phase-incoherent mode of operation.

5.3.2 Improving Linearity

Other than noise, the linearity of the device is another metric requiring further investigation. As seen in figure fig:p1db, the saturated power for degenerate and non-degenerate conditions are $-17.1dBm$ and $-11.6dBm$ respectively. These power levels are very low and within the required the dynamic range for most filter applications, thus these levels need to be increased considerably. Furthermore, the 1-dB compression point for both configurations are $-19dBm$ for the degenerate case and $-7dBm$ for the non-degenerate case. This metric also has to be in improved to levels beyond $0dBm$ to be practical.

As described in the previous chapter, the design utilized in this effort is limited in large signal performance. This is due to the topology used in the pump circuit in which the varactor diode cathode is connected to the pump signal and the anode to the source signal as seen in figure 5.6 a). This simplistic method, while effective, is not ideal for linearity since as the negative resistance amplifies the incoming signal, the voltage drop across the varactor starts to decrease. As this voltage drop decreases, the effective pump signal across the varactor is decreased thereby gradually lowering the negative resistance. This can be remedied by exploring other topologies for the pump circuit. One such topology is a double-balanced mixer topology utilized in [41] as seen in figure 5.6 b). This topology achieves inherent broadband isolation between source and pump signals by thereby enhancing linearity. As reported in [41], the author obtains a saturated power of $-10dBm$ with an improved 1-dB compression point of $-5dBm$ for the degenerate case. Since the non-degenerate case is predicted to be better, this topology is a good start for next design iteration.

5.3.3 Obtaining General Tunability

While tunability is achievable in the phase-coherent mode by controlling the phase relationship between the signal and pump frequencies, the frequency response of the phase-incoherent mode does not demonstrate tunability. While changing the bias of the varactor indeed changes the frequency response, it does not change it in a useful way. To obtain tunability, a secondary transducer can introduce as depicted in figure 5.5. This structure is similar to that of [55, 56, 57] where two

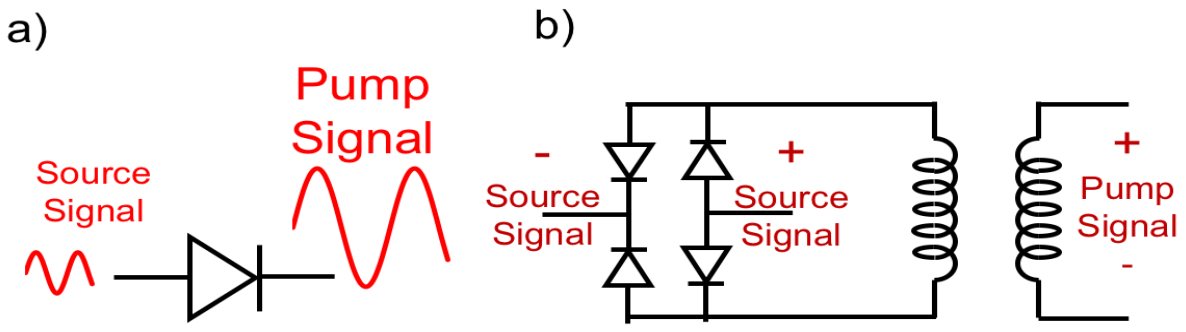

Figure 5.6: a) Single varactor connection used in this design for pump and source signals. b) A double-balance architecture as seen here can be utilized to maximize the voltage swing across varactors thereby enhancing linearity.

varactor diodes are used to create unilateral parametric amplifiers. In this case, the phase relationship between pump signals can be used to tune the frequency response of the device as well. The drawback is the inclusion of another pump signal and more circuitry to implement the phase control.

5.3.4 Low Frequency Pumping

Another path worth inquiry is whether the device can operate at pump frequency below the signal frequency. As suggested by the author in [58], if the varactor is capable of producing odd and even harmonics, it is possible to amplify the signal from a pump signal at a lower frequency. This again requires a secondary pump as shown in figure 5.5. This is of particular interest since decreasing the required pump frequency will decrease the power consumption of the overall system.

5.3.5 Integrated Design in Hetero-junction Platforms

As communications systems become more integrated, it is highly desirable to fabricate and characterize a fully integrated version of the device in a technological platform. One such possibility is

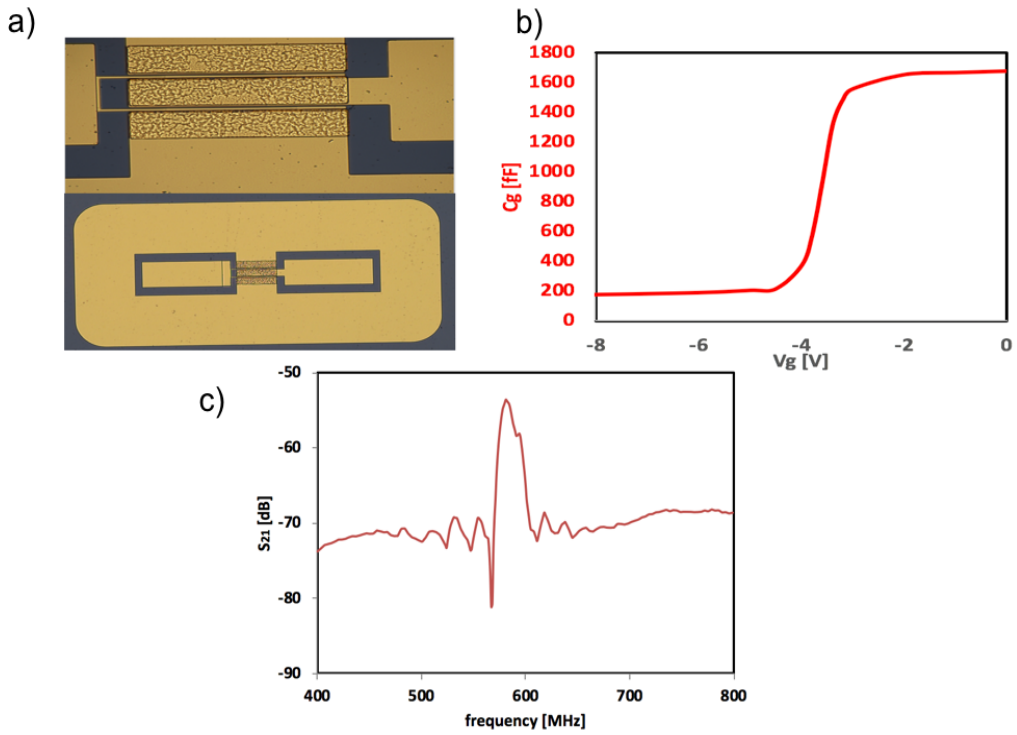

Figure 5.7: a) GaN HEMT with $1\mu m$ gate length with 2 gate fingers and a width of $100\mu m$. b) Total gate capacitance of GaN HEMT. c) Forward transmission S-parameter (S_{21}) of ZnO SAW wave filter on GaN epi .

gallium nitride (GaN). GaN high-electron mobility transistors (HEMT), can function high quality varactors by use of the reverse bias gate capacitance. Figures 5.7 a) and b) demonstrate a GaN HEMT fabricated by the author with a $1\mu m$ gate length as well as the gate capacitance vs. voltage taken at 2GHz. For previous work, the author also developed ZnO delay lines directly deposited on GaN. The forward transmission s-parameter is shown in figure 5.7 c). The insertion loss of the SAW is unfortunately very high, which would limit the performance, however, such a demonstration would valuable.

5.4 Closing Remarks

In this work, the author has demonstrated a novel architecture for reconfigurable and non-reciprocal surface acoustic wave filters. These types of devices have the potential to play a large role in wideband adaptive RF networks for next generation communication systems by reducing the number

of filters required and improving overall performance by providing isolation and improvements in insertion loss. Further work can be focused on improving the noise performance and linearity of both phase-coherent and incoherent modes of operation.

REFERENCES

[1] S. Mahon, "The 5G Effect on RF Filter Technologies," *IEEE Transactions on Semiconductor Manufacturing*, vol. 30, no. 4, pp. 494–499, 2017.

[2] L. Miller, "Carrier Aggregation/ Fundamentals for Dummies," 2016.

[3] Chen-Yu Chi and G. M. Rebiez, "Planar microwave and millimeter-wave lumped elements and coupled-line filters using micro-machining techniques," *IEEE Transactions on Microwave Theory and Techniques*, vol. 43, no. 4, pp. 730–738, 1995.

[4] S. Sun, J. Shi, L. Zhu, S. C. Rustagi, and K. Mouthaan, "Millimeter-wave bandpass filters by standard 0.18-μm cmos technology," *IEEE Electron Device Letters*, vol. 28, no. 3, pp. 220–222, 2007.

[5] C. Hsu, C. Chen, and H. Chuang, "A 60-ghz millimeter-wave bandpass filter using 0.18-μm cmos technology," *IEEE Electron Device Letters*, vol. 29, no. 3, pp. 246–248, 2008.

[6] N. Reiskarimian and H. Krishnaswamy, "Magnetic-free non-reciprocity based on staggered commutation," *Nature Communications*, vol. 7, p. 11 217, 2016.

[7] N. A. Estep, D. L. Sounas, and A. AlÃ, "Magnetless microwave circulators based on spatiotemporally modulated rings of coupled resonators," *IEEE Transactions on Microwave Theory and Techniques*, vol. 64, no. 2, pp. 502–518, 2016.

[8] T. Dinc and H. Krishnaswamy, "A 28ghz magnetic-free non-reciprocal passive cmos circulator based on spatio-temporal conductance modulation," *Digest of Technical Papers - IEEE International Solid-State Circuits Conference*, vol. 60, pp. 294–295, 2017.

[9] R. Lu, T. Manzaneque, Y. Yang, A. Gao, L. Gao, and S. Gong, "A radio frequency non-reciprocal network based on switched low-loss acoustic delay lines," 2018, pp. 1–4.

[10] M. Pirro, C. Cassella, G. Michetti, G. Chen, P. Kulik, Y. Yu, and M. Rinaldi, "Novel topology for a non-reciprocal mems filter," in *2018 IEEE International Ultrasonics Symposium (IUS)*, 2018, pp. 1–3.

[11] J. Bahamonde, I. Kymisis, A. Alu, and H. Krishnaswamy, "1.95-ghz circulator based on a time-modulated electro-acoustic gyrator," in *Proc. IEEE Int. Symp. Antennas and Propagation and USNC-URSI Radio Science Meeting*, 2018.

[12] M. Ghatge, G. Walters, T. Nishida, and R. Tabrizian, "A non-reciprocal filter using asymmetrically transduced micro-acoustic resonators," *IEEE Electron Device Letters*, vol. 40, no. 5, pp. 800–803, 2019.

[13] A. R. Hutson, J. H. McFee, and D. L. White, "Ultrasonic amplification in cds," *Phys. Rev. Lett.*, vol. 7, pp. 237–239, 6 1961.

[14] J. H. Collins, K. M. Lakin, C. F. Quate, and H. J. Shaw, "Amplification of acoustic surface waves with adjacent semiconductor and piezoelectric crystals," *Applied Physics Letters*, vol. 13, no. 9, pp. 314–316, 1968. eprint: https://doi.org/10.1063/1.1652628.

[15] G. S. Kino and T. M. Reeder, "A normal mode theory for the rayleigh wave amplifier," *IEEE Transactions on Electron Devices*, vol. 18, no. 10, pp. 909–920, 1971.

[16] L. A. Coldren and G. S. Kino, "Monolithic acoustic surface-wave amplifier," *Applied Physics Letters*, vol. 18, no. 8, pp. 317–319, 1971. eprint: https://doi.org/10.1063/1.1653677.

[17] K. Yamanouchi and K. Shibayama, "Propagation and amplification of rayleigh waves and piezoelectric leaky surface waves in linbo3," *Journal of Applied Physics*, vol. 43, no. 3, pp. 856–862, 1972.

[18] G. Kino and L. Coldren, "Noise figure calculation for the rayleigh wave amplifier," *Applied Physics Letters*, vol. 22, no. 1, pp. 50–52, 1973. eprint: https://doi.org/10.1063/1.1654471.

[19] G. S. Kino, "Acoustoelectric interactions in acoustic-surface-wave devices," *Proceedings of the IEEE*, vol. 64, no. 5, pp. 724–748, 1976.

[20] J. A. Bahamonde, A. R. Colon, H. Krishnaswamy, and I. Kymissis, "Acoustoelectric amplification of surface acoustic waves on zno deposited on algan/gan epi," in *2017 75th Annual Device Research Conference (DRC)*, 2017, pp. 1–2.

[21] S. Ghosh, M. A. Hollis, and R. J. Molnar, "Acoustoelectric amplification of rayleigh waves in low sheet density algan/gan heterostructures on sapphire," *Applied Physics Letters*, vol. 114, no. 6, p. 063 502, 2019. eprint: https://doi.org/10.1063/1.5080450.

[22] A. Wixforth, J. Scriba, M. Wassermeier, J. P. Kotthaus, G. Weimann, and W. Schlapp, "Surface acoustic waves on gaas/$\mathrm{al_xga1-xas}$ heterostructures," *Phys. Rev. B*, vol. 40, pp. 7874–7887, 11 1989.

[23] J. Pedrós, F. Calle, R. Cuerdo, J. Grajal, and Z. Bougrioua, "Voltage tunable surface acoustic wave phase shifter on algan/gan," *Applied Physics Letters*, vol. 96, no. 12, p. 123 505, 2010. eprint: https://doi.org/10.1063/1.3353971.

[24] R. Li, P. I. Reyes, S. Ragavendiran, H. Shen, and Y. Lu, "Tunable surface acoustic wave device based on acoustoelectric interaction in zno/gan heterostructures," *Applied Physics Letters*, vol. 107, no. 7, p. 073 504, 2015. eprint: https://doi.org/10.1063/1.4928724.

[25] J. A. Bahamonde, A. R. Colon, H. Krishnaswamy, and I. Kymissis, "A tunable surface acoustic wave device on zinc oxide via acoustoelectric interaction with algan/gan 2deg," in *2019 77th Annual Device Research Conference (DRC)*, 2019, pp. 55–57.

[26] K.-y. Hashimoto, *Surface acoustic wave devices in telecommunications. Modelling and simulation*. Jan. 2000, pp. 1–9.

[27] E. Dieulesaint and P. Hartemann, "Acoustic surface wave filters," *Ultrasonics*, vol. 11, no. 1, pp. 24–30, 1973.

[28] M. Lewis, "SAW Filters Employing Interdigitated Interdigital Transducers, IIDT," *1982 Ultrasonics Symposium*, pp. 12–17, 1982.

[29] T. Morita, Y. Watanabe, M. Tanaka, and Y. Nakazawa, "Wideband low loss double mode SAW filters," *IEEE 1992 Ultrasonics Symposium Proceedings*, pp. 95–104, 1992.

[30] K. Yamanouchi and H. Furuyashiki, "New low-loss saw filter using internal floating electrode reflection types of single-phase unidirectional transducer," *Electronics Letters*, vol. 20, no. 24, pp. 989–990, 1984.

[31] ——, "Low-loss saw filter using internal reflection types of single-phase unidirectional transducer," *Electronics Letters*, vol. 20, no. 20, pp. 819–821, 1984.

[32] T. Thorvaldsson, "Analysis of the natural single phase unidirectional saw transducer," in *Proceedings., IEEE Ultrasonics Symposium,*, 1989, 91–96 vol.1.

[33] O. Ikata, T Miyashita, T Matsuda, T. Nishihara, and Y. Satoh, "Development of low-loss band-pass filters using SAW resonators for portable telephones," *IEEE 1992 Ultrasonics Symposium Proceedings*, pp. 111–115, 1992.

[34] R. C. Ruby, P. Bradley, Y. Oshmyansky, A. Chien, and J. D. Larson, "Thin film bulk wave acoustic resonators (fbar) for wireless applications," in *2001 IEEE Ultrasonics Symposium. Proceedings. An International Symposium (Cat. No.01CH37263)*, vol. 1, 2001, 813–821 vol.1.

[35] J. S. Shin, I. Song, C. S. Kim, M. C. Lee, S. U. Son, D. H. Kim, H. S. Park, S. Hwang, and J. S. Rieh, "Balanced RF duplexer with low interference using hybrid BAW resonators for LTE application," *ETRI Journal*, vol. 36, no. 2, pp. 317–320, 2014.

[36] C. L. Hogan, "The ferromagnetic faraday effect at microwave frequencies and its applications: The microwave gyrator," *The Bell System Technical Journal*, vol. 31, no. 1, pp. 1–31, 1952.

[37] S. Tanaka, N. Shimomura, and K. Ohtake, "Active circulators—the realization of circulators using transistors," *Proceedings of the IEEE*, vol. 53, no. 3, pp. 260–267, 1965.

[38] B. Tellegen, "Some general properties of nonlinear elements-part i. general energy relations," *Phillips Research Report*, vol. 3, pp. 366–369, 1949.

[39] J. M. Manley and H. E. Rowe, "Some general properties of nonlinear elements-part i. general energy relations," *Proceedings of the IRE*, vol. 44, no. 7, pp. 904–913, 1956.

[40] L. Blackwell and K. Kotzebue, *Semiconductor-Diode Parametric Amplifiers*. 1961.

[41] G. Blake, "Design of Rf and Microwave Parametric Amplifiers and Power Upconverters," PhD thesis, 2012, p. 104.

[42] W. R. Smith, H. M. Gerard, J. H. Collins, T. M. Reeder, and H. J. Shaw, "Analysis of interdigital surface wave transducers by use of an equivalent circuit model," *IEEE Transactions on Microwave Theory and Techniques*, vol. 17, no. 11, pp. 856–864, 1969.

[43] K. Inagawa and M. Koshiba, "Equivalent networks for saw interdigital transducers," *IEEE Transactions on Ultrasonics, Ferroelectrics, and Frequency Control*, vol. 41, no. 3, pp. 402–411, 1994.

[44] T. Kojima and K. Shibayama, "An analysis of an equivalent circuit model for an interdigital surface-acoustic-wave transducer," *Japanese Journal of Applied Physics*, vol. 27, no. S1, p. 163, 1988.

[45] K. Nakamura, "A simple equivalent circuit for interdigital transducers based on the coupled-mode approach," *IEEE Transactions on Ultrasonics, Ferroelectrics, and Frequency Control*, vol. 40, no. 6, pp. 763–767, 1993.

[46] K. Nakamura and K. Hirota, "Equivalent circuits for unidirectional saw-idts based on the coupling-of-modes theory," *IEEE Transactions on Ultrasonics, Ferroelectrics, and Frequency Control*, vol. 43, no. 3, pp. 467–472, 1996.

[47] K. Kotzebue, "Large-signal characteristics of three-frequency cavity parametric amplifiers," in *1959 IEEE International Solid-State Circuits Conference. Digest of Technical Papers*, vol. II, 1959, pp. 10–11.

[48] A. Suarez, "Analysis and design of autonomous microwave circuits," 2008.

[49] M. Pontón, A. Suárez, B. R. Gray, F. Ramírez, J. S. Kenney, and B. Melville, "In-depth stability analysis of degenerate parametric amplifiers," in *2012 IEEE/MTT-S International Microwave Symposium Digest*, 2012, pp. 1–3.

[50] J. Rollett, "Stability and power-gain invariants of linear twoports," *IRE Transactions on Circuit Theory*, vol. 9, no. 1, pp. 29–32, 1962.

[51] W. J. Getsinger, "Prototypes for Use in Broadbanding Reflection Amplifiers," *IEEE Transactions on Microwave Theory and Techniques*, vol. 11, no. 6, pp. 486–497, 1963.

[52] W. C. Wilson and G. M. Atkinson, "Frequency domain modeling of SAW devices," *2007 NSTI Nanotechnology Conference and Trade Show - NSTI Nanotech 2007, Technical Proceedings*, vol. 3, no. 1, pp. 73–76, 2007.

[53] J. Zhou, N. Reiskarimian, and H. Krishnaswamy, "Receiver with integrated magnetic-free N-path-filter-based non-reciprocal circulator and baseband self-interference cancellation for full-duplex wireless," *Digest of Technical Papers - IEEE International Solid-State Circuits Conference*, vol. 59, pp. 178–180, 2016.

[54] M. Salim, "Full-duplex MRI for zero TE imaging," 2016, p. 54.

[55] J. Hamasaki, "A Theory of a Unilateral Parametric Amplifier Using Two Diodes," *Bell System Technical Journal*, vol. 43, no. 3, pp. 1123–1147, 1964.

[56] W. S. Jones and F. J. Hyde, "Unilateral 2-diode parametric amplifier," *Proceedings of the Institution of Electrical Engineers*, vol. 114, no. 10, pp. 1373–1377, 1967.

[57] H. E. Brenner, "A unilateral Parametric Amplifier," vol. M, no. 5, pp. 790–793, 1974.

[58] S. Bloom and K. K. N. Chang, "Parametric Amplification Using Low-Frequency Pumping," vol. 29, no. 3, p. 594, 1958.

Appendix A: Varactor Diode Principles

As seen in the previous section, the characteristics of the nonlinear capacitor are very important in overall amplifier performance. Up to this point, there has not been any discussion regarding how these are implemented. Due to its manufacturability and high-quality factor, the semiconductor varactor diode is the nonlinear capacitor of choice for many designs [40, 41]. These are normally implemented by using varactor diodes which are based on semiconductor principles. Before beginning in the modeling and design of a parametric amplifiers, it is in order to review of the physics of p-n junctions

A.0.1 P-N Junction Fundamentals

As a consequence of certain quantum-mechanical principles, electrons in crystalline solids can be identified with three types of energy bands: filled, partially filled, and empty. The regions between each band is energetically forbidden for electrons to occupy. The highest occupied band many thusly be filled or partially filled. A partially filled band is also called a conduction band since an applied electric field will cause the electrons to drift and result in electric current. The highest completely filled band is called the valence band. In this case, all states are occupied so the electrons are not free to drift even under an applied electric field. If the highest occupied band is a valence band, the material is either insulating or semiconducting. The difference between the two is the energy required to promote an electron to the conduction band. Insulators require large amounts of energy to accomplish this, on the order of several electron volts. If the gap between the conduction band and valence band is around one electron volt, the material is said to be semiconducting since electrons can make this transition at relatively low energies such as via thermal agitation. An important attribute of semiconductors is that the level of occupancy of the conduction band can be modified by introducing impurities in the crystal. In the case of silicon,

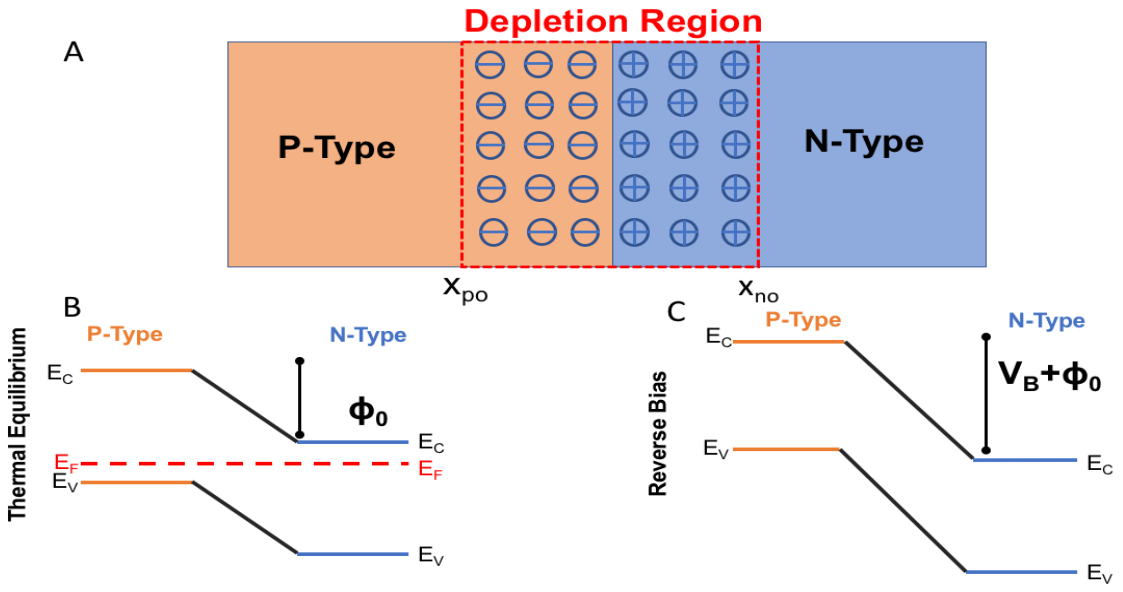

Figure A.1: An Illustration of p-n junction in thermal equilibrium. B Energy band diagram of p-n junction in thermal equilibrium. C Energy band diagram of p-n junction under reverse bias.

dopants can be introduced to replace silicon atoms that either accept electrons or donate electrons. Thus, acceptors decrease the occupancy of electrons, creating holes or absences of electrons in the conduction band while donors increase it by adding free electrons to the conduction band. This results in two different semiconductor types known as p-type where there is an excess of absent electrons and n-type where there is an excess of electrons in the outermost orbitals. Arguably the most fundamental semiconductor device is the interfacing of these two semiconductor types to create a p-n junction as illustrated in figure A.1 A.

When p and n types are combined as in figure A.1 A, the opposition in polarity from the excess electrons on the n-type slide and the large number of holes on the p-type side causes the free electrons on the n-side to be attracted over to the p-side, diffuse into the p-type, combine with the holes and cancel each other out. The holes on the p-side are attracted over to the n-side, diffuse into the n-type, combine with the electrons and cancel each other out. This results in a region at the interface that is depleted of all electrons and holes called the depletion region or space-charge region. Therefore, under no external stimulus, electrons in the n-side cannot drift over to p-side and vice versa. Thus, in thermal equilibrium, the p-n junction behaves as a parallel plate capacitor.

Figure A.1 B illustrates the energy band diagram of the junction in thermal equilibrium. The Fermi level, E_F, represents the type of dopant in the semiconductor. If E_F is closer to the valence band E_V, this signifies that the highest occupancy in the conduction band is very low. In other words, the conduction band E_C is mostly populated by holes. If E_F is closer to the conduction band, the opposite is true. There exists a high population of electrons in the conduction band. To derive this capacitance, we must first derive the physical width of the depletion region. First, we make the approximation that the charge density at either side of the depletion region can be described by

$$\rho_0(x) \approx \begin{cases} -qN_A, & \text{if} - x_{P0} \leq x \geq 0 \\ qN_D, & \text{if} 0 \leq x \geq x_{N0} \end{cases} \tag{A.1}$$

where q is the charge of an electron, N_A and N_D are the acceptor and donor concentrations respectively and x_{P0} and x_{N0} are the depletion widths that extend into the p-side and n-side. Furthermore, because the total charge must cancel out, it must be that

$$x_{P0}N_A = N_D x_{N0}. \tag{A.2}$$

We can now write Poisson's equation in thermal equilibrium as

$$\frac{d^2\Phi}{dx^2} = \frac{\rho}{\epsilon} = \frac{q}{\epsilon} x_{P0}[(p_0 - n_0) + (N_D - N_A)] \tag{A.3}$$

where Φ is the potential across the junction and p_0 and n_0 are the intrinsic carrier concentrations of the semiconductor. Since the depletion region is the area of interest, $p_0 = n_0 = 0$. Performing the integration yields

$$\Delta\Phi = \frac{q}{2\epsilon} \frac{N_A N_D}{N_A + N_D} (x_{P0} + x_{N0})^2. \tag{A.4}$$

Letting $W = x_{P0} + x_{N0}$, the total depletion width can now be written as

$$W = \sqrt{\frac{2\epsilon}{q} \frac{N_A + N_D}{N_A N_D} \Delta\Phi} \tag{A.5}$$

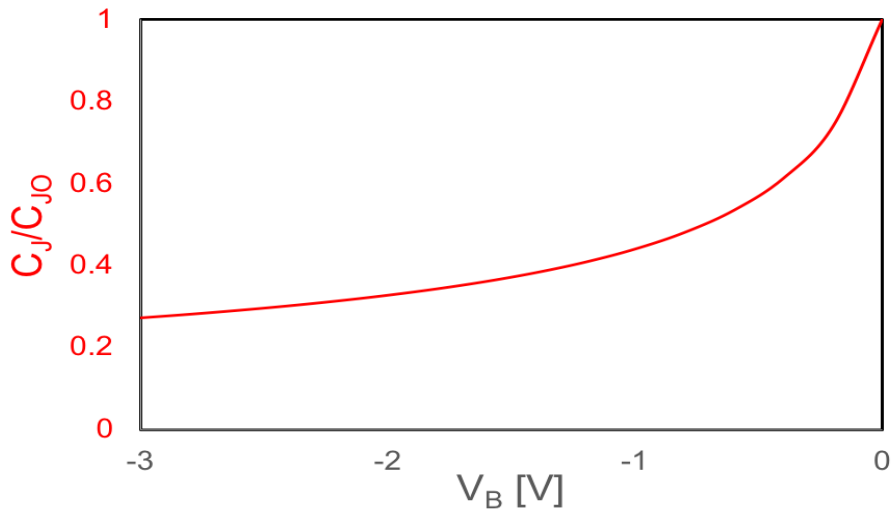

Figure A.2: Example p-n junction capacitance as a function of reverse bias V_B. In this computation $N_A = 10^{15} cm^{-3}$ and $N_D = 10^{10} cm^{-3}$.

where $\Delta\Phi = V_B + \Phi_0$ and Φ_0 is the potential at thermal equilibrium as is equal to $\Phi_0 = \frac{kT}{q} ln(\frac{N_A N_D}{n_0 p_0})$. The constant k is Boltzmann's constant and T is the temperature. V_B is an external bias applied across the junction.

Figure A.1 B depicts the energy band diagram of the p-n junction in thermal equilibrium where $V_B = 0V$. The depletion region is represented by the band bending that occurs in the p and n sides. When an external negative bias is applied, $V_B < 0V$, the depletion region is extended, creating an even larger energy barrier between the p and n regions (A.1C). The depletion width is thereby increased. Thus, the capacitance of the depletion region can be defined as

$$C_J = \frac{\epsilon_S}{W} \tag{A.6}$$

where ϵ_S is the permittivity of the semiconductor material. Figure A.2 demonstrates the junction capacitance C_J normalized to C_{J0} as a function of reverse bias. C_{J0} is the junction capacitance in thermal equilibrium.

We now have a basic understanding of how a variable capacitance is achieved. While many manufacturers provide SPICE models of varactor diodes, it is worth reviewing a basic equivalent

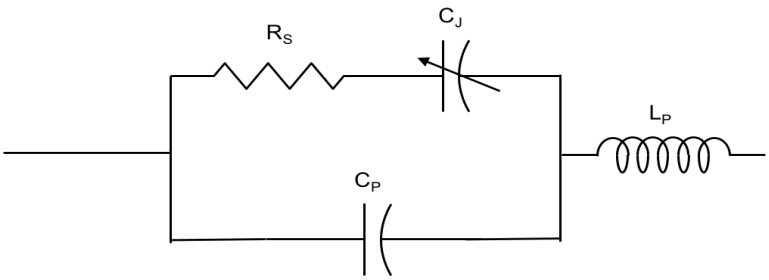

Figure A.3: Equivalent Circuit of varactor based on p-n junction.

circuit to derive the quality factor. An equivalent circuit of the diode used as a varactor is illustrated in A.3. The resistive element R_S is the series resistance resulting from the contacts and metallization of the diode. The capacitance C_P is the parasitic capacitance that arrives from the packaging of the diode. The packaging, geometry, and connections also contribute to an inductance L_P. Using these definitions, the quality factor of the varactor can be written as

$$Q = \frac{1}{2\pi f R_S C(V)} \tag{A.7}$$

where f is the operating frequency. This definition will be useful in later discussions when designing the structure and computing the gain and noise figure of the device.